To the Graduate Council:
I am submitting herewith a thesis written by Shuhua Liang entitled "Numerical Study of the Transition Metal Oxides and the Transport Properties of Iron Pnictides ." I have examined the final paper copy of this thesis for form and content and recommend that it be accepted in partial fulfillment of the requirements for the degree of Doctor of Philosophy, with a major in Physics.

Elbio Dagotto, Major Professor

We have read this thesis
and recommend its acceptance:

Elbio Dagotto

Takeshi Egami

Adriana Moreo

Janice Musfeldt

Accepted for the Council:

Carolyn R. Hodges

Vice Provost and Dean of the Graduate School

To the Graduate Council:
I am submitting herewith a thesis written by Shuhua Liang entitled "Numerical Study of the Transition Metal Oxides and the Transport Properties of Iron Pnictides ." I have examined the final electronic copy of this thesis for form and content and recommend that it be accepted in partial fulfillment of the requirements for the degree of Doctor of Philosophy, with a major in Physics.

Elbio Dagotto, Major Professor

We have read this thesis
and recommend its acceptance:

Elbio Dagotto

Takeshi Egami

Adriana Moreo

Janice Musfeldt

Accepted for the Council:

Carolyn R. Hodges

Vice Provost and Dean of the Graduate School

(Original signatures are on file with official student records.)

Numerical Study of the Transition Metal Oxides and the Transport Properties of Iron Pnictides

A Thesis Presented for

The Doctor of Philosophy

Degree

The University of Tennessee, Knoxville

Shuhua Liang

August 2012

© by Shuhua Liang, 2012
All Rights Reserved.

Acknowledgements

I would like to thank Gonzalo Alvarez, Maria Daghofer, Shuai Dong, Adriana Moreo, Juan Salafranca, Cengiz Sen, Rong Yu and Seiji Yunoki for teaching me so much knowledge about solid state physics. Most importantly, I would like to thank my advisor Dr. Elbio Dagotto for his patience during my PhD study. When I look back, most of his recomendations turn out to be amazingly wise. I also want to use this chance to thank my classmates Qinlong Luo, Andrew Nicholson and Xiaotian Zhang for answering lots of questions for me.

Abstract

Strongly correlated materials such as the manganites and iron pnictides are studied here with several computational techniques. Both types of materials contain transition metals. Thus, our computational models are based on the double exchange mechanism, the super exchange mechanism and the crystal field theory to describe the d electrons. In manganites, we focus on its multiferroic properties induced by the Dzyaloshinskii-Moriya interaction. In the $BiFeO_3$, we use classical Monte Carlo simulations to study the magnetic critical transition transition. In iron pnictides, we study the interplay between the Fermi surface orbital order and the ground state magnetic order.

Contents

List of Tables viii

List of Figures ix

1 Introduction 1

1.1 General Introduction to Multiferroic Manganites 1

1.1.1 Multiferroics 2

1.1.2 Magnetic ferroelectricity in frustrated magnets 4

2 Striped Multiferroic Phases in Narrow Bandwidth Hole-Doped Manganites 9

2.1 Introduction 9

2.2 Model and Methods 11

2.2.1 Model 11

2.2.2 Numerical techniques 13

2.2.3 Generation of ferroelectricity 14

2.3 Results and Discussion 14

2.3.1 $SOS_{1/3}$ and $C_{1/3}E_{2/3}$ at doping $x = 1/3$ 15

2.3.2 Derivative $SOS_{1/3}$ and $C_{1/3}E_{2/3}$ series 19

2.3.3 SOS_x phases at $x = 1/2, 1/5, 1/6, ...$ 25

2.3.4 Macroscopic degeneracy and dimensional reduction 30

2.4 Summary 33

3 Monte Carlo study of a 3D Heisenberg Model to reproduce recent experimental results in $BiFeO_3$ **34**

3.1 Organization . . . 34

3.2 The Heisenberg Model with an isotropic exchange coupling J as a test 35

3.2.1 Comparison with mean-field calculations . . . 35

3.2.2 $T_N(\chi_M)$ from magnetic susceptibility(χ_M) measurements . . . 37

3.3 Heisenberg Model with $J_z = 0$ . . . 38

3.4 3D-Heisenberg Model with anisotropic exchange couplings J: a preliminary test . . . 40

3.5 Addressing the new $BiFeO_3$ experimental results . . . 44

3.6 Differences between the Quasi-2D T-phase and the truly 2D T-phase 49

3.7 Why the 3D T-phase has a lower T_N than the 2D T-phase in a finite lattice . . . 56

3.8 Differences between the Spin Structure Factor and the Staggered Magnetization . . . 56

4 Transport anisotropy of the pnictides studied via Monte Carlo simulations of a Spin-Fermion model **60**

4.1 Introduction. . . . 60

4.2 *Model and Method.* . . . 63

4.3 Results . . . 66

4.4 R vs. T curves. . . . 71

4.5 Conclusions. . . . 75

5 Summary **76**

Bibliography **77**

A Multi d-orbitals for Manganites and Iron pnictides **88**

Vita **91**

List of Tables

2.1 The multiferroelectricity of SOS_x and C_xE_{1-x}. Here only the primary states have been considered. The origins of FE polarization vary with the dopings and spin orders. 31

3.1 Comparison of Néel temperates between our simulations and those of Ref. Yasuda et al. (2005). ($J_x = J_y = 1$) 42

4.1 Δ_{xy} represents the xy orbital on-site energy. This table is reproduced from Table I of Ref. Daghofer et al. (2010b) 64

List of Figures

1.1 The magnetization, resistivity, and magnetoresistance of $La_{0.75}Ca_{0.25}MnO_3$ as a function of temperature at various fields. This figure is reproduced from Ref.[Schiffer et al. (1995)] 2

1.2 The comparison between spatial reversal symmetry and time reversal symmetry shows that ferroelectricity is generated with different symmetry breaking properties as magnetism. 3

1.3 Figure illustrating the Dzyaloshinskii-Moriya interaction $H_{\mathrm{DM}} = \lambda x \times \vec{r}_{12} \cdot [S_1 \times S_2]$ which tends to move the oxygen atoms away from the straight bond Mn-O-Mn defined by r_{12}. The symmetry properties of the DM interaction indicate that only spin configurations with nonzero cross product between nearest-neighbor spins will induce ferroelectricity. In particular, spiral spin configurations will shift every oxygen atom into the same direction, thus inducing a total nonzero polarization. This figure is reproduced from Ref.[Cheong and Mostovoy (2007)]. 5

1.4 Illustration on how a perovskite $RMnO_3$ with spiral magnetic order polarization is rotated by an applied magnetic field. Spiral spins prefer to be perpendicular to strong magnetic fields. Then, if the (a) spiral spins are in the $a-b$ plan, the polarization is along the a axis. But (b) after applying a magnetic filed along the a axis, the spins rotate into the $b-c$ plane which causes the polarization P to rotate 90 degrees. This figure is reproduced from Ref.[Cheong and Mostovoy (2007)]. . . 6

1.5 Phase diagram of $RMnO_3$. Left upper inset shows a schematic view of reciprocal space. The right upper inset shows the wave numbers of the modulated crystallographic structures in a-b plane. The main portion of the figure shows the phase diagram including the A-AFM phase, the spiral-AFM state, and the E-AFM state as the Mn-O-Mn bond angle ϕ varies. This figure is reproduced from Ref[Goto et al. (2004)]. . . . 7

2.1 (Color online) An example of zero-T variational calculation: comparing the energies of several candidate spin orders at doping $x = 1/3$ and $\lambda = 0$ as a function of $J_{\rm AF}$. The dots represent MC results results at $T = 0.002$. S6-a (and S6-b) denote the spiral phase which's period is 6.Dong et al. (2008b) The energies of S6-a and S6-b are calculated in an infinite and $L = 6$ lattices, respectively. By comparing S6-a and S6-b, it is known that the S6-b as the ground state at low $J_{\rm AF}$ region is caused by the PBCs of finite size lattice, which should be taken oven by the FM one in an infinite lattice.Riera et al. (1997); Kaplan and Mahanti (1997); Zang et al. (1997) In other words, here the S6-b region should also be FM. 16

2.2 (Color online) Spin patterns of four phases: (a) E-AFM; (b) $C_{1/3}E_{2/3}$; (c) $SOS_{1/3}$; (d) Triangle-AFM. Two types of coordinate axes ($x-y$ for the pseudo-cubic notation and $a-b$ for the orthorhombic $Pbnm$ notation) are shown in (a). 17

2.3 (Color online) (a) Ground state phase diagram at doping $x = 1/3$. The phase boundaries are obtained via the variational method plus the zero-T lattice optimization. The full dots denote MC simulation results which confirm the optimization calculation. Open dots are cases where the MC simulation does not provide a clear spin structure factor, which usually occur near phase boundaries where MC convergence is difficult due to the phase separation tendency. MC calculations were done at $T = 0.002$. 18

2.4 (Color online) The DOSs of e_g electrons: (a) $SOS_{1/3}$ phase (at $\lambda = 0$); (b) $C_{1/3}E_{2/3}$ phase (at $\lambda = 0.8$, obtained after the zero-T optimization of lattice distortion). 18

2.5 (Color online) Zero-T charge and orbital ordering of the $C_{1/3}E_{2/3}$ ($\lambda = 0.8$) and $SOS_{1/3}$ ($\lambda = 0$) phases, obtained via the lattice optimization calculation. The e_g density of each line (along $\vec{a}$-axis) is shown, which also depends on λ. 19

2.6 (Color online) Spin patterns: (a) $C_{1/3}E_{2/3}$-A; (b) $SOS_{1/3}$-A; (c) $C_{1/3}E_{2/3}$-B; (d) $SOS_{1/3}$-B. Comparing with the original $C_{1/3}E_{2/3}$-C and $SOS_{1/3}$-C ones (shown in Fig. 2.2), the first and second stripes stay the same(from left to right). All spins in the third and forth stripes of (a) and (b), the third stripe of (c) and (d) are reversed. 21

2.7 (Color online) The spin structure factors: (a) $SOS_{1/3}$-A and $C_{1/3}E_{2/3}$-A phases. The main peaks appear at wavevector $2\pi(1/4,1/4)$ and $2\pi(3/4,3/4)$, with an amplitude 5/18, while the weaker peaks appear at $2\pi(1/12,5/12)$, $2\pi(5/12,1/12)$, $2\pi(11/12,7/12)$, and $2\pi(7/12,11/12)$, with an amplitude 1/9. (b) $C_{1/3}E_{2/3}$-C phase. The main peaks appear at wavevector $2\pi(1/6,1/3)$ and $2\pi(5/6,2/3)$, with an amplitude 4/9, while the weaker peak appear at $2\pi(1/2,0)$, with an amplitude 1/9. (c) $SOS_{1/3}$-C phase. The main peaks appear at wavevector $2\pi(1/6,1/3)$, $2\pi(1/3,1/6)$, $2\pi(5/6,2/3)$ and $2\pi(2/3,5/6)$, with an amplitude 2/9, while the weaker peaks appear at $2\pi(1/2,0)$ and $2\pi(0,1/2)$, with an amplitude 1/18. 23

2.8 (Color online) Energy deviation from the $SOS_{1/3}$-A for $SOS_{1/3}$-BC (Red line) and $C_{1/3}E_{2/3}$ states including the lattice optimization procedure, employing a small cluster of size $2\sqrt{2} \times 6\sqrt{2}$ for the actual calculation. Three degenerate $SOS_{1/3}$ -A, -B, -C states have exactly the same energy at large values of the electron-phonon coupling. And they are the ground states with $\lambda < 0.7$. For λ values between 0.7 and 1.4, the $C_{1/3}E_{2/3}$-A state becomes the ground state. 24

2.9 (Color online) Finite temperature MC results (at $J_{AF} = 0.175$ and $\lambda = 0$) for the $SOS_{1/3}$-A phase, on the 12×12 cluster. Each point is obtained by MC heating up the simulation starting with the ideal $SOS_{1/3}$ spin configuration. *Left axis*: FE polarization $|\vec{P}|$ per site, calculated using $\sum_{<i,j>}[\vec{e}_{i,j} \times (\vec{S}_i \times \vec{S}_j)]/L^2$. *Right axis*: amplitudes of the characteristic peaks in the spin structure factors. A 6×6 cluster calculation on $SOS_{1/3}$-C gives the transition temperature equal to 0.014 (~ 40 K). 24

2.10 (Color online) The charge and orbital orders of the $x = 1/2$, $1/5$, $1/6$ SOS_x and C_xE_{1-x} phases, obtained using variational and lattice optimization calculation. Both the CE and $SOS_{1/2}$ phases are calculated with zero electron-phonon coupling. At large coupling $\lambda = 1.8$, the $C_{1/5}E_{4/5}$ and $C_{1/6}E_{5/6}$ phases form lines of zero e_g density sites along the $\vec{a}$ direction in the middle of each E-AFM stripe. At $\lambda = 0$, the $SOS_{1/5}$ and $SOS_{1/6}$ phases show high electronic densities at the center of the stripes and low densities on the stripe domain walls. 26

2.11 Energy deviation from the $C_{1/2}E_{1/2}$ (CE) for $SOS_{1/2}$ state including the lattice distortion optimization. Note that here the $SOS_{1/2}$ phase always has a higher energy. Therefore, in Ref. Giovannetti et al. (2009), an additional Coulomb U is required to stabilize the $SOS_{1/2}$ state. . . 27

2.12 (Color online) (a) Ground state phase diagram obtained via the zero-T variational calculation with lattice optimization, at hole doping $x = 1/5$. (b) DOSs of the $SOS_{1/5}$ ($\lambda = 0.0$) and $C_{1/5}E_{4/5}$ ($\lambda = 1.8$) phases. All these phases have a gap at the Fermi level. For the $SOS_{1/5}$ case ($\lambda = 0.0$), the gap is about 0.2 (~ 0.1 eV), while for $C_{1/5}E_{4/5}$ ($\lambda = 1.8$) the gap is 2.0 (~ 1.0 eV). 28

2.13 (Color online) (a) Ground state phase diagram obtained via the variational calculation with lattice optimization at hole doping $x = 1/6$. (b) DOSs of the $SOS_{1/6}$ ($\lambda = 0.0$) and $C_{1/6}E_{5/6}$ ($\lambda = 1.8$) phases. All these phases have a gap at the Fermi level. For the case of SOS, the gap is about 0.2 (~ 0.1 eV) ($\lambda = 0.0$), while for $C_{1/6}E_{5/6}$ ($\lambda = 1.8$) the gap is 2.0 (~ 1.0 eV). 29

2.14 (Color online) Finite-T MC results (at $J_{\rm AF} = 0.175$, $\lambda = 0.0$) for the $\rm SOS_{1/6}$ phase on the $L = 12$ cluster. Each point is obtained by a MC heating up calculation starting with the ideal $\rm SOS_{1/6}$ spin configuration. The ferroelectric polarization approaches the $\sqrt{2}/6$ limit at low temperatures. This temperature dependent curve shows that the $\rm SOS_{1/6}$ phase has a transition temperature of 0.034 ($\sim$ 190 K). 30

2.15 (Color online) The average spin structure factor of the $\rm C_xE_{1-x}$ (top picture) and $\rm SOS_x$ (bottom picture) degenerate states. Including the degenerate states with two opposite spin arrangements of each E-AFM stripe in $8N\sqrt{2} \times \sqrt{2}$ ($x = 1/N$) cluster, The average spin structure factor of 2^{16} degenerate $\rm SOS_x$ states present broad peaks along the (π, 0) and (0, π) direction. Neglecting that the lattice distortion may break the degeneracy of $\rm C_xE_{1-x}$, the average spin structure factor of $\rm C_xE_{1-x}$ shows quite similar spin structure factor as the $\rm SOS_x$ states. . 32

3.1 The MC results for the spin structure factor $S(\pi, \pi, \pi)$ and the AF-magnetization $\langle M \rangle$, for the case of the 3D isotropic Heisenberg model with all couplings equal to 1. Both curves indicate a Néel critical temperature $\rm T_N \sim 1.6$. 36

3.2 The comparison between the MC results and the mean-field calculation predictions, for the 3D isotropic Heisenberg model. The $\rm T_N$ of the mean-field calculation is 2.0 (no fluctuations included here), while the more accurate $\rm T_N$ of the MC calculation is approximately 1.55. . . . 37

3.3 The magnetization curve and the magnetic susceptibility (χ_M) curve using a $12 \times 12 \times 12$ lattice, and the 3D isotropic Heisenberg model. The $\rm T_N$ that can be estimated from $\langle M \rangle$ is just slightly higher than the $\rm T_N$ that arises from χ_M, for the case of the isotropic 3D Heisenberg model. 38

3.4 The comparison of $T_N(\chi_M)$ obtained with different lattice sizes, for the 3D isotropic Heisenberg model. The $T_N(\chi_M)$ tends to drop slightly below 1.5 in the thermodynamic limit. 39

3.5 Magnetization vs. temperature with different lattice sizes, for the 2D isotropic Heisenberg model. The L= 6, 8, and 20 calculations are for 3D lattices with $J_x = J_y = 1.0$ and $J_z = 0.0$, while the L= 20 and 30 calculations used 2D lattices with $J_x = J_y = 1.0$. 40

3.6 The convergence tendency of the critical temperatures $T_N(\chi_M)$ with different lattice sizes, for the case of the two-dimensional Heisenberg model (note that the 3D label just denotes that the simulation was done with a 3D cluster, but using $J_z = 0$). The critical temperature appears to extrapolate to a finite number, but note that the curvature of the fit suggests the possibility, anticipated by the Mermin-Wagner theorem, that the critical temperature will sharply drop and reach zero in the bulk. 41

3.7 The temperature dependence curve of $S(\pi, \pi)$, M, χ_M, and specific heat C_v using a 2D L=10 lattice, and the isotropic Heisenberg model. The comparison of C_v with Shuai Dong's result is also shown. 42

3.8 MC calculations for the anisotropic 3D Heisenberg model with two sets of values for the couplings as a test to compare with previous literature: (a) $J_z = 0.5$, $J_x = J_y = 1.0$ and (b) $J_z = 0.1$, $J_x = J_y = 1.0$, on a $10 \times 10 \times 10$ lattice. 43

3.9 MC calculations for the anisotropic 3D Heisenberg model with two sets of J values: (a) are results for the J's corresponding to the R-phase (L=10). Here, both the specific heat and magnetization give similar results. (b) Results for the couplings corresponding to the T-phase, using a L=10 lattice. Here, $T_N(\chi_M)$ of the T-phase appears to be equal to 1.2 from the magnetization analysis, but the specific heat has the peak at a higher temperature. For the R-phase (a), we have done 10 K MC thermal steps and 10 K measurement steps at each temperature. For the T-phase (b), we have done 20 K MC thermal steps and 40 K measurement steps at each temperature. More specifically, the magnetic susceptibility was measured under 30 K MC thermal steps and 100 K measurement steps at each temperature. In each MC step, the number of spin flips is doubled to improve the accuracy of $T_N(\chi_M)$. 46

3.10 MC calculations on a two-dimensional lattice with J_x and J_y equal to the values in the T-phase. For (a), we have done 10 K MC thermal steps and 40 K measurement steps at each temperature, using a 10×10 two-dimensional lattice. For (b), we have done 10 or 20 K MC thermal steps and 80 or 300 K measurement steps at each temperature using a 30×30 two-dimensional lattice. Note the move toward lower critical temperatures between (a) and (b) by increasing the lattice size. This is to be expected when using two-dimensional systems. 47

3.11 MC calculations for the 3D anisotropic Heisenberg model with two sets of J values: (a) R-phase (L=12), (b) T-phase (L=12). For the R-phase (a), we have used 10 K MC thermal steps and 10 K measurement steps at each temperature. For the T-phase (b), we have used 30 K MC thermal steps and 80 K measurement steps at each temperature. . . . 50

3.12 Magnetization versus MC measurement steps (i.e. MC "time" evolution) for a 3D lattice close to the Néel temperature: (a) corresponds to the R-phase with T=1.4, and L=12. Here the fluctuations are reasonable. So this R-phase involves no problems at all; (b) corresponds to the T-phase at T=1.15, and L=12. Here the fluctuations are much wilder. This is also clear from the large value of the magnetic susceptibility in the T-phase, as previously discussed. 51

3.13 MC calculations for the T-phase using a three-dimensional lattice of linear size $L = 16$. We have used 50 K MC thermal steps and 200 K measurement steps (4K measurement steps for the S(k)) at each temperature. Notice that the $S(\pi, \pi, \pi)$, χ_M and $\langle M \rangle$ curives shows the same Néel temperature at about 0.95. 52

3.14 MC calculations for the T-phase using a three-dimensional lattice of linear size $L = 20$. We have used 50 K MC thermal steps and 200 K measurement steps at each temperature. 52

3.15 The convergence tendency of the critical temperatures $T_N(\chi_M)$ deduced from the magnetic susceptibility for three different cases. Shown are the two-dimensional T-phase (just one plane), the three-dimensional T-phase, and the three-dimensional R-phase. We can see a clear tendency of T_N to drop with increasing the lattice size. However, compared to the T-phase, the 3D R-phase has a much smaller finite size effect. Assuming the T_N of the R-phase in the bulk limit is 640 K, the corresponding T_N of the 3D T-phase should be approximately 200 K. 53

3.16 The comparison between four different calculations. The magnetic susceptibility of the T-phase using a $6 \times 6 \times 6$ three-dimensional lattice with $J_z = 0$ is found to diverge at low temperature (red curve). This strange behavior is explained in the text. The susceptibility of just one layer of spins (black curve) extracted from the 3D study is equal, as expected, with that of an isolated 6×6 2D lattice (blue curve). The green curve is for a $6 \times 6 \times 6$ 3D T-phase with the realistic coupling $J_z = 0.1013$. These calculations are done using $6 \times 6 \times 6$ 3D lattices and a 6×6 2D lattice. We have used 10 K MC thermal steps and 200 K measurement steps at each temperature. Note the somewhat paradoxical result that the peak in the 2D study is at a higher T than the 3D T-phase, but remember than in 2D there are huge size effects. 54

3.17 The comparison between the MC results for a T-phase system with J_z=0, and mean field calculations. The χ_M from the mean-field calculation is equal to $4/T$. The χ_M of MC calculation has a lower value only at high temperatures where in-plane spin fluctuation reduces the total magnetic order, but at low T there is good agreement. Then, the divergence comes from the decoupling of the planes, with each one behaving like an independent spin, as explained in the text. 55

3.18 The convergence tendency of the critical temperatures $T_N(\chi_M)$ deduced from the magnetic susceptibility for three different cases. Shown are the two-dimensional T-phase (just one plane), the three-dimensional T-phase, and the three-dimensional R-phase. 57

3.19 Sample spin configurations with $2 \times 2 \times 2$ lattice size. The z-direction AFM order requites a lower Néel temperature than that is required to stabilize a G-AFM order in each x-y plane. The two green and red spin configurations represent two near degenerate states with tiny energy difference from the J_z coupling. They both have G-AFM order in each x-y plane. But the opposite z direction spin arrangement gives out different M_{stagg} and spin structure factor. Only a lower temperature can break this near degeneracy. 58

3.20 The comparison between the staggered magnetization $\langle M \rangle$ and spin structure factor $S(\pi, \pi, \pi)$, using a 3D anisotropic Heisenberg model with L=6. The results shown are for (a) R-phase and (b) T-phase. For both calculations, we have used 10 K MC thermal steps and 400 K measurement steps at each temperature. Note that in (b) the temperature where both magnetization and spin structure factor change the sign of their *curvature*, often taken as indication of a critical temperature in numerical studies using a finite lattice, is very similar to the location of the peak in the magnetic susceptibility. 59

4.1 (a) Detwined sample with uniaxial Pressure along the FM direction. (b) Resistivity along AF direction is smaller than that along the FM direction with a $(\pi, 0)$ magnetic order. 62

4.2 Band structure of the tight binding Hamiltonian from Ref. [Daghofer et al. (2010b)]. The chemical potential is adjusted to n=4/3. At the Fermi energy, there are two hole pockets at the Gamma point, and two electron pocket at the X and Y points. 65

4.3 (color online) (a) Classical spins structure factor S(π,0) (normalized to 1) vs. T, for the $J_{\rm H}$'s indicated, using the PBC 8×8 cluster and $J_{\rm NN}$=0.015. The oscillations in the data are indicative of the error bars. (b) Density of states $N(\omega)$ of each orbital (μ= chemical potential), using TBC with L=512, at T=0 K and $J_{\rm H}$=0.1 eV, for the perfect $(\pi, 0)$ magnetic state. (c) Resistance R vs. L (TBC 8×8) for the FM and AFM directions of the perfect $(\pi, 0)$ magnetic state ($J_{\rm H}$=0.1 eV). (d) The occupation at the FS $n(\mu)$ (see text) of the three orbitals vs. T, using L=256. A coupling $J_{\rm NN}$=0.016 (0.014) along the x (y) axis was used (see text). 67

4.4 (color online) $A(\mathbf{k}, \omega)$ at ω=μ (TBC 8×8 L=512). The model used (see Ref. Daghofer et al. (2010b)) includes the staggered As modulation out of the FeAs layer. Thus, our results are in the *folded* Brillouin zone convention, and for this reason two electron pockets (as opposed to just one) are centered at X in the panels above. The pocket elongated vertically at X would corresponds to a pocket at Y in the unfolded convention if the As modulation is considered via a quasicrystal momentum Daghofer et al. (2010b). (a-c) are for $J_{\rm H}$=0.1 eV. Red, green, and blue are for the xz, yz, and xy orbitals, respectively. (a) T=40K, below $T_{\rm N}$. The $(\pi, 0)$ magnetic order induces yz-orbital electron satellite pockets. (b) T=110$K\sim T_{\rm N}$. In this regime, the MC configurations display small coexisting patches of $(\pi, 0)$ and $(0, \pi)$ order (see text), creating almost symmetric xz and yz features around Γ. (c) Large T=360 K, with no remnants of the $(\pi, 0)$ order. The FS becomes a broaden version of the non-interacting FS at $J_{\rm H}$=0, shown in (d) at T=100 K. 69

4.5 (color online) Resistance R of the SF model calculated via MC simulations, at $J_{\rm H}$=0.1 eV and using the L=256 TBC 8×8 cluster. $T_{\rm N}$ is indicated, and the magnetic susceptibilities χ_S are also shown. The FM-AFM directions asymmetry is evident at low T (note that the FM and AFM labels simply refer to the y and x directions, respectively, and not to fully FM or AFM spin configurations). As T increases the symmetry is restored, and the curves display a peak at $T_{\rm N}$. A small symmetry-breaking difference $r_{\rm NN}$=1.14 is used (see text). In green (dashed line) are the results for random spin configurations, showing that their R is smaller than in the MC results near $T_{\rm N}$. The width of the χ peaks extend to $\sim$1.5$T_{\rm N}$, in agreement with neutron scattering for $CaFe_2As_2$ Diallo et al. (2010). 70

4.6 (color online) Resistance R calculated using a L=64 TBC 16×16 cluster, with $J_{\rm NN}$=0.032 (0.028) along the x (y) axis. The spin configurations are generated via $H_{\rm Heis}$, while the R measurements use the full $H_{\rm SF}$, at $J_{\rm H}$=0.1 eV. The rest of the notation is as in Fig. 4.5. 72

4.7 (color online) (a) Typical MC-generated classical spin configuration on an 8×8 cluster at $T_{\rm N}\sim$110 K, $J_{\rm H}$=0.1 eV, and $J_{\rm NN}$=0.016 (0.014) along the x (y) axis. The red (blue) lines denote AFM (FM) NN correlations, of intensity proportional to the width. (b) The dominant orbital at the FS at each site for the configuration used in (a), calculated using $n(\mu)$ as in Fig. 1(d). Red (green) denote the xz (yz) orbital, with a size proportional to the density. 74

A.1 The d electron degeneracy is broken under a crystal field. (a) Octahedral structure with one Mn in the center and eight Oxygen atoms along the x, y and z axis. (b) Tetrahedral structure with one Fe atom in the center and four Arsenic atoms around it. These figures are reproduced from wikipedia. 89

A.2 e_g d orbitals: $x^2 - y^2$, $3r^2 - z^2$. This figure is courtesy of Alexander Pruell. 89
A.3 t_{2g} d orbitals: yz, xz and xy. This figure is courtesy of Alexander Pruell. 90
A.4 The energy levels of the e_g and t_{2g} d electrons vary under different types of crystal fields. These figures are reproduced from http://scienceworld.wolfram.com. 90

Chapter 1

Introduction

1.1 General Introduction to Multiferroic Manganites

In the first portion of this manuscript, the colossal magnetoresistance (CMR) effect of manganites will be reviewed, and then the main new subjects of research will be discussed. Manganites have potential use in the computer industry if the CMR effect could occur at room temperature. The CMR effect was initially observed in materials such as $La_{0.75}Ca_{0.25}MnO_3$, in which the resistivity changed dramatically when applying magnetic fields of a few Teslas Schiffer et al. (1995). Near the Curie temperature, there is a sharp transition from metal to insulator with temperature increasing above T_c As shown in the middle graph of Fig[1.1], the height of the resistivity peak drops significantly when magnetic fields are applied. Current understanding of this CMR effect involves the existence of nano length scale clusters of the FM phase separated by insulator domain walls Dagotto et al. (2001). This is related with the explanation of this phenomenon based on phase separation tendencies, due to phase competition in the bulk. In other words, work by our group and others have shown that it is the competition between a FM metallic phase and an insulating phase that creates the resistivity peak in the curve. By applying

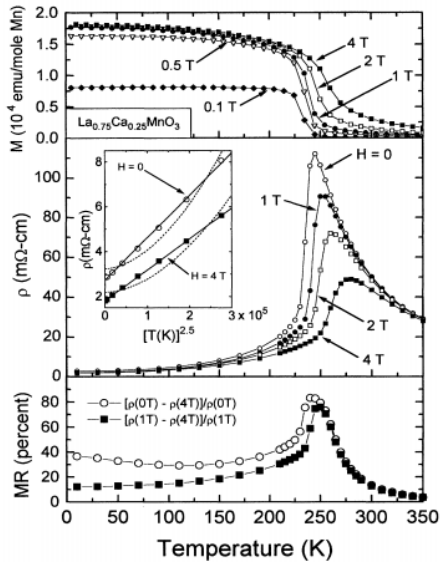

Figure 1.1: The magnetization, resistivity, and magnetoresistance of $La_{0.75}Ca_{0.25}MnO_3$ as a function of temperature at various fields. This figure is reproduced from Ref.[Schiffer et al. (1995)]

a magnetic field into the state with the FM nanoclusters having randomly oriented magnetizations, all these FM nano clusters are then aligned into the same orientation, thus rendering the entire ensemble ferromagnetic and conducting.

1.1.1 Multiferroics

A natural next-step evolution involving electronic devices would involve the meld of magnetism and ferroelectricity into a single compact and sensitive unit (a multiferroic material). However, it is quite difficult to combine these two properties into one single material. Magnetism is typically related to incomplete ionic shells, while ferroelectricity is related to the shift of ions to produce an electric moment (Fig.[1.2]). Several ferroelectric and magnetic materials are transition metal oxides. The magnetism is caused by the unfilled d shells. These two states involved in multiferroics have different symmetry properties. For example, a ferromagnetic state obeys space reversal symmetry but violates time reversal symmetry, while a ferroelectric states obeys time reversal symmetry but violates space reversal symmetry. For instance, the

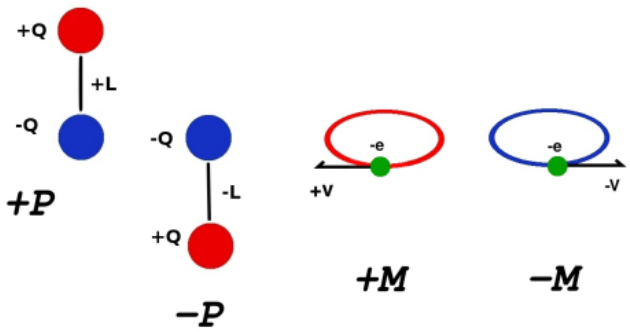

Figure 1.2: The comparison between spatial reversal symmetry and time reversal symmetry shows that ferroelectricity is generated with different symmetry breaking properties as magnetism.

electric dipole moment is shown as $P = Q \times L$ in Fig.[1.2] where the dipole moment P will change sign if space L is reversed which means the space reversal symmetry is violated. As a result, having dipole moments in a material in a ferroelectric state is not enough to produce multiferroics.

Multiferroics are promising materials that have the unique property of coexisting ferroelectricity and magnetism. The focus of this manuscript will be on the manganese oxides called manganites. There are two ways in which multiferroics can occur in the family of manganites: (1) via the intrinsic presence of both orders simultaneously in the material or (2) via the creation (spontaneously or artificially) of heterostructures consisting of ferroelectric and magnetic materials coupled together. In this manuscript, we will explore these amazing materials. First, we will introduce experimental results in the area of manganite multiferroics. Then, we will discuss how to use theoretical computational methods to better understand both of the phenomena above. Finally, we will discuss a set of new phases in these materials which have the ferroelectric and magnetic properties discussed before.

They also have different symmetries. Ferromagnetism obeys space reversal symmetry but violates time reversal symmetry, while ferroelectricity obeys time reversal symmetry and violates space reversal symmetry. Multiferroics require to have

both the space and time symmetry violation at the same time. In this manuscript, multiferroics induced by special magnetic ordering will be discussed.

1.1.2 Magnetic ferroelectricity in frustrated magnets

One particular group of manganites has the chemical formula $RMnO_3$, where R is a rare-earth element. This subfamily is sometimes referred to as the "undoped" manganites since there is no divalent ion in the chemical formula, such as Sr or Ca, that upon replacing R could create hole carriers in the material. A remarkable experimental result is that some of these undoped manganites materials exhibit an electric polarization which is caused by a special spiral-like spin arrangement observed experimentally, that theorists believe is itself induced by the phenomenon of spin frustration. The coupling between ferroelectricity and magnetic ordering is caused by the spin-orbital coupling. More specifically, in this class of materials the spin-orbital coupling creates a very weak Dzyaloshinskii-Moriya (DM) interaction that shifts the oxygen atoms away from the Mn plane (see Fig. [1.3]) Sergienko and Dagotto (2006). The DM interaction violates the space-inversion symmetry of the oxygen atoms which creates ferroelectricity (Fig. [1.4]). In this case, an applied magnetic field will be the driving force to twist the $RMnO_3$'s magnetic order and, as a consequence, also rotate the direction of ferroelectricity through the spin-orbital coupling.

Multiferroic spiral phases of $RMnO_3$

As shown in Fig. [1.5], experiments show results that have a dependence on the rare earth ion size and the Mn-O-Mn bond angle. The smaller the ion is, the more the Mn-O-Mn bond is bended. With the ion size decreasing, this graph also shows a phase change from an A-AFM state to a spiral phase which is ferroelectric, and then to an E-AFM state. The modifications of the bond bending angle by chemical doping directly result in the modifications of the superexchange coupling. The experimental discovery of manganites multiferroics with spiral phases Goto et al. (2004) motivated several

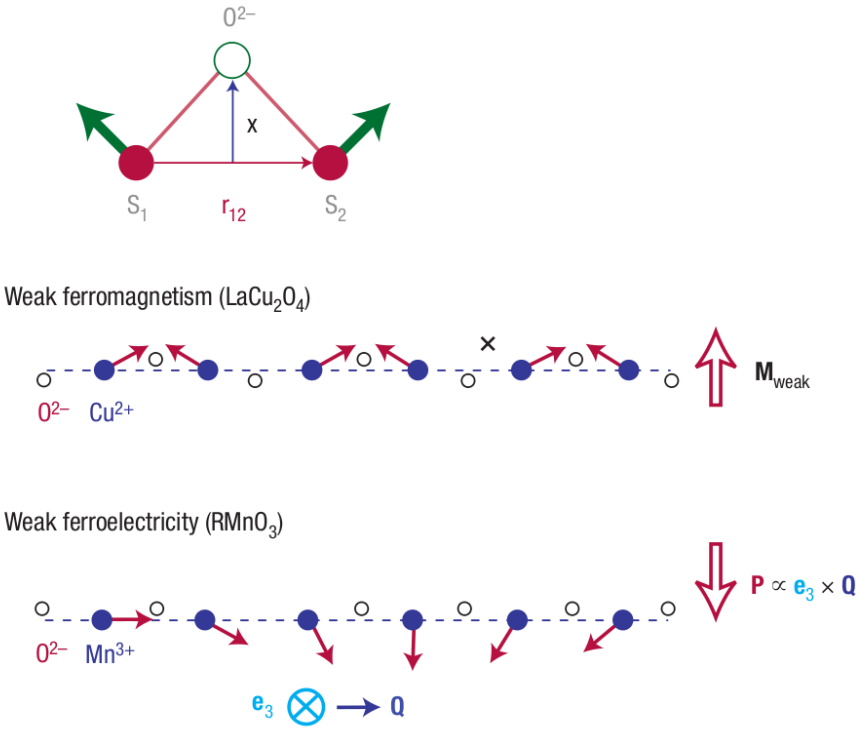

Figure 1.3: Figure illustrating the Dzyaloshinskii-Moriya interaction $H_{\rm DM} = \lambda x \times \vec{r}_{12} \cdot [S_1 \times S_2]$ which tends to move the oxygen atoms away from the straight bond Mn-O-Mn defined by r_{12}. The symmetry properties of the DM interaction indicate that only spin configurations with nonzero cross product between nearest-neighbor spins will induce ferroelectricity. In particular, spiral spin configurations will shift every oxygen atom into the same direction, thus inducing a total nonzero polarization. This figure is reproduced from Ref.[Cheong and Mostovoy (2007)].

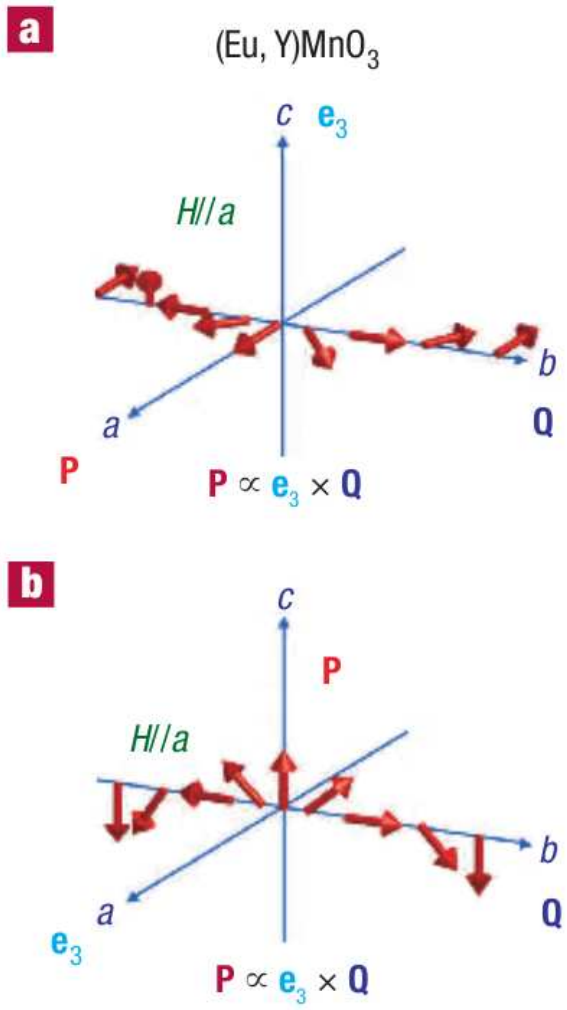

Figure 1.4: Illustration on how a perovskite $RMnO_3$ with spiral magnetic order polarization is rotated by an applied magnetic field. Spiral spins prefer to be perpendicular to strong magnetic fields. Then, if the (a) spiral spins are in the $a-b$ plan, the polarization is along the a axis. But (b) after applying a magnetic filed along the a axis, the spins rotate into the $b-c$ plane which causes the polarization P to rotate 90 degrees. This figure is reproduced from Ref.[Cheong and Mostovoy (2007)].

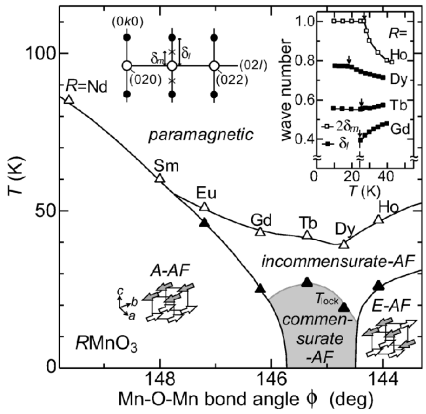

Figure 1.5: Phase diagram of $RMnO_3$. Left upper inset shows a schematic view of reciprocal space. The right upper inset shows the wave numbers of the modulated crystallographic structures in a-b plane. The main portion of the figure shows the phase diagram including the A-AFM phase, the spiral-AFM state, and the E-AFM state as the Mn-O-Mn bond angle ϕ varies. This figure is reproduced from Ref[Goto et al. (2004)].

theorists to try to explain the spiral spin phenomena. At present, there are several different ways of explaining how this spiral spin appeared in this phase diagram.

It can be analytically and computationally shown that spiral order can be reached by the competition between a nearest-neighbor spin coupling, $J_{\rm FM}$, which is negative and next-nearest coupling, $J_{\rm AFM}$, which is positive. However, this is simply a phenomenological procedure with no microscopic basis. Another way to arrive to the spiral order is by setting a very large DM interaction, but this requires a much larger spin-orbit coupling strength than believed to be realistic. Thus, the most natural and realistic procedure to create a spiral configuration in theoretical calculations is by using a double-exchange model which also contains a (asymmetric) next-nearest neighbor super-exchange coupling which originates in lattice distortions Dong et al. (2008b) Dong et al. (2008a). This previous work has been done by Shuai Dong and collaborators using mainly a Monte Carlo method. The Hamiltonian of the double-exchange model with infinite Hund coupling is schematically given by:

$$H = H_{\rm DE} + H_{\rm SE} + H_{\rm JT} \tag{1.1}$$

In this model, $H_{\mathrm{DE}} = -\sum t_r^{\alpha\beta}\Omega_{ij}c_{i\alpha}^{\dagger}c_{j\beta}$ is the double-exchange energy term which is also called the kinetic energy term. Here, $t_r^{\alpha\beta}$ is the hoping amplitude between orbitals α and β along direction $r = x, y, z$. The superexchange term is given by $H_{\mathrm{SE}} = \sum J_{ij}^{c}\mathbf{S}_i \cdot \mathbf{S}_j$. Because of the lattice distortions that stretch the b axis of the manganese plane, the next-nearest neighbor (NNN) superexchange is different in the a and b directions. Although the next-nearest coupling J_{NNN} is small, the symmetry along a and b axes is broken. The third term H_{JT} represents the coupling of e_g electrons with the lattice, via the Jahn-Teller (JT) mode. DM interaction is treated as a perturbation based on its small experimentally observed value Deisenhofer et al. (2002).

Chapter 2

Striped Multiferroic Phases in Narrow Bandwidth Hole-Doped Manganites

2.1 Introduction

In recent years, the family of compounds known as the manganites has attracted considerable attention from the research community. This interest arises from the colossal magnetoresistance effect that the manganites exhibit and also from the multiferroic properties of some of these manganese oxides. The rich phase diagrams of manganites suggest that there are several competing phases with close free energies but very different physical properties. This provides a unique playground to investigate the basic physics of strongly correlated electronic systems in general. It also offers the opportunity to find materials with useful technological applications Dagotto (2005).

Multiferroics, especially the magnetic multiferroics (the so-called type-II multiferroics) Khomskii (2009) has become a hot area of research in the community of condensed matter physics and material science Fiebig (2005); Cheong and Mostovoy

(2007); Kimura (2007); Wang et al. (2009). In magnetic multiferroics, the ferroelectric (FE) polarization is driven by some particular spin orders, that can be controlled by a magnetic field.

However, there are several critical issues preventing the technical applications of magnetic multiferroics. One critical problem is that the multiferroic Curie temperatures (T_C's) are very low (mostly below 50 K). Very recently, Kimura *et al.* made great progresses on new magnetic multiferroics with relative high T_C's, including CuO Kimura et al. (2008) and $Sr_3Co_2Fe_{24}O_{41}$ Kitagawa et al. (2010), the later of which shows a low-field magnetoelectric effect at room temperature (T). Another critical fact is that the FE polarizations in magnetic multiferroics are usually quite weak. A large branch of magnetic multiferroics involves those with spiral (or conical) spin order Kimura (2007), in which the FE polarization is induced by the inverse Dzyaloshinskii-Moriya (DM) interaction. However, the DM interaction is naturally weak due to its relativistic origin Katsura et al. (2005); Sergienko and Dagotto (2006); Xiang et al. (2008); Malashevich and Vanderbilt (2008). An alternative way to obtain FE polarization in magnetic multiferroics is the exchange striction (ES) effect. For example, the FE polarizations in E-type antiferromagnetic (E-AFM) manganites was predicted to be higher than ~ 1 $\mu C/cm^2$ Sergienko et al. (2006); Picozzi et al. (2007), and the latest experiments have already confirmed their large FE polarizations Ishiwata et al. (2010), although the values have not reached the theoretical one due to the polycrystalline samples used and high coercive fields. Thus, to search for new magnetic multiferroics, especially those with new mechanisms to improve the above discussed limits, is the most important issue in the current stage of research.

Very recently, we predicted a multiferroic *spin-orthogonal stripe* (SOS) phase for quarter-doped manganites in the narrow-bandwidth region.Dong et al. (2009) The noncollinear spin structure in the SOS phase is not due to the traditional next-nearest neighbor (NNN) exchange frustration, but the competition between the nearest neighbor (NN) double-exchange (DE) and superexchange (SE). Thus, a relative high multiferroic T_C (~ 100 K) is expected for the SOS phase. Meanwhile,

others predicted a multiferroic state in half-doped manganites, which also showed noncollinear *spin stripe* structure and a large FE polarization Giovannetti et al. (2009). These theoretical investigations may open an alternative route to pursue new magnetic multiferroic families with better performance.

In this chapter, the narrow-bandwidth manganites with other dopings, in one of our publications Liang et al. (2011), will be investigated systematically by using the two-orbital DE model. There are five interesting aspects of the problem. First, more magnetic multiferroic phases have been discovered. Second, both the DM interaction and ES effect can induce FE polarizations in these phases. Third, a systematic SOS_x family has been revealed in narrow-bandwidth manganites from the half-doping case to the undoped case. Fourth, the new discovered FE states and non-FE states can be very close in energies (even degenerate), allowing for the manipulations of multiferroic states with low fields. Last but not least, the number of degeneracy of the new SOS_x phases may be macroscopic, which is different from neither normal ordered materials nor spin ice systems Bramwell and Gingras (2001).

2.2 Model and Methods

2.2.1 Model

The Hamiltonian used in this effort is defined as:Dagotto et al. (2001); Dagotto (2002)

$$\begin{aligned} H &= -\sum_{<ij>}^{\alpha,\beta} t_r^{\alpha\beta}(\Omega_{ij} c_{i\alpha}^{\dagger} c_{j\beta} + H.c.) + \sum_{<ij>} J_{\mathrm{AF}} \vec{S}_i \cdot \vec{S}_j \\ &\quad +\lambda \sum_i (-Q_{1i} n_i + Q_{2i} \tau_i^x + Q_{3i} \tau_i^z) \\ &\quad +\frac{1}{2} \sum_i (2Q_{1i}^2 + Q_{2i}^2 + Q_{3i}^2), \end{aligned} \tag{2.1}$$

where the first term represents the two-orbital DE hopping of e_{g} electrons, widely used in the context of manganites. The limit of an infinite Hund coupling is

already assumed in this term. The parameters $t_r^{\alpha\beta}$ are the hopping amplitudes between the orbitals α and β, which represent the active e_g orbitals $a = d_{x^2-y^2}$ and $b = d_{3r^2-z^2}$ of the manganese cations. Since our study below, for computational simplicity, will be restricted to two-dimensional (2D) lattices, then r represents the hopping directions x and y. More explicitly, the hopping parameters are: $t_x^{aa} = t_y^{aa} = \frac{3}{4}t_0$, $t_x^{bb} = t_y^{bb} = \frac{1}{4}t_0$, $t_x^{ab} = -\frac{\sqrt{3}}{4}t_0 = -t_y^{ab}$, as explained in detailed in previous publications Dagotto et al. (2001); Dagotto (2002). The energy unit is $t_0 = 0.2 - 0.5$ eV for typical manganites. The Berry phase factor has the form $\Omega_{ij} = \cos(\theta_i/2)\cos(\theta_j/2) + \sin(\theta_i/2)\sin(\theta_j/2)\exp[-i(\phi_i - \phi_j)]$ and it effectively modifies the hopping amplitude for an e_g electron to hop to the NN site due to the t_{2g} electron spin ($\vec{S}$) orientations, regulated by polar angles θ and azimuthal angles ϕ. For NNs sites with parallel (antiparallel) t_{2g} spins, the Berry phase factor for an e_g electron to jump from one site to the next becomes one (zero).

The second term represents the SE coupling between NN t_{2g} spins, which is represented as a Heisenberg model formula. The third terms represents the coupling of e_g electrons with the lattice, via the Jahn-Teller (JT) modes (Q_2 and Q_3) and breathing mode (Q_1), which can be written in terms of the coordinates of the six oxygens surrounding each manganese. λ is a dimensionless lattice-electron coupling coefficient. For a 2D lattice, only the $x - y$ plane distortions are considered here. Assuming the lattice shape (square) does not change, then the Q_1 becomes $-\sqrt{2}Q_3$ here. The lattice normal modes Q_2 and Q_3 are represented by the oxygen shifts δ^x, δ^y, and $\delta^z = 0$ as follows: $Q_2 = (\delta^x - \delta^y)/\sqrt{2}$ and $Q_3 = -(\delta^x + \delta^y)/\sqrt{6}$, and τ represents the pseudospin operators ($\tau_x = c_a^\dagger c_b + c_b^\dagger c_a$, $\tau_z = c_a^\dagger c_a - c_b^\dagger c_b$).

In the past decade, the above model was been extensively studied and proved to be a quite successful model to describe manganites.Dagotto (2002); Dagotto et al. (2001)

2.2.2 Numerical techniques

Variational, Monte Carlo (MC), and zero-T optimization methods are adopted in this work to solve the two-orbital DE Hamiltonian described above. The lattices studied here are 2D $L \times L$ squares and $\sqrt{2}L_1 \times \sqrt{2}L_2$ tilted rectangles with periodic boundary conditions (PBCs). Sometimes, an infinite size lattice is also simulated with the help of the twisted boundary conditions (TBCs) with dense k meshes Salafranca et al. (2009).

For given classical spin configurations, the variational method diagonalizes the Hamiltonians and compares the energies of all proposed states. This method is typically used for initial candidates selection and to guide the MC simulations. Only the phase with the lowest energy in the variational calculation has the chance to be physically correct, namely to be the possible ground state. By varying couplings like $J_{\rm AF}$, there may be energy crossings among variational candidates, indicating the presence of zero-T phase transitions.

The other technique used here extensively is the MC simulation. In this approach, the $e_{\rm g}$ sector is diagonalized exactly for a fixed set of lattice coordinates and classical spins. Via the MC procedure, those classical variables are updated until a thermal equilibrium is reached. In contrast to the variational method, it may be difficult to identify the "perfect" ground states using MC simulations because fluctuations always exist at finite-T's. Moreover, the MC calculation for the DE model used here is quite CPU-time consuming. However, MC simulations are crucially important since they are unbiased, i.e. not variational, and with sufficiently long runs they converge to the true thermodynamic relevant state of the system.

The third technique used here is the zero-T optimization. This technique is used to optimize the classical spins (θ_i, ϕ_i), and the oxygen lattice displacements (δ_i^x, δ_i^y). By taking derivatives of the Hamiltonian with respect to all generic variable q's (spin angles or lattice distortions) $\frac{\partial H(q)}{\partial q}$, the optimization method can get a lower energy by adjusting q's at the next step Yu et al. (2009b). In each step of the iteration, all

the variables are adjusted until $|\langle\frac{\partial H(q_i)}{\partial q_i}\rangle| \leq \epsilon$, where ϵ is a small number used as the criterium for convergence. This optimization method is particularly useful especially around a local minimum energy point at zero-T. Thus, an optimization following a low-T MC simulation is quite efficient to obtain the global energy minimum, and an optimization of lattice distortions with fixed spin configurations can be used to obtain the lowest energy of each phases.

2.2.3 Generation of ferroelectricity

In our model, two magnetic multiferroic mechanisms are considered. The first mechanism is the inverse DM interaction, involving the term $H_{\rm DM} = \lambda_{\rm DM} \sum_{ij} (\vec{\delta}_{ij}^{\perp} \times \vec{r}_{ij}) \cdot [\vec{S}_i \times \vec{S}_j]$, where $\vec{r}_{ij}$ is the unit vector linking two NN spins $\vec{S}_i$ and $\vec{S}_j$, $\vec{\delta}_{\perp}$ is the oxygen displacement perpendicular to the $i-j$ direction, and $\lambda_{\rm DM}$ is the strength of the DM coupling. This DM term tends to move the oxygen anion away from the midpoint of a Mn-Mn pair when a noncollinear spin pair appears, namely to change $\vec{\delta}^{\perp}$ Sergienko and Dagotto (2006). A simplified formula of FE polarization for noncollinear spin configurations is written as: $\vec{P}_{\rm DM} \propto \Sigma_{<ij>} \vec{r}_{ij} \times [\vec{S}_i \times \vec{S}_j]$ Katsura et al. (2005).

Another mechanism for ferroelectricity is the ES effect, which drives a relative large FE polarization in E-AFM $HoMnO_3$ Sergienko et al. (2006); Picozzi et al. (2007). In this case, $e_{\rm g}$ electrons gain extra DE energy from the Mn-O-Mn bond distortion. The total FE polarization amplitude can be simplified into a formula: $P_{\rm E} \propto \Sigma_{<i,j>} (-1)^{i_x+i_y} |\Omega_{ij}| \propto \Sigma_{<ij>} (-1)^{i_x+i_y} \sqrt{1+\vec{S}_i \cdot \vec{S}_j}$.

2.3 Results and Discussion

Following the discovery of the SOS (spin-orthogonal stripe) phase in the DE model for quarter-hole-doped ($x = 1/4$) manganites,Dong et al. (2009) the present effort aims

to extend those calculations to other hole-doping fractions and investigate whether similar multiferroic phases can emerge besides the quarter doping.

2.3.1 $\mathbf{SOS}_{1/3}$ and $\mathbf{C}_{1/3}\mathbf{E}_{2/3}$ at doping $x = 1/3$

As an example, a variational calculation at $\lambda = 0.0$ was carried out on a 6×6 square lattice, as shown in Fig. 2.1. By comparing the energies of the candidate states, it is known that the ground states transit from a ferromagnetic (FM) phase to a $\mathrm{SOS}_{1/3}$ state at $0.175t_0$. Note that there is a close competition between the $\mathrm{C}_{1/3}\mathrm{E}_{2/3}$ and $\mathrm{SOS}_{1/3}$ phases, since their energy difference is as small as $0.007t_0$. Besides the expected $\mathrm{SOS}_{1/3}$ phase, an unexpected triangle-type antiferromagnetic (Triangle-AFM) phase has also been found in the large J_{AF} region. The variational result is also confirmed by the MC simulation at low-T (dots in Fig. 2.1). The close proximity of those MC results and the variational calculations indicates that the true ground state has been identified. Some spin configurations adopted here are shown in Fig. 2.2.

With the help of zero-T optimization of lattice distortions, the variational method can be extended to finite λ cases. Then a ground state phase diagram can be obtained in the $J_{\mathrm{AF}} - \lambda$ parameter space, as shown in Fig. 2.3, which is further checked by MC simulations. The $\mathrm{SOS}_{1/3}$ state, as a natural generalization to $x = 1/3$ of the original $x = 1/4$ SOS state, is stable in almost the same area of the phase diagram. Similarly, the relevant $\mathrm{C}_{1/3}\mathrm{E}_{2/3}$ phase also appears at high-λ region.

The e_{g}'s density of states (DOSs) of $\mathrm{SOS}_{1/3}$ and $\mathrm{C}_{1/3}\mathrm{E}_{2/3}$ phases are calculated in an infinite size lattice, as shown in Fig. 2.4. Both phases have gaps at their Fermi levels. The gap of $\mathrm{SOS}_{1/3}$ is about $0.8t_0 \approx 0.16 - 0.4$ eV, guaranteeing the insulating properties. The gap of $\mathrm{C}_{1/3}\mathrm{E}_{2/3}$ is even a little larger, due to the presence of the JT distortion.

The orbital and charge orders of $\mathrm{SOS}_{1/3}$ and $\mathrm{C}_{1/3}\mathrm{E}_{2/3}$ are calculated, as shown in Fig. 2.5. For the $\mathrm{SOS}_{1/3}$ phase, the charge in the stripe center is higher than on

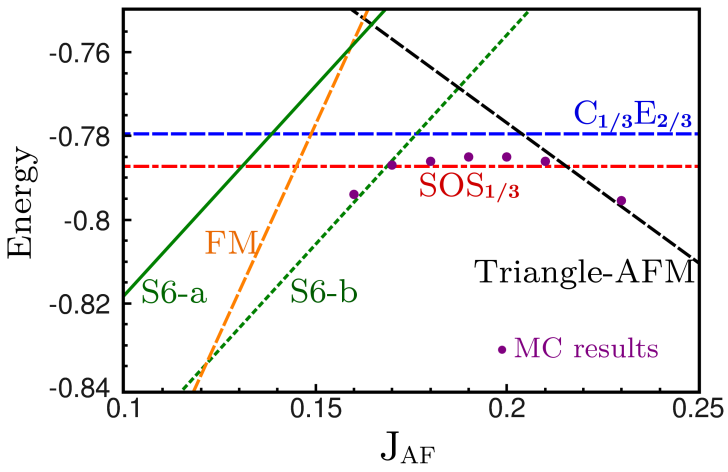

Figure 2.1: (Color online) An example of zero-T variational calculation: comparing the energies of several candidate spin orders at doping $x = 1/3$ and $\lambda = 0$ as a function of $J_{\rm AF}$. The dots represent MC results results at $T = 0.002$. S6-a (and S6-b) denote the spiral phase which's period is 6.Dong et al. (2008b) The energies of S6-a and S6-b are calculated in an infinite and $L = 6$ lattices, respectively. By comparing S6-a and S6-b, it is known that the S6-b as the ground state at low $J_{\rm AF}$ region is caused by the PBCs of finite size lattice, which should be taken oven by the FM one in an infinite lattice.Riera et al. (1997); Kaplan and Mahanti (1997); Zang et al. (1997) In other words, here the S6-b region should also be FM.

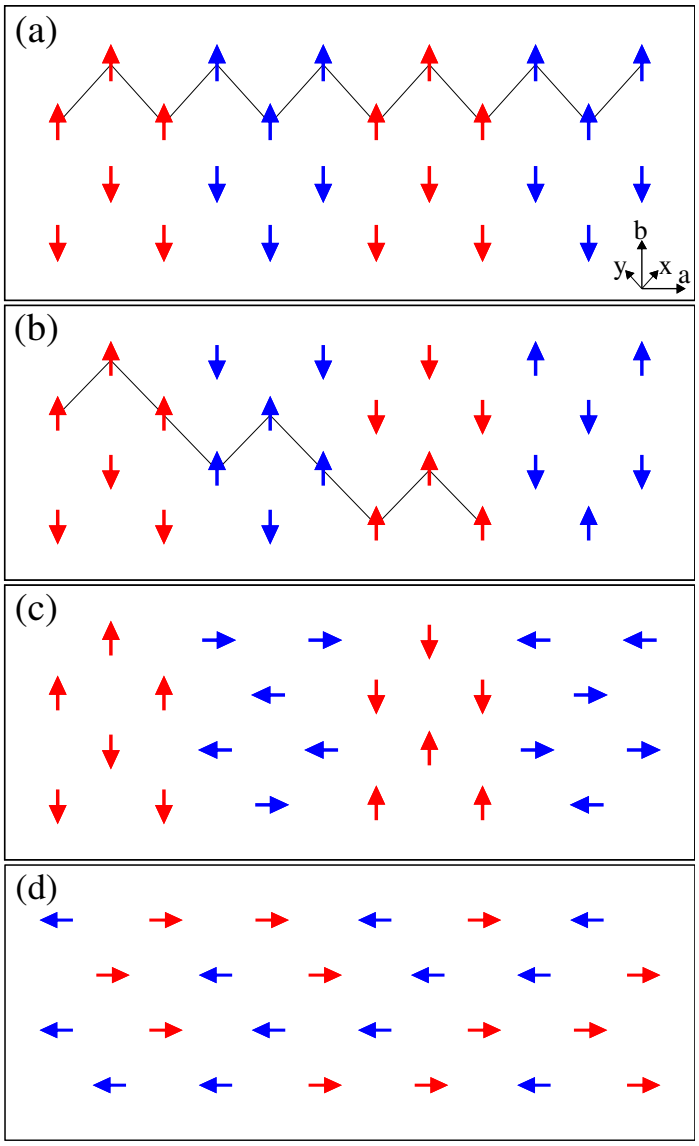

Figure 2.2: (Color online) Spin patterns of four phases: (a) E-AFM; (b) $C_{1/3}E_{2/3}$; (c) $SOS_{1/3}$; (d) Triangle-AFM. Two types of coordinate axes ($x-y$ for the pseudo-cubic notation and $a-b$ for the orthorhombic *Pbnm* notation) are shown in (a).

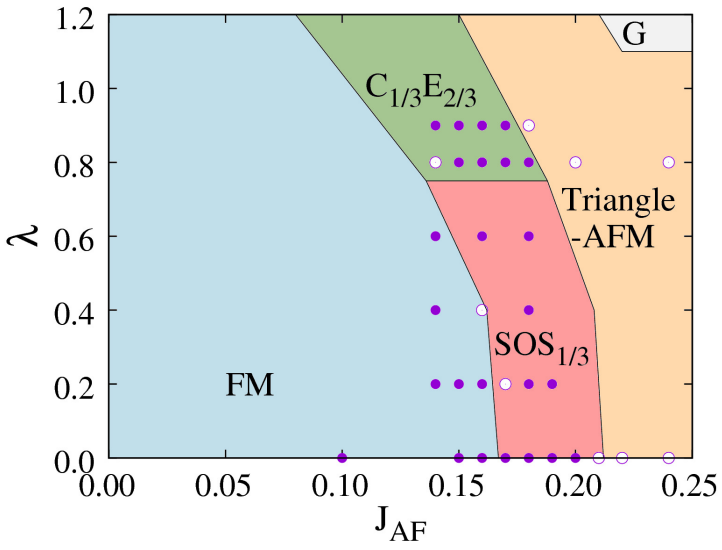

Figure 2.3: (Color online) (a) Ground state phase diagram at doping $x = 1/3$. The phase boundaries are obtained via the variational method plus the zero-T lattice optimization. The full dots denote MC simulation results which confirm the optimization calculation. Open dots are cases where the MC simulation does not provide a clear spin structure factor, which usually occur near phase boundaries where MC convergence is difficult due to the phase separation tendency. MC calculations were done at $T = 0.002$.

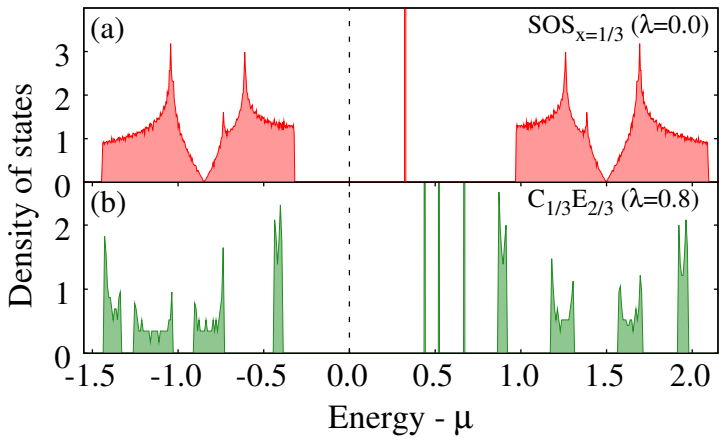

Figure 2.4: (Color online) The DOSs of e_g electrons: (a) $SOS_{1/3}$ phase (at $\lambda = 0$); (b) $C_{1/3}E_{2/3}$ phase (at $\lambda = 0.8$, obtained after the zero-T optimization of lattice distortion).

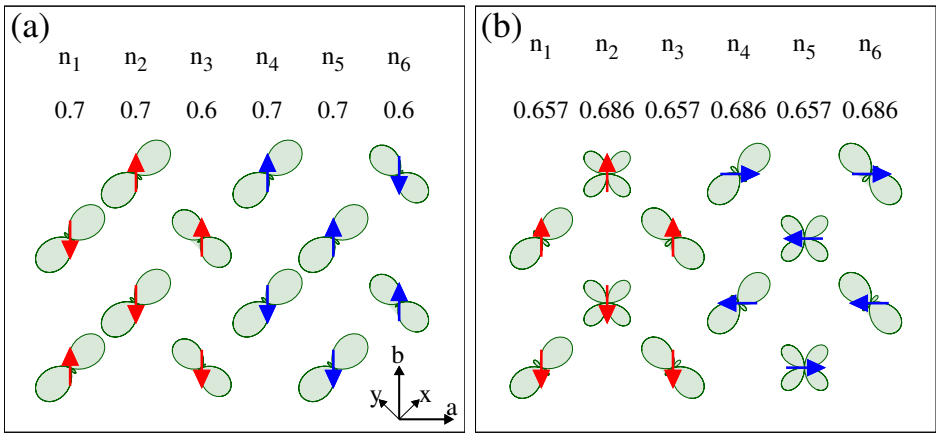

Figure 2.5: (Color online) Zero-T charge and orbital ordering of the $C_{1/3}E_{2/3}$ ($\lambda = 0.8$) and $SOS_{1/3}$ ($\lambda = 0$) phases, obtained via the lattice optimization calculation. The e_g density of each line (along $\vec{a}$-axis) is shown, which also depends on λ.

the boundary, in agreement with the $SOS_{1/4}$ case. For the $C_{1/3}E_{2/3}$ phase, charge and orbital orders also show stripe-type modulation. With large λ (> 1.0), charge accumulates on the stripes domain wall and leaves holes along the $\vec{b}$-axis in the stripe center.

2.3.2 Derivative $SOS_{1/3}$ and $C_{1/3}E_{2/3}$ series

In Ref. Dong et al. (2009), the basis $SOS_{1/4}$ and $C_{1/4}E_{3/4}$ phases share the same spin structure factor, which implies a close relationship between these two phases. Namely, the $C_{1/4}E_{3/4}$ pattern can be extracted from the $SOS_{1/4}$ spin vectors' x and y components. Further, here a simpler rule is proposed to reveal the implicit correlations between SOS_x/C_xE_{1-x} and E-AFM, and can be straightforwardly applied to other doping x and obtain the derivative SOS_x and C_xE_{1-x} series.

The C_xE_{1-x} and SOS_x phases can be viewed as *stripe-type domains* of the E-AFM state. First, the domain walls are along $\vec{b}$-axis and the width (along x- and y-axes) of each E-AFM stripe in SOS_x and C_xE_{1-x} is $N = 1/x$ (the inverse of the hole doping density). Consider $x = 1/3$ doping as an example, as indicated in Fig. 2.2, the E-AFM, $C_{1/3}E_{2/3}$, $SOS_{1/3}$ phases can be divided into "blue" (light) and "red" (dark) stripes. For the $C_{1/3}E_{2/3}$ case, there is a total shift along y axis (see axes labels in

Fig. 2.2) in the "blue" (light) domains, comparing with the original E-AFM. If an additional 90° rotation is applied to the "blue" (light) stripe of $C_{1/3}E_{2/3}$, the $SOS_{1/3}$ is obtained. This stripe domains of zigzag chains (width $1/x$ along x- and y-axes) can open an energy gap just at the Fermi levels due to the *topological* mechanism,Hotta et al. (2003); Hotta (2006) which can lower the energy to stabilize these states.

If the $SOS_{1/3}$ and $C_{1/3}E_{2/3}$ can be considered as special domain states of E-AFM, one important question is raised: is the $SOS_{1/3}$ or $C_{1/3}E_{2/3}$ unique? In other words, are there any other stripe domain structures fulfilling the aforementioned rules. The answer is positive if the basic period can be enlarged. The configurations shown in Fig. 2.2 are restricted in the minimum unit (6×6) of square lattices. If the period is enlarged to 12 units along x- and y-axes, there are more possible configurations for the $SOS_{1/3}$ and $C_{1/3}E_{2/3}$, which are called $SOS_{1/3}$-A, $SOS_{1/3}$-A and $C_{1/3}E_{2/3}$-B, $C_{1/3}E_{2/3}$-B as shown in Fig. 2.6.

The previous ones found in Sec. 2.3.1 are quoted as $SOS_{1/3}$-C and $C_{1/3}E_{2/3}$-C, because they are not the primary ones at $x = 1/3$. Their periods along a-axis are both 12, as shown in Fig. 2.2(b, c). In contrast, the $SOS_{1/3}$-A and $C_{1/3}E_{2/3}$-A in Fig. 2.6(a, b) show the minimum periods along a-axis are both 6. From the viewpoint of E-AFM stripe-type domains, the period along a-axis is more fundamental, which is also confirmed from the spin structure factors. As shown in Fig. 2.7(a), the $SOS_{1/3}$-A and $C_{1/3}E_{2/3}$-A phases share the common spin structure factor, with the strongest peak at $(\pi/2, \pi/2)$ and its equivalent position contributed by the E-AFM's period and satellite peaks contributed by the domain's period. This character of the spin structure factor was also found in Ref. Dong et al. (2009) for the $SOS_{1/4}$ and $C_{1/4}E_{3/4}$. In contrast, the $C_{1/3}E_{2/3}$-C and $SOS_{1/3}$-C found in Sec. 2.3.1 show different (lower symmetric) spin structure factors, as shown in Fig. 2.7(b) and (c), respectively. Therefore, although all these derivative series are constructed from E-AFM stripes and with the same stripe width, their spin structure factors depend on the way how these stripes are organized, which can either have the $(\pi/2,\pi/2)$ peak missing or present an asymmetric S_q peaks distribution. The effect of derivative series to spin structure factors will be discussed

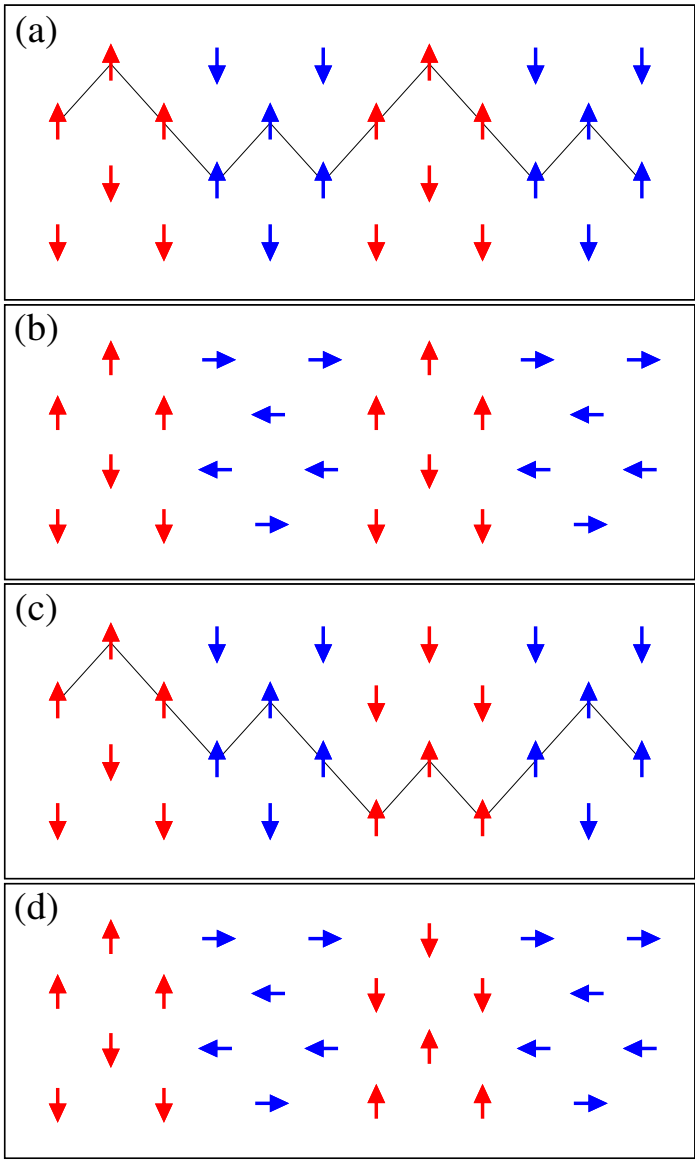

Figure 2.6: (Color online) Spin patterns: (a) $C_{1/3}E_{2/3}$-A; (b) $SOS_{1/3}$-A; (c) $C_{1/3}E_{2/3}$-B; (d) $SOS_{1/3}$-B. Comparing with the original $C_{1/3}E_{2/3}$-C and $SOS_{1/3}$-C ones (shown in Fig. 2.2), the first and second stripes stay the same(from left to right). All spins in the third and forth stripes of (a) and (b), the third stripe of (c) and (d) are reversed.

in more detail later. In short, the $SOS_{1/3}$ and $C_{1/3}E_{2/3}$ phases found in Sec. 2.3.1 are not the primary ones but derivative ones, although they require the minimum square lattice.

Since the primary ones and all derivative one satisfy the construction rules mentioned above but with an opposite sign between NNN stripes. They can also open gaps at the Fermi levels to reduce the energies. Therefore, it is necessary to compare the energies of these $SOS_{1/3}$ and $C_{1/3}E_{2/3}$ series to determine whether these derivative phases affect the phase diagram. As shown in Fig. 2.8, the $SOS_{1/3}$ and $C_{1/3}E_{2/3}$ series are competing with each other to be the ground state under different lattice distortions. The $SOS_{1/3}$ series listed above are degenerate independent of λ, which dominate the region $\lambda < 0.7$. At range $0.7 < \lambda < 1.04$, the $C_{1/3}E_{2/3}$-C state is the ground state. In the range $\lambda > 1.6$, all six states converge to the same energy. The degeneracy suggests that it may be difficult to detect a $SOS_{1/3}$ pure phase in real experiments with low-bandwidth hole-doped manganites, but instead the coexistence of a set of degenerate $SOS_{1/3}$ states is a more likely outcome.

The idea of E-AFM domain strips reminds us that the ES effect may also work in the SOS_x and C_xE_{1-x} phase. A careful check finds that the $SOS_{1/4}$-A presented in Ref. Dong et al. (2009) does own a FE polarization due to the ES effect, although this polarization was neglected in Ref. Dong et al. (2009). This FE component may be much larger than the DM one, which makes the $SOS_{1/4}$ phase more attracting. However, the local FE polarizations caused by the ES effect cancel each other between domains in the $SOS_{1/3}$-A and $C_{1/3}E_{2/3}$-A presented here due to the odd number $1/x$. Even though, there is a DM driven FE polarization in the $SOS_{1/3}$-A phase, as shown in Fig. 2.9. It should be noted that the FE polarization may be totally difficult between the primary $SOS_{1/3}$ and derivative ones. More discussion on multiferroicity will be given later.

Due to the degeneracy, the MC simulation of $SOS_{1/3}$ phases should be more careful. In order to study the T_C of DM-ferroelectricity, the initial states were set to $SOS_{1/3}$-A and $SOS_{1/3}$-C. In the square lattice, the minimum size for $SOS_{1/3}$-A is

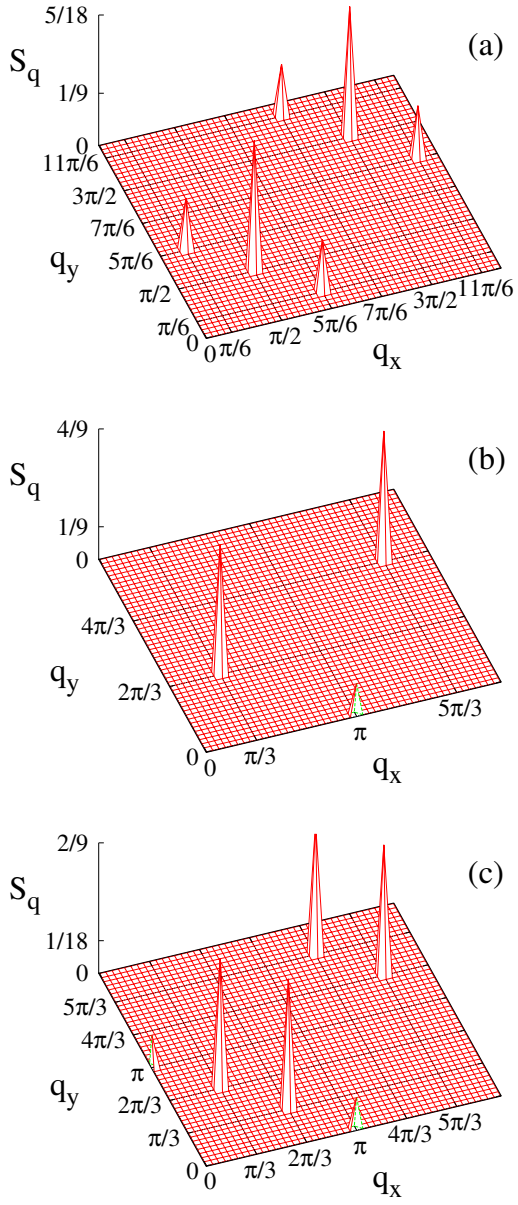

Figure 2.7: (Color online) The spin structure factors: (a) $SOS_{1/3}$-A and $C_{1/3}E_{2/3}$-A phases. The main peaks appear at wavevector $2\pi(1/4,1/4)$ and $2\pi(3/4,3/4)$, with an amplitude 5/18, while the weaker peaks appear at $2\pi(1/12,5/12)$, $2\pi(5/12,1/12)$, $2\pi(11/12,7/12)$, and $2\pi(7/12,11/12)$, with an amplitude 1/9. (b) $C_{1/3}E_{2/3}$-C phase. The main peaks appear at wavevector $2\pi(1/6,1/3)$ and $2\pi(5/6,2/3)$, with an amplitude 4/9, while the weaker peak appear at $2\pi(1/2,0)$, with an amplitude 1/9. (c) $SOS_{1/3}$-C phase. The main peaks appear at wavevector $2\pi(1/6,1/3)$, $2\pi(1/3,1/6)$, $2\pi(5/6,2/3)$ and $2\pi(2/3,5/6)$, with an amplitude 2/9, while the weaker peaks appear at $2\pi(1/2,0)$ and $2\pi(0,1/2)$, with an amplitude 1/18.

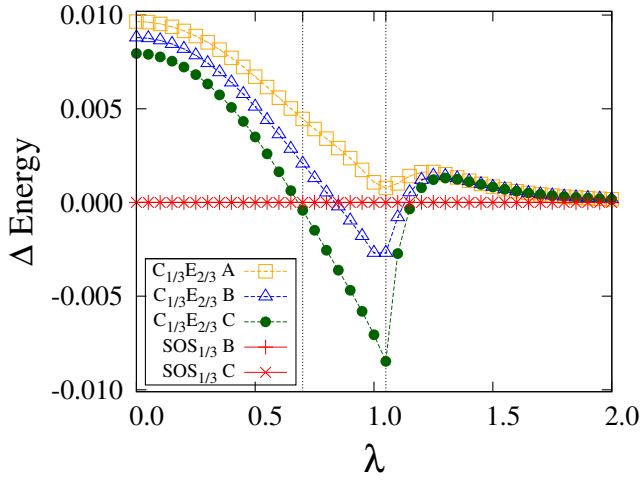

Figure 2.8: (Color online) Energy deviation from the $SOS_{1/3}$-A for $SOS_{1/3}$-BC (Red line) and $C_{1/3}E_{2/3}$ states including the lattice optimization procedure, employing a small cluster of size $2\sqrt{2} \times 6\sqrt{2}$ for the actual calculation. Three degenerate $SOS_{1/3}$ -A, -B, -C states have exactly the same energy at large values of the electron-phonon coupling. And they are the ground states with $\lambda < 0.7$. For λ values between 0.7 and 1.4, the $C_{1/3}E_{2/3}$-A state becomes the ground state.

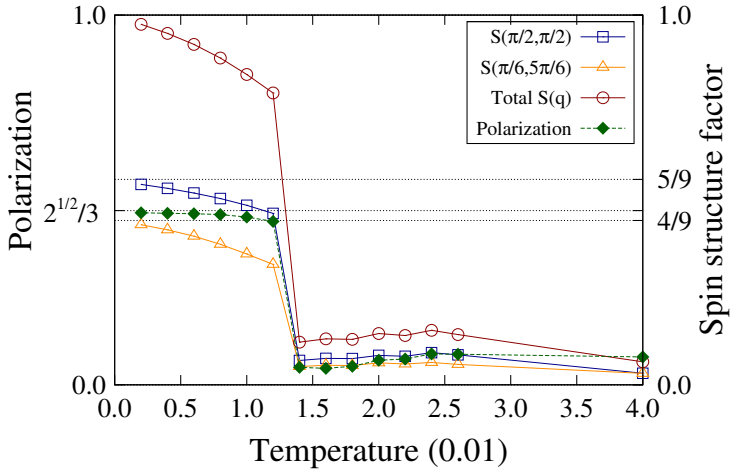

Figure 2.9: (Color online) Finite temperature MC results (at $J_{\rm AF} = 0.175$ and $\lambda = 0$) for the $SOS_{1/3}$-A phase, on the 12×12 cluster. Each point is obtained by MC heating up the simulation starting with the ideal $SOS_{1/3}$ spin configuration. *Left axis*: FE polarization $|\vec{P}|$ per site, calculated using $\sum_{<i,j>}[\vec{e}_{i,j} \times (\vec{S}_i \times \vec{S}_j)]/L^2$. *Right axis*: amplitudes of the characteristic peaks in the spin structure factors. A 6×6 cluster calculation on $SOS_{1/3}$-C gives the transition temperature equal to 0.014 ($\sim$ 40 K).

$L = 12$, while for $SOS_{1/3}$-C is $L = 6$. And the calculations for both phases shows exactly the same first-order transition at $T = 0.014$ ($\sim 30 - 80$ K). Interestingly, the $SOS_{1/3}$-A phase has a net DM-FE polarization (equal to $\sqrt{2}/3$ per site at zero-T) but the $SOS_{1/3}$-B and $SOS_{1/3}$-C do not have a net DM-FE polarization. In Fig. 2.7, the T-dependence curves of the spin structure factors and the DM-polarization (for $SOS_{1/3}$-A only) are shown. With decreasing T, these observables approach the zero-T theoretical limits shown in dashed lines.

Luckily enough, the charge and orbital orders of the $SOS_{1/3}$ and $C_{1/3}E_{2/3}$ series are not altered by the high degeneracy. In other words, the spin flips of E-AFM domains can switch the phases between the $SOS_{1/3}$-A and $SOS_{1/3}$-B (or $SOS_{1/3}$-C .....) without changes of other physical properties but only the FE polarization.

2.3.3 SOS_x phases at $x = 1/2, 1/5, 1/6, ...$

After the discussion focusing on the $x = 1/3$ doping, let us now move to more general cases involving hole densities $x = 1/N$ (with $N = 2, 4, 5, 6, ...$). By using the E-AFM stripe construction procedure outlined before, we can construct SOS_x and C_xE_{1-x} phases with stripe-width equal to N (along x and y axes).

The $N = 4$ case was already studied in our previous publication.Dong et al. (2009) The $C_{1/2}E_{1/2}$ (mostly quoted as CE) phase has been known for more than 50 years,Wollan and Koehler (1955) as shown in Fig. 2.10(a). In fact, the case of $SOS_{1/2}$ has already been found by others which is multiferroic and now turns out to be one special case of the SOS_x family. The $SOS_{1/2}$ follows the same construction rule as for the $x = 1/3$ doping, but with stripe-width equal to two, as shown in Fig. 2.10(b). The charge and orbital orderings of $C_{1/2}E_{1/2}$ and $SOS_{1/2}$ are also shown in Fig. 2.10(a) and (b), respectively.

Regarding $N = 5$ and $N = 6$, their spin/charge/orbital configurations still follow the same rules of the $x = 1/3$ case, as shown in Fig. 2.10(c-f). Electrons accumulate in the center of the SOS_x stripes while holes accumulate in the center of C_xE_{1-x}

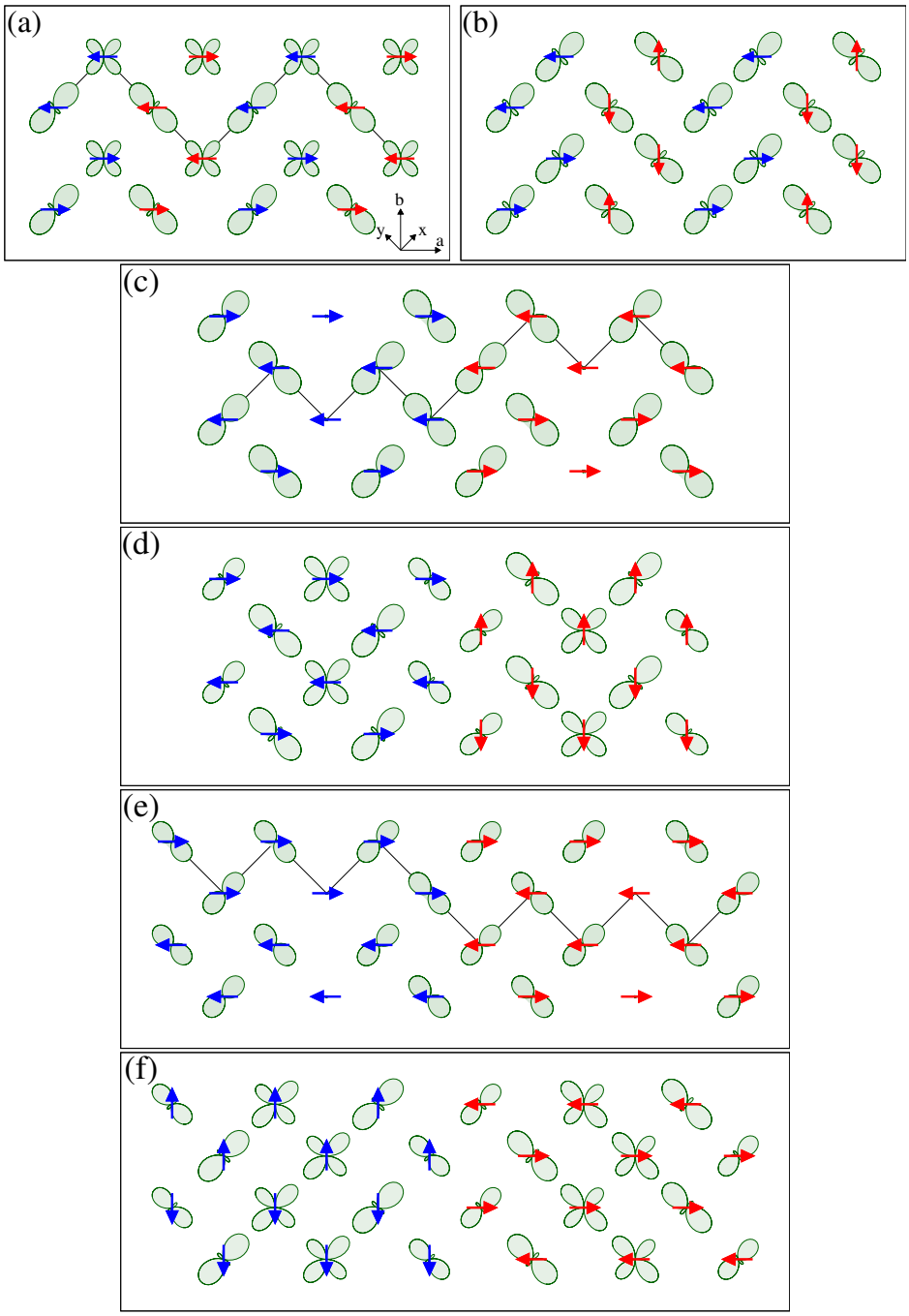

Figure 2.10: (Color online) The charge and orbital orders of the $x = 1/2$, $1/5$, $1/6$ SOS_x and C_xE_{1-x} phases, obtained using variational and lattice optimization calculation. Both the CE and $SOS_{1/2}$ phases are calculated with zero electron-phonon coupling. At large coupling $\lambda = 1.8$, the $C_{1/5}E_{4/5}$ and $C_{1/6}E_{5/6}$ phases form lines of zero e_g density sites along the $\vec{a}$ direction in the middle of each E-AFM stripe. At $\lambda = 0$, the $SOS_{1/5}$ and $SOS_{1/6}$ phases show high electronic densities at the center of the stripes and low densities on the stripe domain walls.

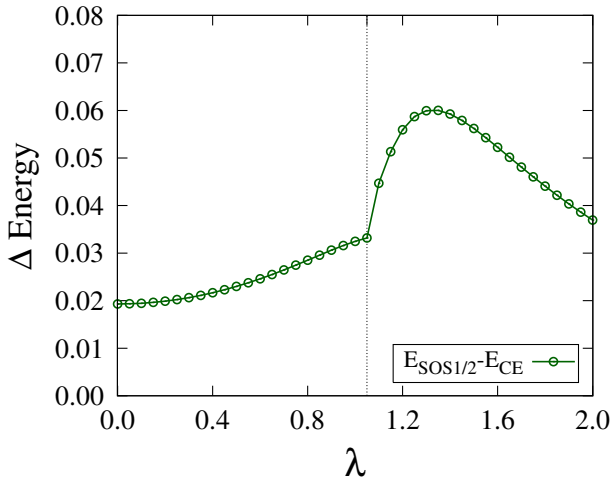

Figure 2.11: Energy deviation from the $C_{1/2}E_{1/2}$ (CE) for $SOS_{1/2}$ state including the lattice distortion optimization. Note that here the $SOS_{1/2}$ phase always has a higher energy. Therefore, in Ref. Giovannetti et al. (2009), an additional Coulomb U is required to stabilize the $SOS_{1/2}$ state.

zigzags. By considering more N's, this uniform picture shows a gradual change from the CE/$SOS_{1/2}$ case at half-doped manganites ($N = 2$) to the E-AFM phase at undoped manganites ($N = \infty$).

However, it should be pointed out that the $SOS_{1/2}$ state has a higher energy (more than 0.01 eV) than the $C_{1/2}E_{1/2}$ phase in the whole λ region, as shown in Fig. 2.11, which is different from $x = 1/3$ and $x = 1/4$ cases. The reason is that the $N = 2$ stripe is too narrow to accommodate a full zig-zag period to reduce the system's energy. This stable $C_{1/2}E_{1/2}$ is in agreement with experimental observations that the CE phase is very robust at $x = 1/2$. In Ref. Giovannetti et al. (2009), an additional Coulomb U is necessary to stabilize the $SOS_{1/2}$ state.

While for other N's, as shown explicitly by both MC and variational calculations, these states share similar properties in the ground state phase diagrams, as shown in Fig. 2.12(a) and Fig. 2.13(a). The SOS_x phases are energetically stable in the small bandwidth (large J_{AF}) area for all other dopings, except the $x = 1/2$ case. The DOSs show that both the $SOS_{1/5}$, $C_{1/5}E_{1/5}$, $SOS_{1/5}$, and $SOS_{1/6}$ phases are insulators, as shown in Fig. 2.12(b,c) and Fig. 2.13(b,c).

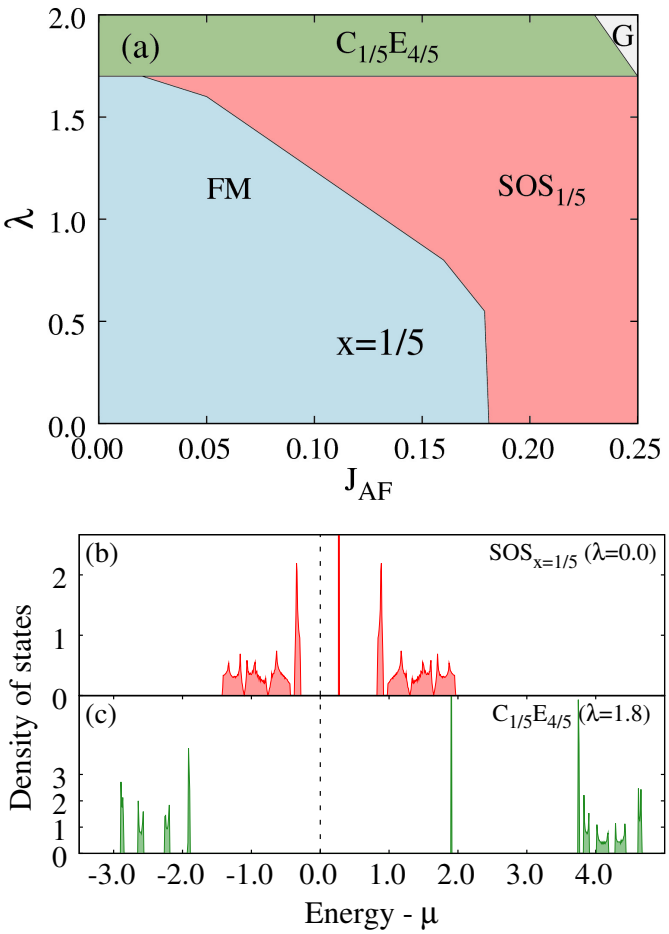

Figure 2.12: (Color online) (a) Ground state phase diagram obtained via the zero-T variational calculation with lattice optimization, at hole doping $x = 1/5$. (b) DOSs of the $SOS_{1/5}$ ($\lambda = 0.0$) and $C_{1/5}E_{4/5}$ ($\lambda = 1.8$) phases. All these phases have a gap at the Fermi level. For the $SOS_{1/5}$ case ($\lambda = 0.0$), the gap is about 0.2 (~ 0.1 eV), while for $C_{1/5}E_{4/5}$ ($\lambda = 1.8$) the gap is 2.0 (~ 1.0 eV).

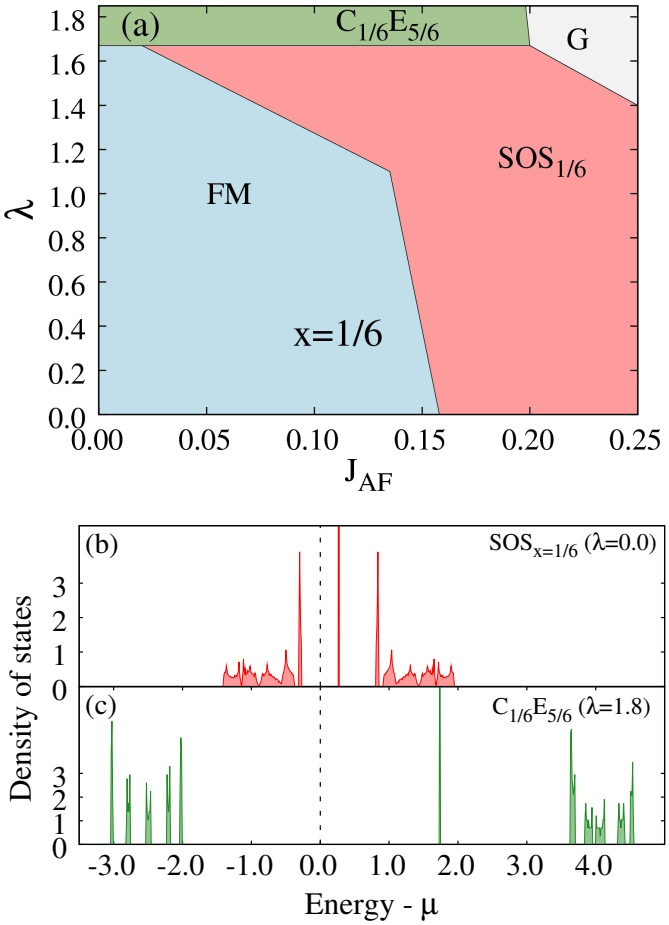

Figure 2.13: (Color online) (a) Ground state phase diagram obtained via the variational calculation with lattice optimization at hole doping $x = 1/6$. (b) DOSs of the $SOS_{1/6}$ ($\lambda = 0.0$) and $C_{1/6}E_{5/6}$ ($\lambda = 1.8$) phases. All these phases have a gap at the Fermi level. For the case of SOS, the gap is about 0.2 (~ 0.1 eV) ($\lambda = 0.0$), while for $C_{1/6}E_{5/6}$ ($\lambda = 1.8$) the gap is 2.0 (~ 1.0 eV).

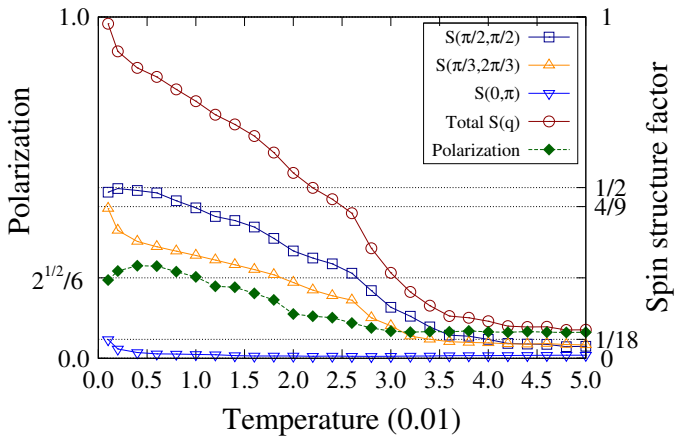

Figure 2.14: (Color online) Finite-T MC results (at $J_{\rm AF} = 0.175$, $\lambda = 0.0$) for the $\rm SOS_{1/6}$ phase on the $L = 12$ cluster. Each point is obtained by a MC heating up calculation starting with the ideal $\rm SOS_{1/6}$ spin configuration. The ferroelectric polarization approaches the $\sqrt{2}/6$ limit at low temperatures. This temperature dependent curve shows that the $\rm SOS_{1/6}$ phase has a transition temperature of 0.034 ($\sim$ 190 K).

The MC calculation has also been done to determine the $T_{\rm C}$ of $\rm SOS_{1/6}$ phase. In Fig. 2.14, all peaks of spin structure factor and the FE polarization are measured, which show a $T_{\rm C}$ of approximately $0.034t_0$ ($\sim 80 - 190$ K).

At last, it should be noted that all spin patterns shown in this subsection are the primary ones ($\rm SOS_{\it x}$-A and $\rm C_{\it x}E_{1-\it x}$-A), which's periods are minimum along the $\vec{a}$-axes.

2.3.4 Macroscopic degeneracy and dimensional reduction

Similarly to the $x = 1/3$ case, more derivative $\rm SOS_{\it x}$ and $\rm C_{\it x}E_{1-\it x}$ patterns can be obtained for other x by reversing or shifting some stripes in these E-AFM domain structures with enlarged periods. At each doping x, $\rm C_{\it x}E_{1-\it x}$ series show very close energies, while the energies of $\rm SOS_{\it x}$ series are totally degenerate.

The degeneracy of $\rm SOS_{\it x}$ phases can be explained as the isolation of stripes by the 90 degree spin arrangement across the domain walls, which contributes zero DE-

Table 2.1: The multiferroelectricity of SOS_x and C_xE_{1-x}. Here only the primary states have been considered. The origins of FE polarization vary with the dopings and spin orders.

$N = 1/x$	Odd	Even
SOS_x	DM	DM+ES
C_xE_{1-x}	ES	none

and SE-energy change during the derivation procedure. Also, the charge- and orbital-orderings are not affected by the reversing of all spins in neighbor stripes.

As mentioned above, there are two FE polarization mechanisms in the SOS_x phases. One is the inverse DM interaction which creates a local FE polarization on the domain wall between stripes. The other is the ES effect proposed for the E-AFM phase. The net FE polarization varies with the different degenerate states and dopings. For the inverse DM mechanism, the SOS_x-A phases always have the strongest DM-polarization comparing with other derivative phases. In the SOS_x family, the FE polarization driven by the ES effect is finite only with even N, which's intensity is in inverse proportional to x. While for the C_xE_{1-x}-A phase, the DM driven FE polarization is always zero due to the collinear spin pairs but the ES can induce FE polarizations when N is odd, as summarized in Table. 3.1.

In order to study the coexistence of degenerate sates and their influence on real experiments, two opposite spin orientations for each stripes in the C_xE_{1-x} and SOS_x cases are taken into consideration. Because the periodicity along the direction $\vec{b}$ is $2\sqrt{2}$, this type of degenerate SOS phases creates a broad spin structure factor $S(\vec{q})$ going from (0, π) to (π, 0), which is $\frac{2\pi}{2\sqrt{2}}$ away from the (0, 0) point and zero excitations in all other points in momentum space. Due to their periodicity, the dimensional reduction technique can be used to simplify the E-AFM, C_xE_{1-x}, SOS_x 2D phases into two 1D chains along the $\vec{a}$ axis.

For instance, at $x = 1/5$ doping, the two basic chains for $SOS_{1/5}$ are ($\uparrow\uparrow\leftarrow\leftarrow\leftarrow$) and ($\uparrow\uparrow\uparrow\rightarrow\rightarrow$) with each length equal to $5\sqrt{2}$. For a $40\sqrt{2} \times \sqrt{2}$ lattice with four stripes which were separated into two chains, there are $2^4 = 16$ degenerate

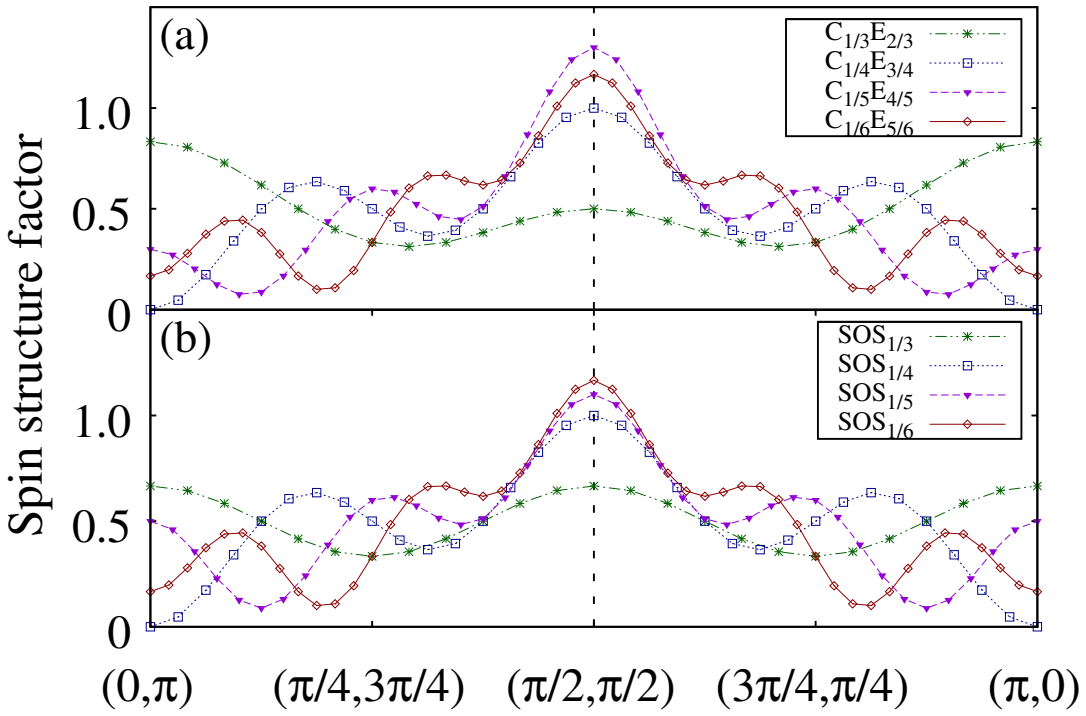

Figure 2.15: (Color online) The average spin structure factor of the C_xE_{1-x} (top picture) and SOS_x (bottom picture) degenerate states. Including the degenerate states with two opposite spin arrangements of each E-AFM stripe in $8N\sqrt{2} \times \sqrt{2}$ ($x = 1/N$) cluster, The average spin structure factor of 2^{16} degenerate SOS_x states present broad peaks along the (π, 0) and (0, π) direction. Neglecting that the lattice distortion may break the degeneracy of C_xE_{1-x}, the average spin structure factor of C_xE_{1-x} shows quite similar spin structure factor as the SOS_x states.

configurations for both the $C_{1/5}E_{4/5}$ and $SOS_{1/5}$ states. The spin flipping of each SOS stripe will keep the energy of the system the same. Even taking lattice distortions into consideration, the spin flip of one SOS stripe will not change the orbital- or charge-orderings, as discussed before.

Because these derivative states have the same energy (or nearly degenerate in C_xE_{1-x} states), the averaged spin structure factors along (0, π) to (π, 0) for each doping $x = 1/3$, $1/4$, $1/5$ and $1/6$ are calculated, as shown in Fig. 2.15. This dimensional reduction calculation shows that each set of SOS_x and C_xE_{1-x} with the same doping x share the very similar average spin structure factor. The inverse DM mechanism of the SOS phases may also be suppressed by degenerate SOS phases which have weaker DM-induced polarization. However, these degenerate SOS phases are quite interesting because their *macroscopic degeneracy* is 2^m, where m is the number of stripes which is in proportional to the $\sqrt{N}$ (N is the square area). Thus the zero-T entropy of SOS_x remains zero. This macroscopic degeneracy of SOS_x is different from the neither normal ordered systems (without macroscopic degeneracy) nor spin ice systems (with macroscopic degeneracy and nonzero zero-T entropies).

2.4 Summary

By using the microscopic model Hamiltonian, the phase diagrams of hole-doped manganites have been systematically studied. Most efforts have been devoted to the SOS_x and C_xE_{1-x} phases, which appear in the narrow-bandwidth limit. The SOS_x and C_xE_{1-x} families have been found to exist in the whole hole doping range from $x = 1/2$ to $x = 0$, which may be multiferroic at certain values of x. In addition, the macroscopic degeneracy in the SOS_x and C_xE_{1-x} families have been revealed, which is different from normal ordered materials or spin ice systems.

Chapter 3

Monte Carlo study of a 3D Heisenberg Model to reproduce recent experimental results in $BiFeO_3$

3.1 Organization

We will start with the isotropic three-dimensional Heisenberg model to show that our Monte Carlo calculations on the lattices that we can handle provide accurate information for the critical temperature, when compared with published literature. Then, we move to the more subtle issue of the two-dimensional Heisenberg model and its notorious size effects. Finally, we focus on the parameter regime that is relevant for the R- and T-phases found experimentally, as explained later, and formulate our conclusions MacDougall et al. (2012).

3.2 The Heisenberg Model with an isotropic exchange coupling J as a test

The three dimensional (3D) isotropic Heisenberg model with couplings $J_x = J_y = J_z = J = 1.0$ is defined as:

$$H = \sum_{\langle ij \rangle} J\vec{S}_i \cdot \vec{S}_j.$$

In the Monte Carlo (MC) calculation, we typically perform 4000 steps for thermalization and between 1000 and 4000 steps for measurements at each temperature, but results with more steps are also provided in other sections below. In order to study the transition from a G-AFM antiferromagnetic state into a magnetically disordered state with increasing temperature both the spin structure factor at the relevant wavevector for G-AFM order i.e. $S(\pi, \pi, \pi)$ and the AF-magnetization $\langle M \rangle$ are measured. Here, the AF-magnetization $\langle M \rangle$ is given by $|\langle M_A \rangle - \langle M_B \rangle|$ where $\langle M_A \rangle$ and $\langle M_B \rangle$ are the magnetization of the two sublattices. Using a $10 \times 10 \times 10$ lattice with periodic boundary conditions to reduce the size effects, the MC calculation gives a Néel critical temperature $\mathrm{T}_N \sim 1.6$ (Fig. 3.1).

3.2.1 Comparison with mean-field calculations

Only for completeness, and to check the effect of fluctuations that are not incorporated in mean-field studies, here the mean-field calculation has also been applied to predict the critical temperature.

$$\begin{aligned} H &= \sum_{\langle ij \rangle} J\vec{S}_i \cdot \vec{S}_j \\ &= \frac{1}{2}\sum_{ij} J(\vec{S}_i - \langle S \rangle) \cdot (\vec{S}_j - \langle S \rangle) + z\sum_i J\vec{S}_i\langle S \rangle - \frac{z}{2}\sum_i J\langle S \rangle^2 \end{aligned} \tag{3.1}$$

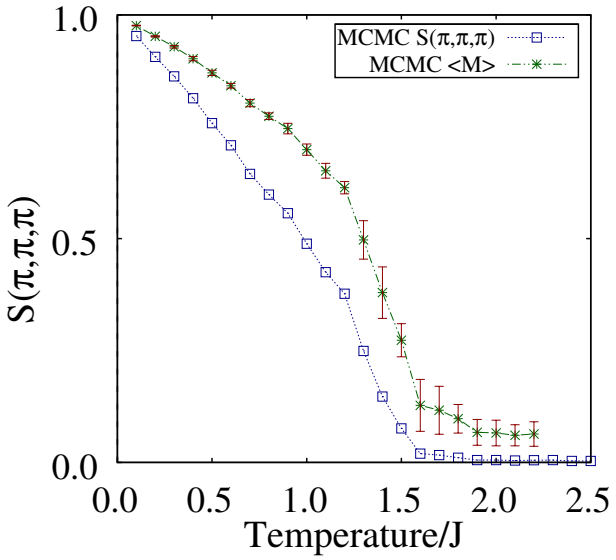

Figure 3.1: The MC results for the spin structure factor $S(\pi, \pi, \pi)$ and the AF-magnetization $\langle M \rangle$, for the case of the 3D isotropic Heisenberg model with all couplings equal to 1. Both curves indicate a Néel critical temperature $T_N \sim 1.6$.

Here, z is the number of neighbors of a given site which is 6 in our 3D model defined on a cubic lattice. By subtracting the second order term $\frac{1}{2}\sum_{ij} J(\vec{S}_i - \langle S \rangle) \cdot (\vec{S}_j - \langle S \rangle)$ we get the mean-field-approximation Hamiltonian:

$$H \approx z \sum_i J \vec{S}_i \langle S \rangle - \frac{z}{2} J \cdot N \langle S \rangle^2.$$

This mean field method is well known for Quantum Heisenberg model and gives a critical temperature $T_N = \frac{z}{4}$ for spin 1/2 variables. In the classical Heisenberg model case, the average magnetization M is

$$\langle M \rangle = \frac{\int_{-1}^{1} \langle S \rangle e^{-6\beta \langle S \rangle} d\langle S \rangle}{\int_{-1}^{1} e^{-6\beta \langle S \rangle} d\langle S \rangle} = cotanh(6\beta \langle S \rangle) - \frac{1}{6\beta \langle S \rangle}.$$

This mean field calculation gives a critical temperature $T_N = 2.0$ which, as expected, is higher than the MC results (Fig. 3.2), since the mean-field approximation enhances the tendencies to form order states since they do not include properly the fluctuations.

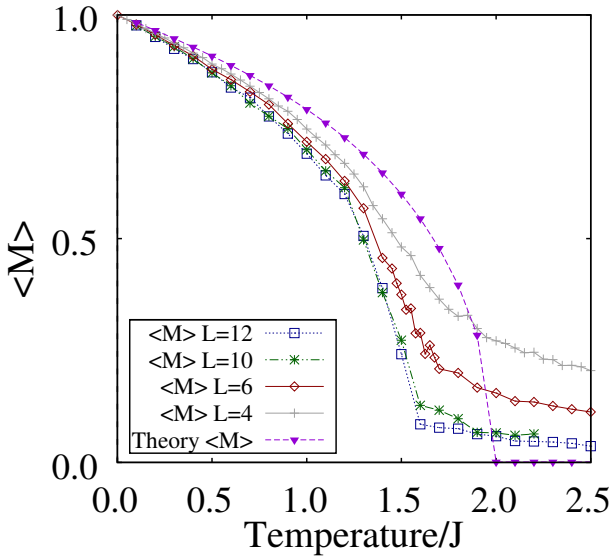

Figure 3.2: The comparison between the MC results and the mean-field calculation predictions, for the 3D isotropic Heisenberg model. The T_N of the mean-field calculation is 2.0 (no fluctuations included here), while the more accurate T_N of the MC calculation is approximately 1.55.

By comparing several MC results using different lattice sizes, an extrapolation of the MC T_N's should be close to 1.55.

3.2.2 $T_N(\chi_M)$ from magnetic susceptibility(χ_M) measurements

Besides measuring and estimating the T_N from the magnetization curves, the magnetic susceptibility is another observable that can be used to describe phase transitions, and it is defined as:

$$\langle \chi \rangle = N\beta \langle M - \langle M \rangle \rangle^2,$$

(note: M represents $|\vec{M}|$. $\vec{M}$ is the staggered magnetization of each layer.) As shown in Fig. 3.3, the peak of χ_M is caused by the large fluctuations in the magnetization during the phase transition. As a result, the T_N measured from the magnetization curve is just a little higher than that from the χ_M. We have studied the $T_N(\chi_M)$

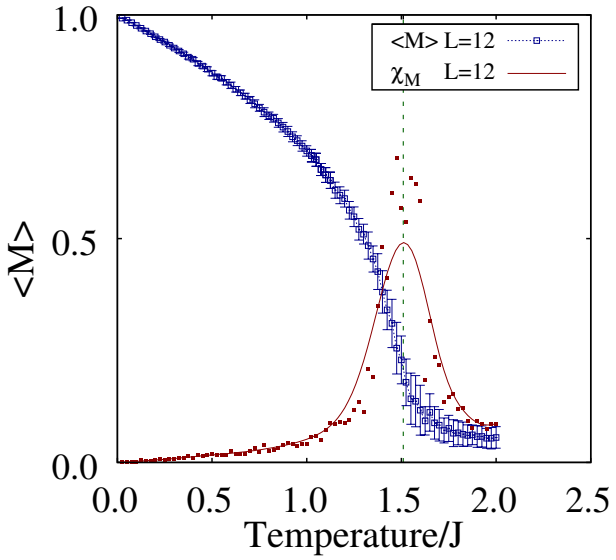

Figure 3.3: The magnetization curve and the magnetic susceptibility (χ_M) curve using a $12 \times 12 \times 12$ lattice, and the 3D isotropic Heisenberg model. The T_N that can be estimated from $\langle M \rangle$ is just slightly higher than the T_N that arises from χ_M, for the case of the isotropic 3D Heisenberg model.

with different lattice sizes (Fig. 3.4). At L=12, the χ_M^{MAX} gives a $T_N(\chi_M) \sim 1.48$ which is in good agreement with MC results in previous literature Holm and Janke (1993)Chen et al. (1993).

3.3 Heisenberg Model with $J_z = 0$

Since the new experimental results MacDougall et al. (2012) suggest a small coupling along the z-axis, then it is important to gain some intuition on what to expect by studying the case of a two dimensional Heisenberg model (a special case of an anisotropic Heisenberg model). By setting $J_z = 0$ and $J_x = J_y = 1.0$, we can easily transform our 3D model into an equivalent 2D Heisenberg model. For a two-dimensional Heisenberg model, the Mermin-Wagner theorem Mermin and Wagner (1966) shows that there is no spontaneously magnetized phase at nonzero temperature. However, the correlation length for antiferromagnetism can be huge and for most practical purposes the 2D system behaves like a magnetic state on the

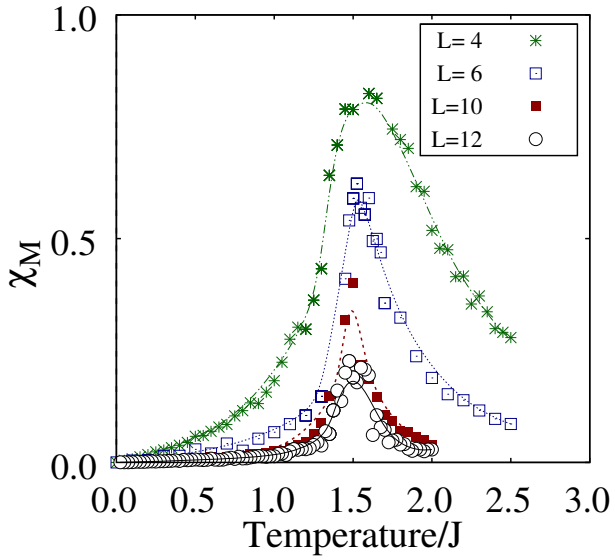

Figure 3.4: The comparison of $T_N(\chi_M)$ obtained with different lattice sizes, for the 3D isotropic Heisenberg model. The $T_N(\chi_M)$ tends to drop slightly below 1.5 in the thermodynamic limit.

finite lattices that can be studied numerically. In addition, in real systems small couplings in the third dimension profoundly affect the results rapidly leading to a finite temperature critical temperature. Thus, the case of the 2D Heisenberg model is very pathological.

Our MC results show that the transition in 2D ($J_z = 0$) (Fig. 3.5) is smoother than in the previously described 3D calculation (i.e. it is not so sharp). We computed using the 3D lattice but with zero coupling along the z-axis ($J_z = 0$, $J_x = J_y = 1.0$) for the cases L= 6, 8, and 10, but directly used a 2D lattice ($J_x = J_y = 1.0$) for the cases L= 20, 30, 40, and 80. According to our finite-size scaling (Fig. 3.6), that thus far uses only a very limited number of clusters, the $T_N(\chi_M)$ with increasing lattice sizes does not show a clear tendency to convergence to $T = 0$, i.e. the bulk extrapolation seems (incorrectly) to suggest a finite critical temperature as anticipated by the qualitative discussion above that remarked the huge values of the correlation lengths. Even with a 80×80 lattice calculation, the T_N appears to be still above 0.5. We also compared with MC results by our collaborator Shuai Dong (for the specific heat C_v)

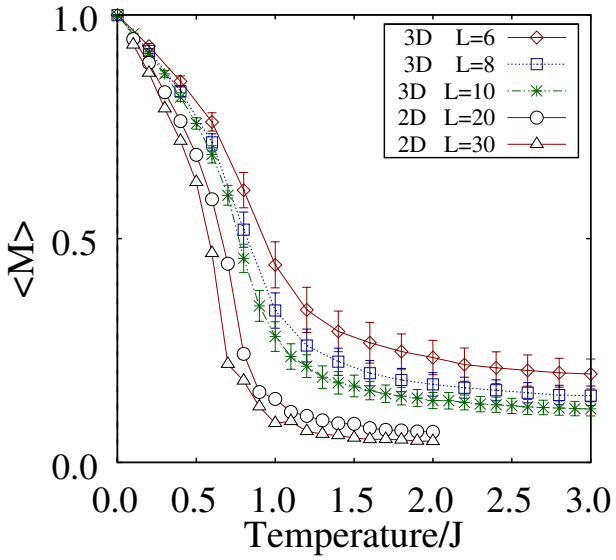

Figure 3.5: Magnetization vs. temperature with different lattice sizes, for the 2D isotropic Heisenberg model. The L= 6, 8, and 20 calculations are for 3D lattices with $J_x = J_y = 1.0$ and $J_z = 0.0$, while the L= 20 and 30 calculations used 2D lattices with $J_x = J_y = 1.0$.

and they are in good agreement (Fig. 3.7), suggesting that there is no "bug" in the codes. However, on a more positive note, at least we have observed a *clear* difference between 3D and 2D, with a critical temperature approximately ∼1.5 for 3D and ∼0.5 (or lower, according to Mermin-Wagner) for 2D.

3.4 3D-Heisenberg Model with anisotropic exchange couplings J: a preliminary test

Now let us consider the case of anisotropic couplings J_x, J_y, and J_z into our 3D model, in order to try to reproduce the experimental results on $BiFeO_3$ by Christen *et al.*. First, let us compare our MC calculations with the results of other groups Yasuda et al. (2005) on a quasi-two-dimensional system by setting $J_x = J_y = 1.0 > J_z$. We select two sets of parameters $J_z = 0.5$ and $J_z = 0.1$ and study a $10 \times 10 \times 10$ lattice. The Néel temperatures (Fig. 3.8) are approximately found to be 1.25 (for $J_z = 0.5$)

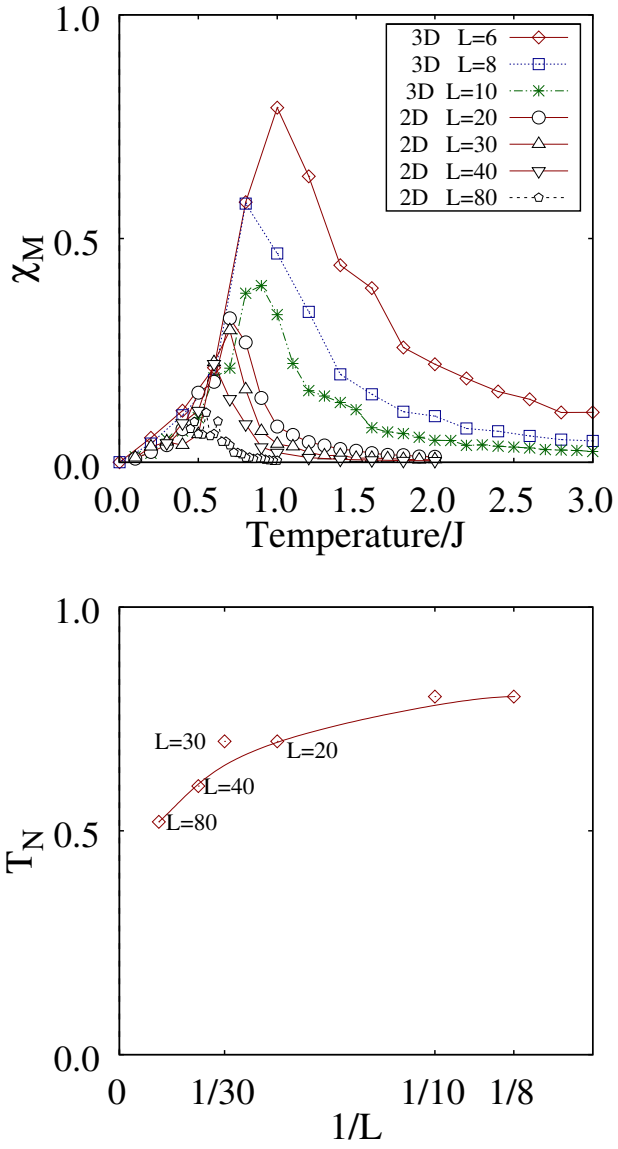

Figure 3.6: The convergence tendency of the critical temperatures $T_N(\chi_M)$ with different lattice sizes, for the case of the two-dimensional Heisenberg model (note that the 3D label just denotes that the simulation was done with a 3D cluster, but using $J_z = 0$). The critical temperature appears to extrapolate to a finite number, but note that the curvature of the fit suggests the possibility, anticipated by the Mermin-Wagner theorem, that the critical temperature will sharply drop and reach zero in the bulk.

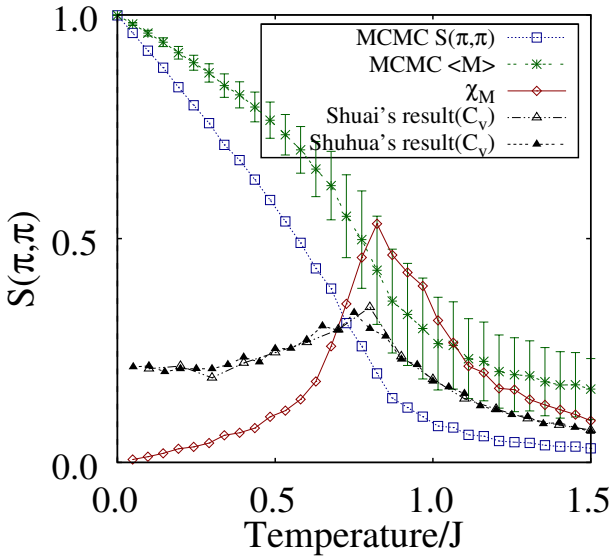

Figure 3.7: The temperature dependence curve of $S(\pi, \pi)$, M, χ_M, and specific heat C_v using a 2D L=10 lattice, and the isotropic Heisenberg model. The comparison of C_v with Shuai Dong's result is also shown.

Table 3.1: Comparison of Néel temperates between our simulations and those of Ref. Yasuda et al. (2005). ($J_x = J_y = 1$)

J_z/J_x	1.0	0.5	0.1
MC results ($L = 10$)	1.52	1.25	0.85
MC from Ref.Yasuda et al. (2005)	1.443	1.173	0.853

and 0.85 (for $J_z = 0.1$) which are in agreement with the MC results in publication Ref. Yasuda et al. (2005) where $T_N = 1.1733$ (for $J_z = 0.5$) and $T_N = 0.8526$ (for $J_z = 0.1$) were reported, as summarized in Table 3.1. Thus, these tests indicate that our method of calculation is fairly accurate, with the only exception of the difficulty in reaching a zero critical temperature for the strictly 2D case.

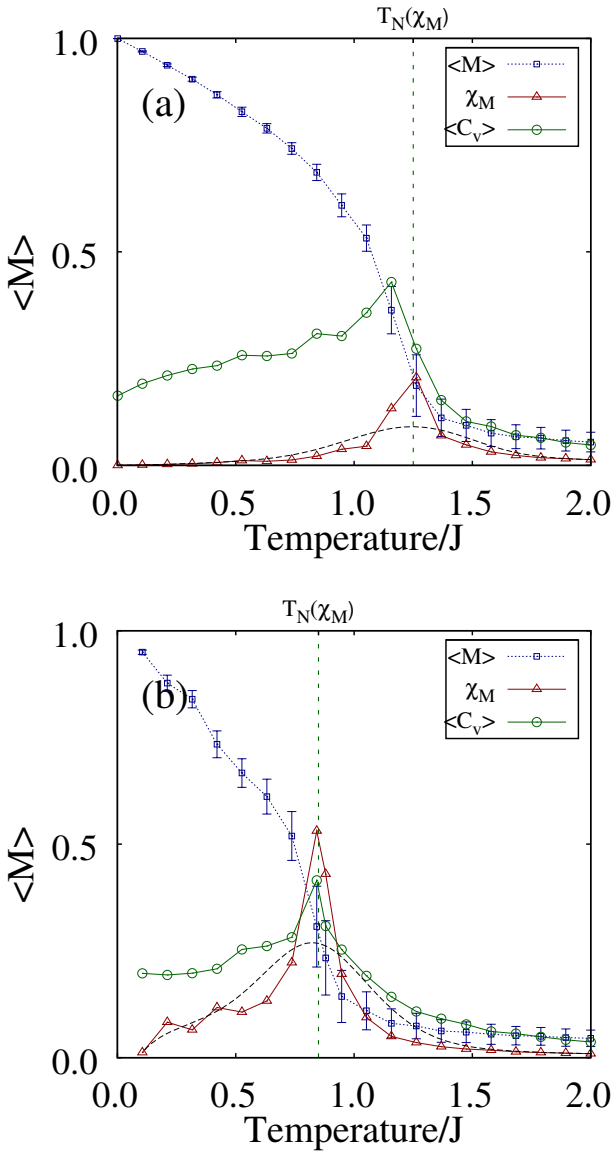

Figure 3.8: MC calculations for the anisotropic 3D Heisenberg model with two sets of values for the couplings as a test to compare with previous literature: (a) $J_z = 0.5$, $J_x = J_y = 1.0$ and (b) $J_z = 0.1$, $J_x = J_y = 1.0$, on a $10 \times 10 \times 10$ lattice.

3.5 Addressing the new $BiFeO_3$ experimental results

Our main goal is to analyze the origin of the substantial reduction of the critical temperature T_N between the two BFO phases, the tetragonal R-phase and the orthorhombic T-phase recently found by MacDougall et al. (2012). According to the well-known Harrison's formula Harrison (1989), the superexchange J is proportional to r^{-14}, where r is the Fe-O-Fe bond length. Note that this formula does not incorporate the bending of the Fe-O-Fe bonds; it is assumed to be straight. By setting the J_x=J_y coupling of the R-phase as our unit, from the experimental information provided to us we get the J values of both phases:

lattice	J_x	J_y	J_z
R-phase	1.0	1.0	0.868
T-phase	1.4332	2.4106	0.1013

We performed the MC calculations on a $L = 10$ 3D lattice using the J values shown in the table above. In the MC calculation, two quantities were measured: χ_M, which is proportional to $\beta\langle\Delta(M)^2\rangle$, and the heat capacity C_v which is proportional to $\beta^2\langle\Delta(E)^2\rangle$.

The MC L=10 results show that the magnetic transitions of the two phases are substantially different (Fig. 3.9). For the R-phase, the $T_N(\chi)(\sim 1.45)$ is just a little higher than the one coming from the specific heat $T_N(C)(\sim 1.4)$. Thus, this case seems reasonable and all is clear. However, for the phase we are the most interested in, the T-phase, the critical temperature coming from the magnetic susceptibility $T_N(\chi)(\sim 1.2)$ is considerably lower than the critical temperature from the specific heat $T_N(C)(\sim 1.5)$.

Note also that the actual value of χ is much higher in magnitude in the T-phase than the value it takes in the R-phase, suggesting a stronger influence of fluctuations. In fact, we believe that the difference is caused by the weak J_z coupling (~ 0.1) in the T-phase that affects substantially the results.

Consider a 2D lattice with J_x and J_y equal to those in the T-phase, namely just drop the coupling in the z-direction and let us see what happens. The results are in Fig. 3.10), where we find a $T_N(C)(\sim 1.45)$ which is almost the same as the one found for the 3D T-phase in the previous figure, while $T_N(\chi)(\sim 1.45)$ now is much higher than that in the 3D T-phase, which is difficult to understand. The weak coupling of the T-phase along the z axis ($J_z \sim 0.103$) must be creating strong fluctuations in the G-AFM-type magnetic order but apparently much weaker fluctuations in the total energy.

In view of the quasi-2D character of the T-phase, a careful size study is imperative. Using a L=12 lattice, the Néel temperatures drops by ~ 0.05 from the results of the L=10 calculation (Fig. 3.11). We have also done calculations for several other lattice sizes. The comparison of $T_N(\chi)$ between lattice sizes L=6, 8, 10, 12, 16 and L=20(Fig. 3.13) is presented in the table below:

lattice size L	R-phase	T-phase
6	1.45	1.2
8	1.45	1.23
10	1.425	1.2
12	1.4	1.15
16	1.425	0.95
20		0.85
∞(*prediction*)	1.375	0.4

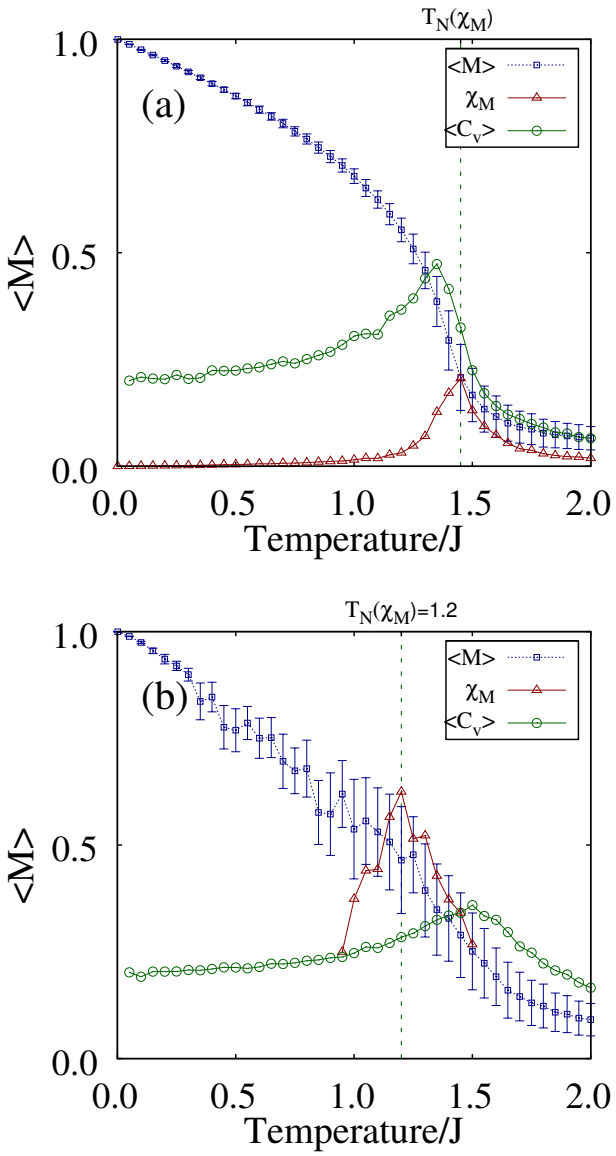

Figure 3.9: MC calculations for the anisotropic 3D Heisenberg model with two sets of J values: (a) are results for the J's corresponding to the R-phase (L=10). Here, both the specific heat and magnetization give similar results. (b) Results for the couplings corresponding to the T-phase, using a L=10 lattice. Here, $T_N(\chi_M)$ of the T-phase appears to be equal to 1.2 from the magnetization analysis, but the specific heat has the peak at a higher temperature. For the R-phase (a), we have done 10 K MC thermal steps and 10 K measurement steps at each temperature. For the T-phase (b), we have done 20 K MC thermal steps and 40 K measurement steps at each temperature. More specifically, the magnetic susceptibility was measured under 30 K MC thermal steps and 100 K measurement steps at each temperature. In each MC step, the number of spin flips is doubled to improve the accuracy of $T_N(\chi_M)$.

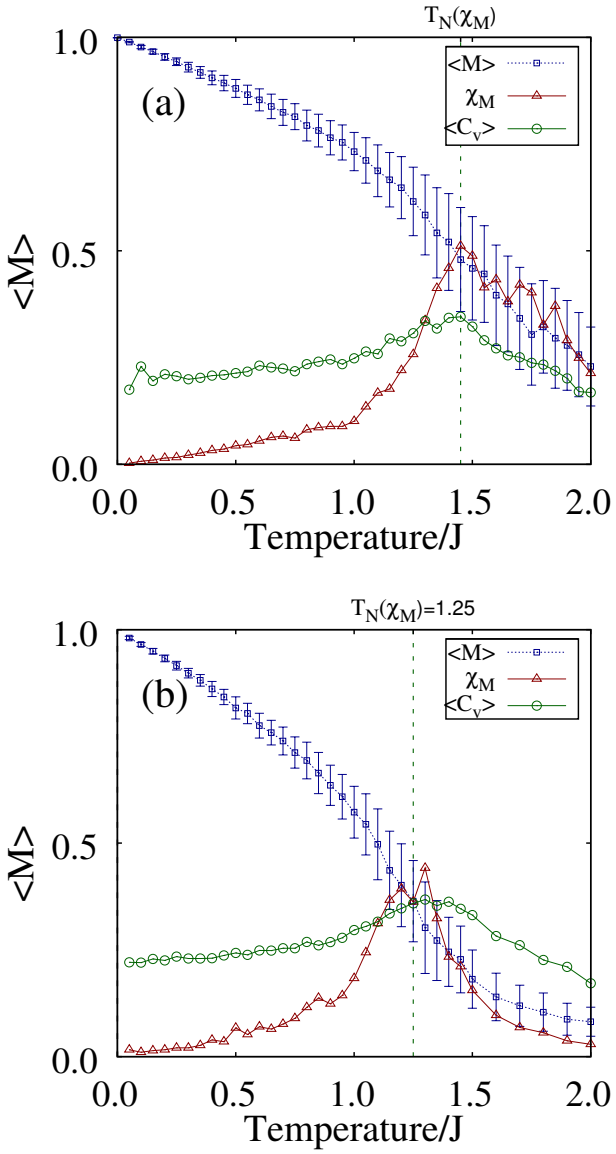

Figure 3.10: MC calculations on a two-dimensional lattice with J_x and J_y equal to the values in the T-phase. For (a), we have done 10 K MC thermal steps and 40 K measurement steps at each temperature, using a 10×10 two-dimensional lattice. For (b), we have done 10 or 20 K MC thermal steps and 80 or 300 K measurement steps at each temperature using a 30×30 two-dimensional lattice. Note the move toward lower critical temperatures between (a) and (b) by increasing the lattice size. This is to be expected when using two-dimensional systems.

Thus, if we define the critical temperature via the peak in the magnetic susceptibility, as opposed to other criteria such as the broad bump in the specific heat, then we observe a clear difference between the R- and T-phases. If the critical temperature of the R-phase in J units coming from the MC calculation is made equal to 640 K, then the critical temperature of the T-phase would be $(0.4/1.375)\times 640$ K which is 186 K, in good agreement with experiments MacDougall et al. (2012).

Let us explain some of the details that have allowed us to make the bulk extrapolation described above:

(1) Since the T-phase has a very weak J coupling along the z-axis, this quasi-2D system presents larger finite size effect than the R-phase (since we know the size effects in 2D are very large since all finite lattices suggest the presence of a finite critical temperature while in the bulk Mermim-Wagner establishes that the critical temperature is zero). As the lattice sizes are increased, the $T_N(\chi)$ of the T-phase should decrease more that that of the R-phase, as the results in the table above show.

(2) As already expressed, we have observed strong fluctuations in the T-phase during the magnetic transition (Fig. 3.12). As a result, to get a smooth $T_N(\chi)$ vs. temperature curve, we believe that additional MC measurement steps (80 K at least) are required for the T-phase MC calculations. It is for this reason that we have increased the number of MC steps for all the calculations involving the T-phase, as explained in many of the figure captions.

(3) We carry out a finite-size scaling for the T-phase employing larger lattices. The main challenge is provided by the strong fluctuations in the magnetization. This requires much longer MC measurement steps than usual (some results are in Fig. 3.13). Our result (Fig. 3.15) shows that the 3D and 2D T-phases have a larger finite size effect than the 3D R-phase. As a result, the T_N difference between the R-phase and the T-phase is larger in the bulk limit extrapolation than it is for the individual finite lattices. As already explained, assuming the T_N of the R-phase at bulk limit is 640 K, the corresponding T_N of the 3D T-phase should be approximately 200 K. This

explains the significant Néel temperature difference between the tetragonal R-phase and the orthorhombic T-phase.

3.6 Differences between the Quasi-2D T-phase and the truly 2D T-phase

The contents of this section are not crucial for the "bottom line" critical temperature estimation, but are important for the consistency of the theoretical approach:

We have noticed, as a curiosity, that in our calculations a 2D lattice has higher T_N than an equivalent quasi-2D lattice (Figs. 3.10 and 3.15), with the same linear size. In order to explain this unexpected phenomena, we have compared three different types of T-phase lattice simulations: (1) 3D T-phase with $J_z = 0.0$ (here there will be many decoupled planes all contributing independently to the results), (2) 3D T-phase with the realistic $J_z = 0.1013$, and (3) an equivalent 2D T-phase (here there is only one plane).

Our MC results (Fig. 3.16) show that when the J_z was set to zero in the 3D lattice, i.e. when many planes contributed to the results but they were decoupled, the magnetic susceptibility *diverges* at zero temperature which is strange. The explanation is the following: at low temperatures, the spins in the $x-y$ plane will tend to form nearly perfect AFM spin configurations since the correlation length is huge for any of the lattices we can numerically study. However, the planes are decoupled along the z-axis. As a result, at low temperatures, the total magnetic susceptibility can be simplified by treating each plane as *one* single spin (note: M represents $|\vec{M}|$. $\vec{M}$ is the staggered magnetization of each layer):

$$\begin{aligned}\langle\chi\rangle &= N\beta\langle M - \langle M\rangle\rangle^2 \\ &= \frac{N\beta}{4\pi}\int_0^{2\pi}\int_0^{\pi}(cos\theta - 0)^2 sin\theta d\theta d\phi \\ &= \frac{2N\beta}{3}.\end{aligned} \tag{3.2}$$

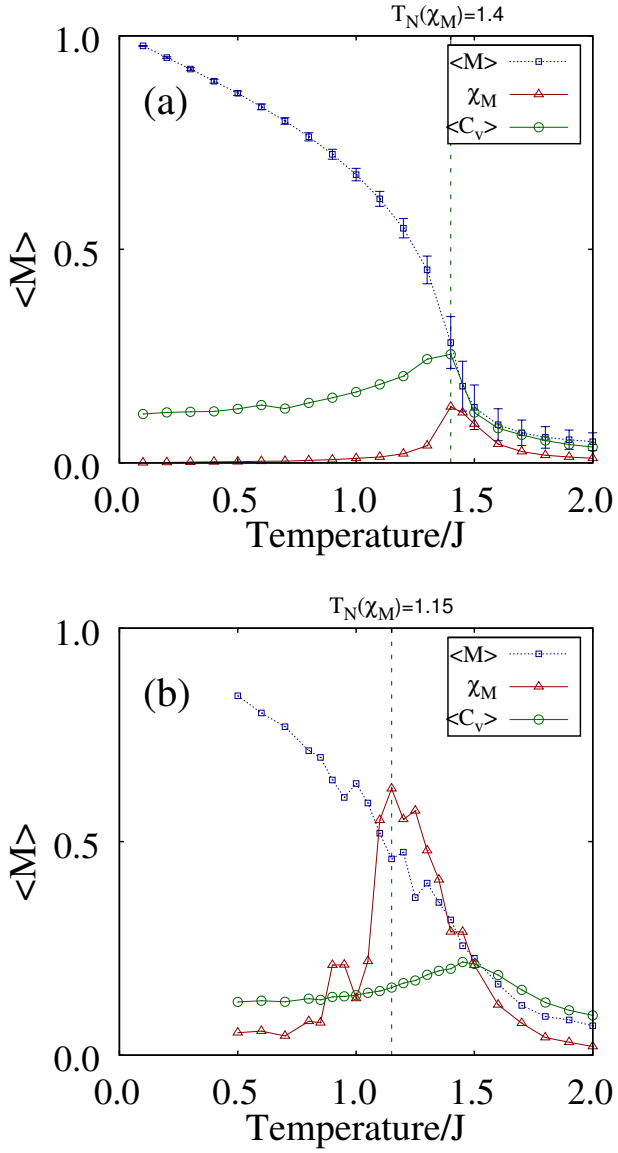

Figure 3.11: MC calculations for the 3D anisotropic Heisenberg model with two sets of J values: (a) R-phase (L=12), (b) T-phase (L=12). For the R-phase (a), we have used 10 K MC thermal steps and 10 K measurement steps at each temperature. For the T-phase (b), we have used 30 K MC thermal steps and 80 K measurement steps at each temperature.

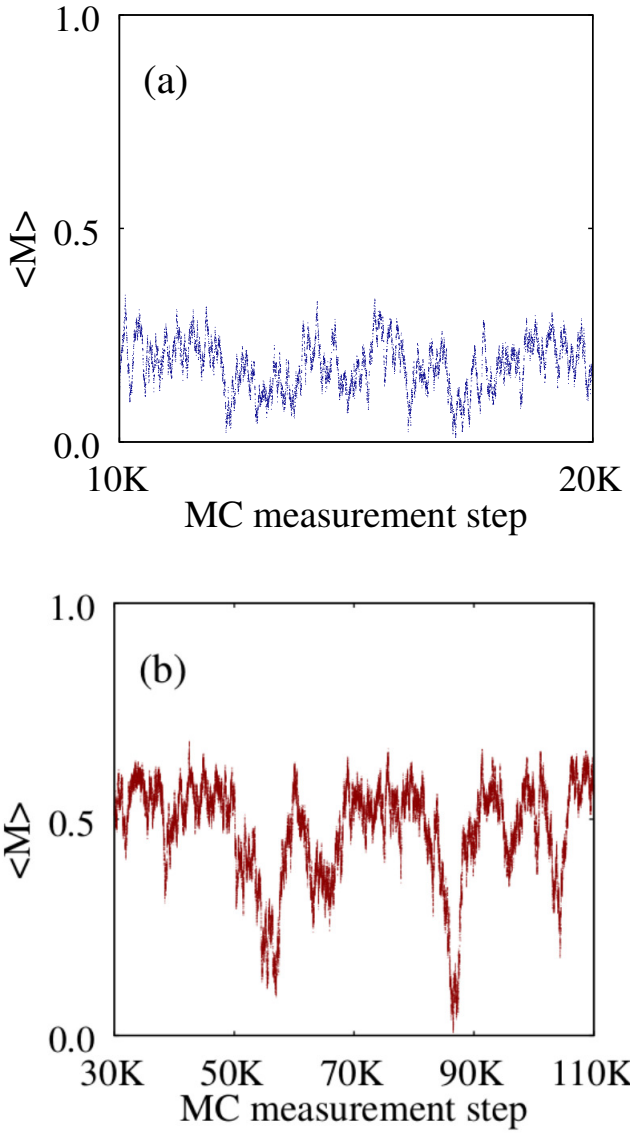

Figure 3.12: Magnetization versus MC measurement steps (i.e. MC "time" evolution) for a 3D lattice close to the Néel temperature: (a) corresponds to the R-phase with T=1.4, and L=12. Here the fluctuations are reasonable. So this R-phase involves no problems at all; (b) corresponds to the T-phase at T=1.15, and L=12. Here the fluctuations are much wilder. This is also clear from the large value of the magnetic susceptibility in the T-phase, as previously discussed.

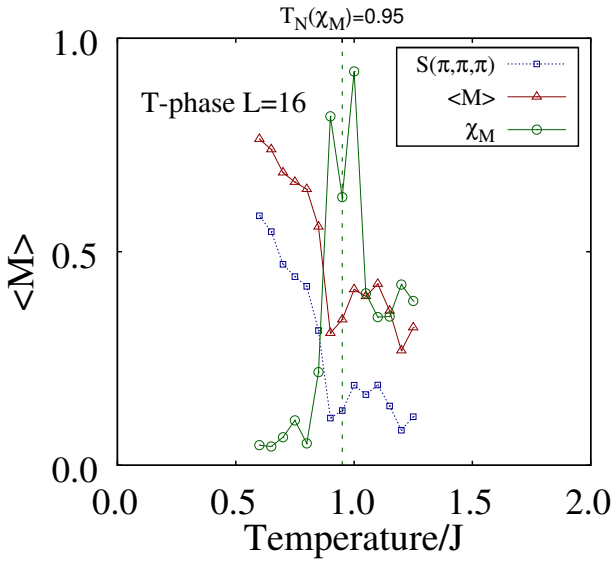

Figure 3.13: MC calculations for the T-phase using a three-dimensional lattice of linear size $L = 16$. We have used 50 K MC thermal steps and 200 K measurement steps (4K measurement steps for the S(k)) at each temperature. Notice that the $S(\pi, \pi, \pi)$, χ_M and $\langle M \rangle$ curives shows the same Néel temperature at about 0.95.

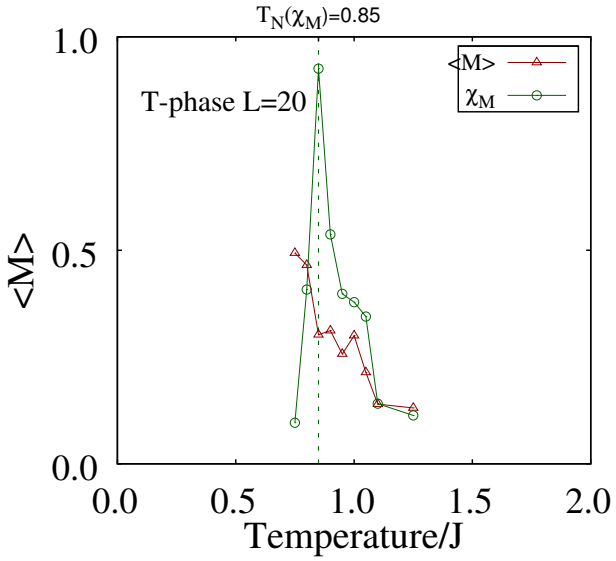

Figure 3.14: MC calculations for the T-phase using a three-dimensional lattice of linear size $L = 20$. We have used 50 K MC thermal steps and 200 K measurement steps at each temperature.

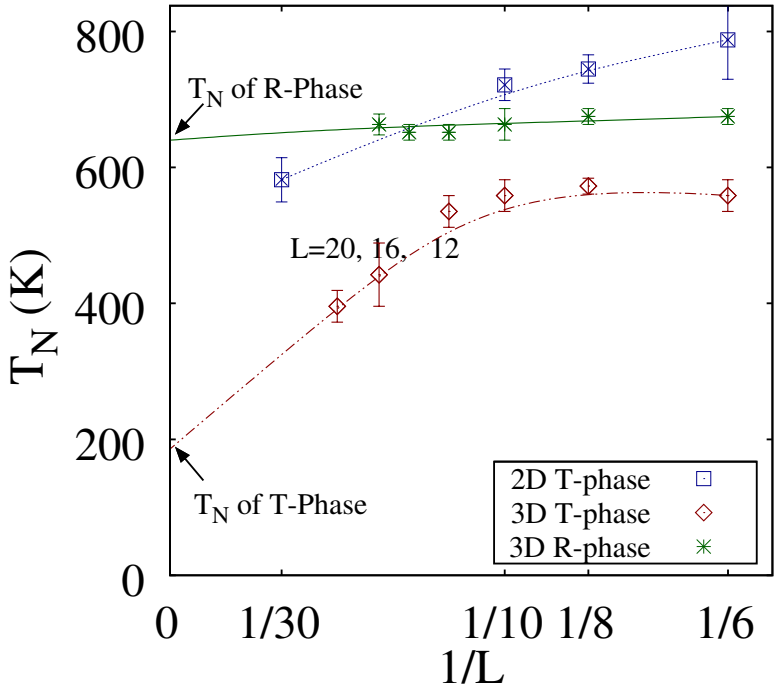

Figure 3.15: The convergence tendency of the critical temperatures $T_N(\chi_M)$ deduced from the magnetic susceptibility for three different cases. Shown are the two-dimensional T-phase (just one plane), the three-dimensional T-phase, and the three-dimensional R-phase. We can see a clear tendency of T_N to drop with increasing the lattice size. However, compared to the T-phase, the 3D R-phase has a much smaller finite size effect. Assuming the T_N of the R-phase in the bulk limit is 640 K, the corresponding T_N of the 3D T-phase should be approximately 200 K.

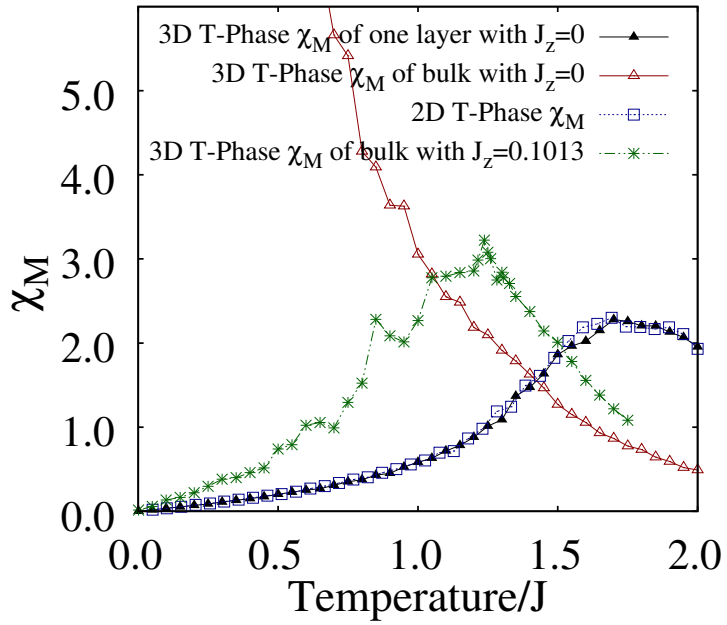

Figure 3.16: The comparison between four different calculations. The magnetic susceptibility of the T-phase using a $6 \times 6 \times 6$ three-dimensional lattice with $J_z = 0$ is found to diverge at low temperature (red curve). This strange behavior is explained in the text. The susceptibility of just one layer of spins (black curve) extracted from the 3D study is equal, as expected, with that of an isolated 6×6 2D lattice (blue curve). The green curve is for a $6 \times 6 \times 6$ 3D T-phase with the realistic coupling $J_z = 0.1013$. These calculations are done using $6 \times 6 \times 6$ 3D lattices and a 6×6 2D lattice. We have used 10 K MC thermal steps and 200 K measurement steps at each temperature. Note the somewhat paradoxical result that the peak in the 2D study is at a higher T than the 3D T-phase, but remember than in 2D there are huge size effects.

In our study with a $L = 6$ quasi-2D lattice (i.e. 6 decoupled planes), the theoretical χ is equal to 4β. As shown in Fig. 3.17, this theoretical approximation matches very well our MC results at low temperature, showing that at least this paradox has been understood. At higher temperature ($T > 0.75$), the χ_M measured by the MC calculation is smaller than the theoretical χ_M due to the in-plane spin fluctuations.

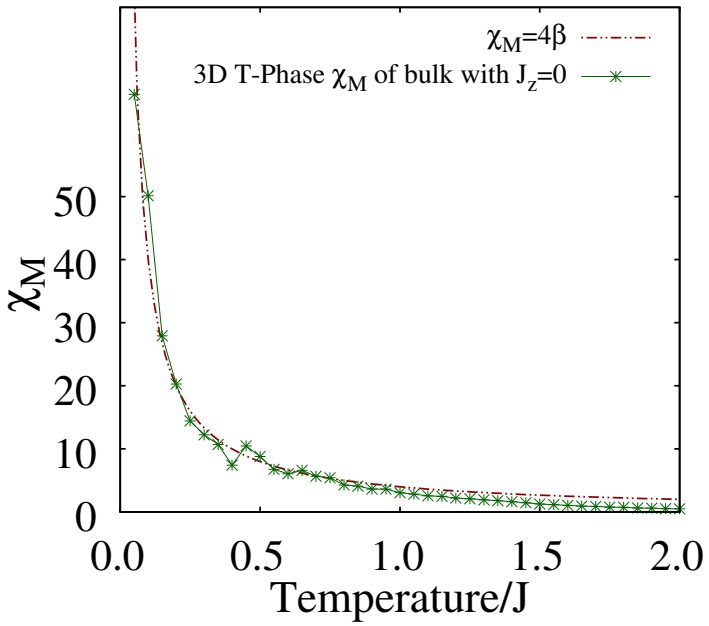

Figure 3.17: The comparison between the MC results for a T-phase system with J_z=0, and mean field calculations. The χ_M from the mean-field calculation is equal to $4/T$. The χ_M of MC calculation has a lower value only at high temperatures where in-plane spin fluctuation reduces the total magnetic order, but at low T there is good agreement. Then, the divergence comes from the decoupling of the planes, with each one behaving like an independent spin, as explained in the text.

3.7 Why the 3D T-phase has a lower T_N than the 2D T-phase in a finite lattice

As we know from the Mermin-Wagner theorem, a 2D lattice does not have the long range order. However, it is very difficult for us to see this zero temperature transition in a Monte Carlo 2D Heisenberg model calculation due to the limitations from our computer resources. As a result, a 12×12 2D T-phase having a higher T_N than a $12 \times 12 \times 12$ 3D T-phase does not violate the Mermin-Wagner theorem. Fortunately, we know that a 3D lattice will have a non-zero Néel temperature in the bulk limit. We made an "idea" graph (Fig. 3.18) for the T_N at the bulk limit to show that the T_N of a 2D T-phase will drop to zero at infinite size limit.

We also want to explain why the 3D T-phase has a lower T_N than the 2D T-phase (just one plane) in a finite lattice ($L < 30$). This interesting phenomena can be explained by the z-direction disorder caused by the weak J_{AF} coupling. As shown in Fig. 3.19, in the 3D T-phase, the J_z is much weaker than the J_x and J_y. When temperature cools down below the magnitude of J_x and J_y, the spins in each x-y plane are frozen into a 2D G-AFM order. But the weak J_z coupling requites a much lower critical temperature to stabilize the z direction AFM order.

Summarizing, the 2D lattice only presents a higher T_N than the 3D lattice if the following conditions are met: (1) It is a relatively smaller lattice than a big lattice where the Mermin-Wagner theorem starts to play an important role. (2) The 3D lattice is a Quasi 2D system where x-y planes are weakly coupled.

3.8 Differences between the Spin Structure Factor and the Staggered Magnetization

In most cases, we were using the staggered magnetization instead of the spin structure factor as the the order parameter to determine the Néel temperatures for the cases of

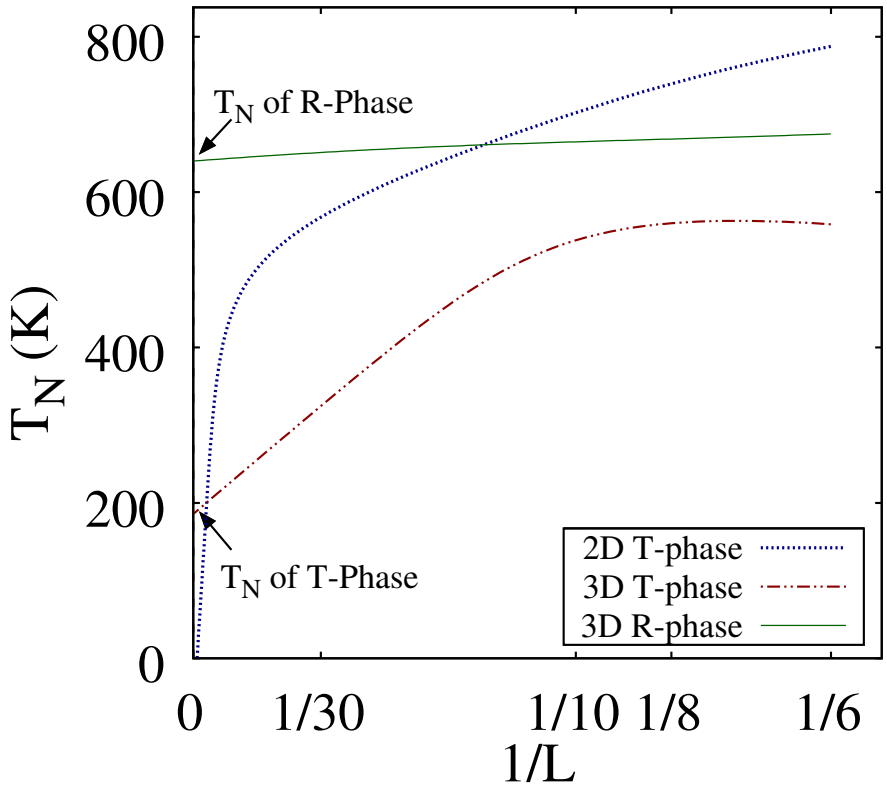

Figure 3.18: The convergence tendency of the critical temperatures $T_N(\chi_M)$ deduced from the magnetic susceptibility for three different cases. Shown are the two-dimensional T-phase (just one plane), the three-dimensional T-phase, and the three-dimensional R-phase.

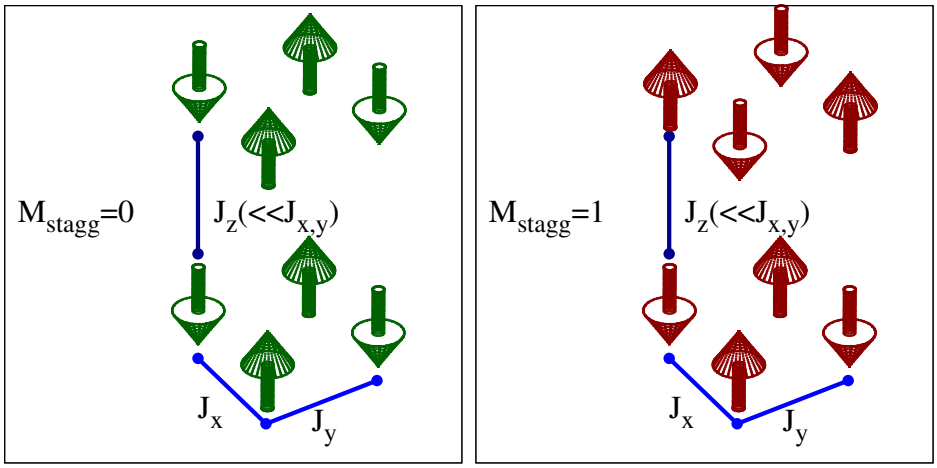

Figure 3.19: Sample spin configurations with $2 \times 2 \times 2$ lattice size. The z-direction AFM order requites a lower Néel temperature than that is required to stabilize a G-AFM order in each x-y plane. The two green and red spin configurations represent two near degenerate states with tiny energy difference from the J_z coupling. They both have G-AFM order in each x-y plane. But the opposite z direction spin arrangement gives out different M_{stagg} and spin structure factor. Only a lower temperature can break this near degeneracy.

interest, particularly the 3D T-phase. This is in part because the spin structure factor requires much more computation than the staggered magnetization. In relatively small lattices (L=6), the temperature dependence of the spin structure factor at (π, π, π) has been compared with the staggered magnetization. As shown in Fig. 3.20 (and Fig. 3.13 for L=16), the use of the spin structure factor, or the magnetization, or the magnetic susceptibility are all approximately equivalent for the R-phase. With regards to the T-phase, as already explained the magnetic susceptibility peaks at a temperature where both the magnetization and the spin structure factor are still very robust. But observing carefully the plot, the temperature where the spin structure factor changes *curvature* is close to the position of the magnetic suscep. peak. The same can be said about the magnetization. What perhaps remains as the main paradox is why the specific heat has the peak at appreciably higher temperatures than the other observables would suggest, but we will need to address this in the future.

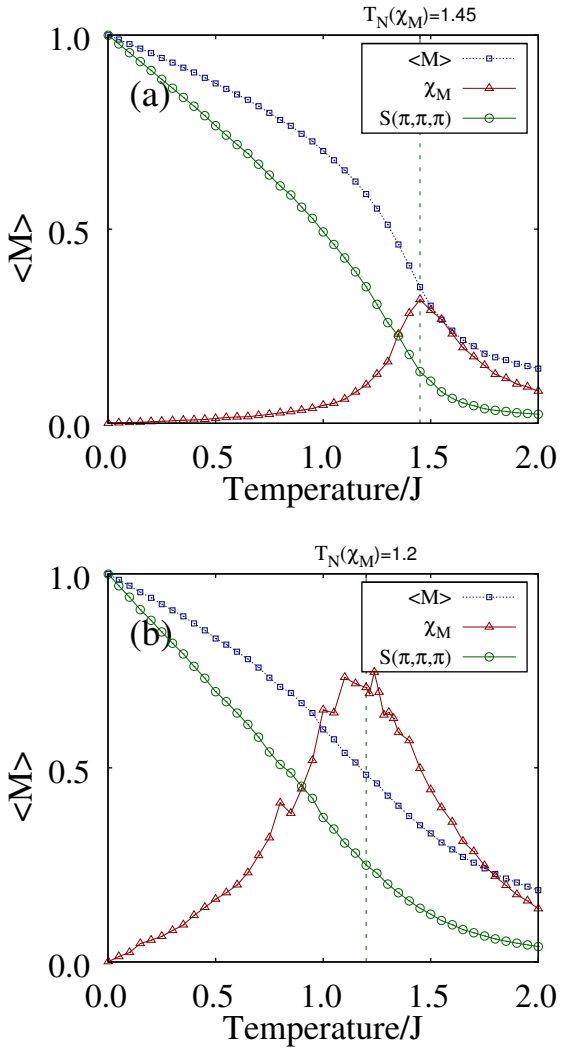

Figure 3.20: The comparison between the staggered magnetization $\langle M \rangle$ and spin structure factor $S(\pi, \pi, \pi)$, using a 3D anisotropic Heisenberg model with L=6. The results shown are for (a) R-phase and (b) T-phase. For both calculations, we have used 10 K MC thermal steps and 400 K measurement steps at each temperature. Note that in (b) the temperature where both magnetization and spin structure factor change the sign of their *curvature*, often taken as indication of a critical temperature in numerical studies using a finite lattice, is very similar to the location of the peak in the magnetic susceptibility.

Chapter 4

Transport anisotropy of the pnictides studied via Monte Carlo simulations of a Spin-Fermion model

This chapter is a modified verstion of our submitted paper Liang et al. (2011).

4.1 Introduction.

In early studies of Fe-based superconductors Johnston (2010), it was widely assumed that Fermi Surface (FS) nesting was sufficient to understand the undoped-compounds magnetic order with wavevector $\mathbf{Q} = (\pi,0)$ de la Cruz et al. (2008) and the pairing tendencies upon doping. Neutron scattering reports of spin-incommensurate order Pratt et al. (2011) are in fact compatible with the nesting scenario. However, several recent experimental results cannot be explained by FS nesting, including *(i)* electronic "nematic" tendencies in $Ca(Fe_{1-x}Co_x)_2As_2$ Chuang et al. (2010); *(ii)* orbital-independent superconducting gaps Shimojima et al. (2010) found using

laser angle-resolved photoemission (ARPES) spectroscopy on $BaFe_2(As_{0.65}P_{0.35})_2$ and $Ba_{0.6}K_{0.4}Fe_2As_2$; and, more importantly for the investigations reported here, *(iii)* the report of local moments at room temperature (T) via Fe X-ray emission spectroscopy Gretarsson et al. (2011); Bondino et al. (2008). Considering these experiments and others, a better characterization of the pnictides is that they are in the "middle" between the weak and strong Coulomb correlation limits Qazilbash et al. (2009); Yu et al. (2009a); Z. P. Yin and Kotliar (2011). Because this intermediate Hubbard U range is difficult for analytical approaches, there is interest in the development of simpler models that can be studied via computational techniques to provide insight into such a difficult coupling regime. The Hartree-Fock (HF) approximation to the Hubbard model Luo et al. (2010) cannot be applied at room T since HF approximations only lead to non-interacting fermions above the ordering temperature T_N, and thus the local moment physics Gretarsson et al. (2011) cannot be reproduced due to the "sign problem".

Recently, a Spin-Fermion (SF) model for the pnictides has been independently proposed by Lv *et al.* Krüger et al. (2009) and Yin *et al.* Yin et al. (2010). The model, very similar to those widely discussed for manganites, originally involved itinerant electrons in the xz and yz d-orbitals coupled, via an on-site Hund interaction, to local spins (assumed classical) that represent the magnetic moment of the rest of the Fe orbitals (considered localized). The Hund interaction is supplemented by a nearest-neighbor (NN) and next-NN (NNN) classical Heisenberg spin-spin interaction. This SF model has interesting features that makes it qualitatively suitable for the pnictides, particularly since by construction the model has itinerant electrons in interaction with local moments Gretarsson et al. (2011); Bondino et al. (2008) at all temperatures.

Phenomenological SF models have been proposed before for underdoped cuprates, with itinerant fermions representing carriers locally coupled to classical spins representing the antiferromagnetic order parameter. These investigations unveiled stripe tendencies Buhler et al. (2000), ARPES and optical conductivity results Moraghebi et al. (2001, 2002a) similar to experiments, and even the dominance of the d-wave

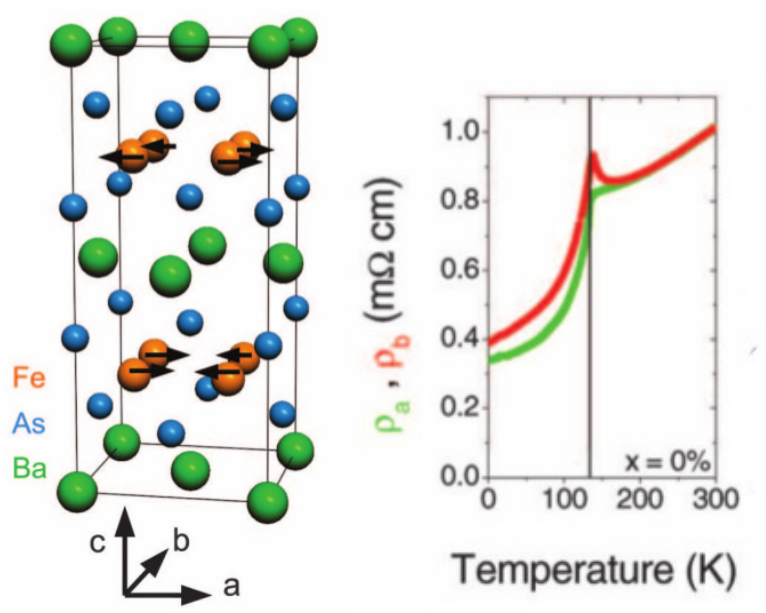

(a) **(b)**

Figure 4.1: (a) Detwined sample with uniaxial Pressure along the FM direction. (b) Resistivity along AF direction is smaller than that along the FM direction with a $(\pi, 0)$ magnetic order.

channel in pairing Moraghebi et al. (2002b). Thus, it is natural to apply now these ideas to the Fe superconductors.

As remarked already, SF models are also mathematically similar to models used for the manganites Dagotto et al. (2001). Then, all the experience accumulated in the study of Mn-oxides can be transferred to the analysis of SF models for Fe-superconductors. In particular, one of our main objectives is to study for the first time a SF model for pnictides employing Monte Carlo (MC) techniques, allowing for an unbiased analysis of its properties. Moreover, to test the model, challenging experimental results will be addressed. It is known that for detwinned $Ba(Fe_{1-x}Co_x)_2As_2$ single crystals (Fig. 4.1-a), a puzzling transport anisotropy has been discovered between the ferromagnetic (FM) and antiferromagnetic (AFM) directions Chu et al. (2010); I.R. Fisher and Shen (2011).

In addition, the resistivity vs. T curves display an unexpected peak at $T_N \sim 130$ K (Fig. 4.1-b), and the presumably weak effect of an applied uniaxial stress Chu et al.

(2010); I.R. Fisher and Shen (2011) still causes the anisotropy to persist well beyond T_N. However, recent neutron results suggest that the transport anisotropy may be actually caused by strain effects that induce a shift upwards of the tetragonal-orthorhombic and T_N transitions Dhital et al. (2012); Blomberg et al. (2012), as opposed to a spontaneous rotational symmetry-breaking state not induced by magnetism or lattice effects. Then, theoretical guidance is needed. While the low-T anisotropy was already explained as caused by the coupling between the spins and orbitals in the $\mathbf{Q}$=$(\pi, 0)$ state Zhang and Dagotto (2011), the full transport curves at finite T define a challenge that will be here addressed for the nontrivial undoped case.

4.2 *Model and Method.*

The SF model Krüger et al. (2009); Yin et al. (2010) is given by

$$H_{\rm SF} = H_{\rm Hopp} + H_{\rm Hund} + H_{\rm Heis}. \tag{4.1}$$

The first term $H_{\rm Hopp}$ describes the Fe-Fe hopping of itinerant electrons. To better reproduce the band structure of pnictides Johnston (2010), three d-orbitals (xz, yz, xy) will be used instead of two.

$$H_{\rm Hopp} = -\sum_{<ij>}^{\sigma,\alpha,\beta} t_r^{\sigma,\alpha,\beta}(d^\dagger_{i,\alpha,\sigma} d_{j,\beta,\sigma} + H.c.)$$

The full expression for $H_{\rm Hopp}$ can be found in Eqs.(1-3) of Ref. Daghofer et al. (2010b).

The hopping parameters $t_r^{\alpha,\beta}(\alpha, \beta = xz, yz, xy)$ are organized into four 3×3 matrices:

Table 4.1: Δ_{xy} represents the xy orbital on-site energy. This table is reproduced from Table I of Ref. Daghofer et al. (2010b)

t_1	t_2	t_3	t_4	t_5	t_6	t_7	t_8	Δ_{xy}
0.02	0.06	0.03	-0.01	-0.2	0.3	-0.2	-0.1	0.4

$$T_{\hat{x}} = \begin{pmatrix} t_2 & 0 & t_7^* \\ 0 & t_1 & 0 \\ t_7^* & 0 & t_5 \end{pmatrix}$$

$$T_{\hat{y}} = \begin{pmatrix} t_1 & 0 & 0 \\ 0 & t_2 & t_7^* \\ 0 & t_7^* & t_5 \end{pmatrix}$$

$$T_{\hat{x}+\hat{y}} = \begin{pmatrix} t_3 & -t_4 & t_8^* \\ -t_4 & t_3 & t_8^* \\ -t_8^* & -t_8^* & t_6 \end{pmatrix}$$

$$T_{\hat{x}-\hat{y}} = \begin{pmatrix} t_3 & t_4 & t_8^* \\ t_4 & t_3 & -t_8^* \\ -t_8^* & t_8^* & t_6 \end{pmatrix}$$

In the tight binding Hamiltonian, $t_7^* = t_7 \cdot (-1)^{|i+j|}$ and $t_8^* = t_8 \cdot (-1)^{|i+j|}$. The $(-1)^{|i+j|}$ factor is from the staggered As modulation out of the FeAs layer.

The actual values of the hopping parameters $t_1 \sim t_8$ in eV's are listed below:

The density of relevance used here is n=4/3 Daghofer et al. (2010b). At this filling, we are able to produce the correct Fermi surface comparing with the results from ARPES and the density function theory (Fig. 4.2).

The Hund interaction is simply $H_{\text{Hund}}=-J_{\text{H}}\sum_{\mathbf{i}\alpha}\mathbf{S_i}\cdot\mathbf{s}^{\alpha}{}_{\mathbf{i}}$, with $\mathbf{S_i}$ the classical spin at site $\mathbf{i}$ ($|\mathbf{S_i}|$=1), and $\mathbf{s}^{\alpha}{}_{\mathbf{i}}$ the itinerant-fermion spin of orbital α. Although

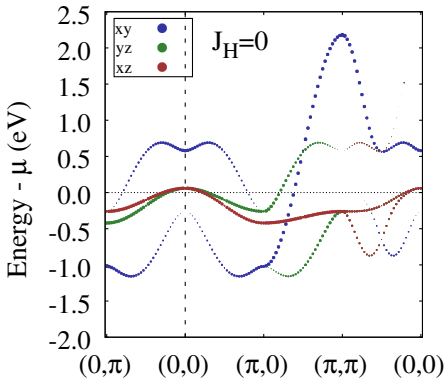

Figure 4.2: Band structure of the tight binding Hamiltonian from Ref. [Daghofer et al. (2010b)]. The chemical potential is adjusted to n=4/3. At the Fermi energy, there are two hole pockets at the Gamma point, and two electron pocket at the X and Y points.

the fermions do not have a direct Hund interaction among themselves, an effective one is generated via the interaction with the classical variables. (more formally, "integrating out" the classical spins should induce a Hund coupling among the fermions). The last term $H_{\rm Heis}$ contains the spin-spin interaction among the localized spins $H_{\rm Heis}$=$J_{\rm NN}\sum_{\langle \mathbf{ij}\rangle}\mathbf{S_i}\cdot\mathbf{S_j}$ + $J_{\rm NNN}\sum_{\langle\langle \mathbf{im}\rangle\rangle}\mathbf{S_i}\cdot\mathbf{S_m}$, where $\langle\rangle$ ($\langle\langle\rangle\rangle$) denotes NN (NNN) couplings. The particular ratio $J_{\rm NNN}/J_{\rm NN}$=2/3 was used in all the results below, leading to $(\pi,0)/(0,\pi)$ magnetism. The transition from (π,π) order to $(\pi,0)/(0,\pi)$ order occurs at $J_{\rm NNN}/J_{\rm NN}$=1/2, within $H_{\rm Heis}$. Any other ratio $J_{\rm NNN}/J_{\rm NN}$ larger than 1/2 would have been equally suitable for our purposes.

The well-known Monte Carlo (MC) technique for SF models Dagotto et al. (2001) will be here used to study $H_{\rm SF}$ at any T. In this technique, the acceptance-rejection MC steps are carried out in the classical spins, while at each step a full diagonalization of the fermionic sector (hopping plus on-site Hund terms) for fixed classical spins is performed via library subroutines in order to calculate the energy of that spin configuration. These frequent diagonalizations render the technique CPU-time demanding. The simulation is run on a finite 8×8 cluster with periodic boundary conditions (PBC) and uses the full $H_{\rm SF}$ model for the MC time evolution

and generation of equilibrated configurations for the classical spins at a fixed T. Typically 20,000 MC sweeps through the lattice are used for thermalization followed by 10,000 for the measurements that occur every 20 configurations. However, for the MC measurements those equilibrated configurations are assumed replicated in space but differing by a phase factor such that a better resolution is reached with regards to the momentum $\mathbf{k}$. Since a larger lattice with more eigenstates gives a more continuous distribution of eigenenergies, the procedure then reduces finite-size effects in the measurements. This well-known method is often referred to as "Twisted" Boundary Conditions (TBC) Salafranca et al. (2009). In practice, phases Φ are added to the hopping amplitudes, schematically denoted as "t", at the boundary via t_{TBC}=$e^{i\Phi}t$, with Φ=$2\pi m/M$ (m=0,1,...,$M-1$) such that the number of possible momenta in the x or y directions becomes L=8×M.

4.3 Results

Figure 4.3(a) contains MC results for the structure factor of the classical spins, defined as $S(\mathbf{q})$=$\frac{1}{N^2}\sum_{\mathbf{i},\mathbf{j}}\langle \mathbf{S_i}\cdot\mathbf{S_j}\rangle e^{i\mathbf{q}\cdot(\mathbf{i}-\mathbf{j})}$ (N = number of sites), illustrating the development of $\mathbf{Q}$=$(\pi,0)$ magnetic order as T is reduced. Since a ratio $J_{\rm NNN}/J_{\rm NN}$>1/2 is "frustrating", finding $\mathbf{Q}$-order at $J_{\rm H}$=0 is not surprising, but Fig. 4.3 shows that this order remains stable turning on $J_{\rm H}$ in the range investigated, as opposed to inducing transitions to other states. The chosen value of $J_{\rm NN}$ in Fig. 4.3(a) leads to a $T_{\rm N}$ similar to that in $BaFe_2As_2$. The low-T orbitally-resolved electronic density-of-states (DOS) is in Fig. 4.3(b). The $\mathbf{Q}$ magnetic order opens a pseudogap (PG) in the yz orbital, while the others are not much affected. This PG generation was previously discussed when contrasting theory and ARPES experiments Daghofer et al. (2010a) and it should not be confused with long-range orbital-order, that in this SF model occurs at $J_{\rm H}$∼0.4 or larger.

Figure 4.3(c) contains the evolution of the 8×8-cluster resistance R increasing the number of momenta via the TBC, calculated via standard procedures Dagotto et al.

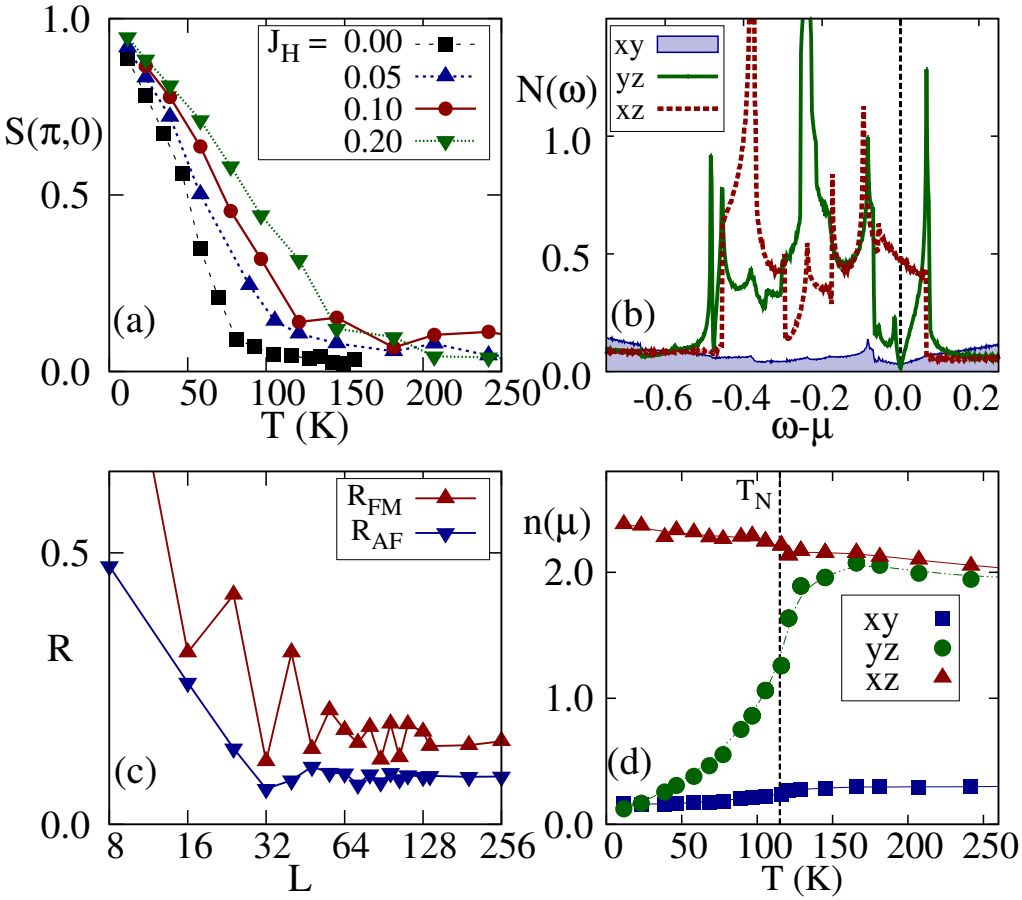

Figure 4.3: (color online) (a) Classical spins structure factor S(π,0) (normalized to 1) vs. T, for the $J_{\rm H}$'s indicated, using the PBC 8×8 cluster and $J_{\rm NN}$=0.015. The oscillations in the data are indicative of the error bars. (b) Density of states $N(\omega)$ of each orbital (μ= chemical potential), using TBC with L=512, at T=0 K and $J_{\rm H}$=0.1 eV, for the perfect $(\pi, 0)$ magnetic state. (c) Resistance R vs. L (TBC 8×8) for the FM and AFM directions of the perfect $(\pi, 0)$ magnetic state ($J_{\rm H}$=0.1 eV). (d) The occupation at the FS $n(\mu)$ (see text) of the three orbitals vs. T, using L=256. A coupling $J_{\rm NN}$=0.016 (0.014) along the x (y) axis was used (see text).

(2001); Vergés (1999). While the ratio of R's along the FM and AFM directions is always > 1, i.e. qualitatively correct, TBC with L=256 is needed to reach stable values. In addition, the occupation of the three orbitals at the FS (Fig. 4.3(d)) was defined as $n(\mu)=\int d\epsilon n(\epsilon)\beta e^{\beta(\epsilon-\mu)}/(1+e^{\beta(\epsilon-\mu)})^2$, involving the μ-derivative of the fermionic population. As T increases and the **Q** order weakens, the xz-yz orbitals populations converge to the same values.

The results of Fig. 4.3, and others below, were obtained introducing a "small" explicit asymmetry along the x and y axes for $J_{\rm NN}$, namely a generalized $J^{\alpha}_{\rm NN}$ (α=x, y) was used. Its purpose is to mimic the orthorhombic distortion and strain effects de la Cruz et al. (2008); Dhital et al. (2012); Blomberg et al. (2012) and judge if the present calculations reproduce transport experiments Chu et al. (2010); I.R. Fisher and Shen (2011); Dhital et al. (2012); Blomberg et al. (2012). Consider the ratio $r_{\rm NN}$=$J^x_{\rm NN}/J^y_{\rm NN}$. Using the dependence of the hopping amplitudes with the distance u between d- and p-orbitals i.e. $t_{pd}\sim 1/u^{7/2}$ Harrison (1989), the angles involved in the Fe-As-Fe bonds, the low-T lattice parameters de la Cruz et al. (2008), fourth-order perturbation in the hoppings for the Fe-Fe superexchange, and, more importantly, neglecting contributions of the yz orbital that is suppressed at the Fermi level Daghofer et al. (2010a) as long as $(\pi, 0)$ spin fluctuations dominate leads to a crude estimation $r_{\rm NN}\sim$1.4. Since this is likely an upper bound, the ratio used in our MC simulation $r_{\rm NN}\sim$1.14, assumed to be temperature independent, is reasonable. Other crude estimations including the direct Fe-Fe hoppings Harrison (1989) or employing the lattice parameters under pressure Dhital et al. (2012) lead to similar ratios. Then, our asymmetry value is qualitatively realistic.

Previous investigations Luo et al. (2010) showed that the T=0 HF approximation to the undoped multiorbital Hubbard model can reproduce neutron diffraction results and ARPES data. A similar degree of accuracy should be expected from any reasonable model for the pnictides, including $H_{\rm SF}$. To test this assumption, the one-particle spectral function $A(\mathbf{k}, \omega)$ was calculated, and the FS at different T's is shown in Fig. 4.4, contrasted against the low-T fermionic non-interacting limit $J_{\rm H}$=0.

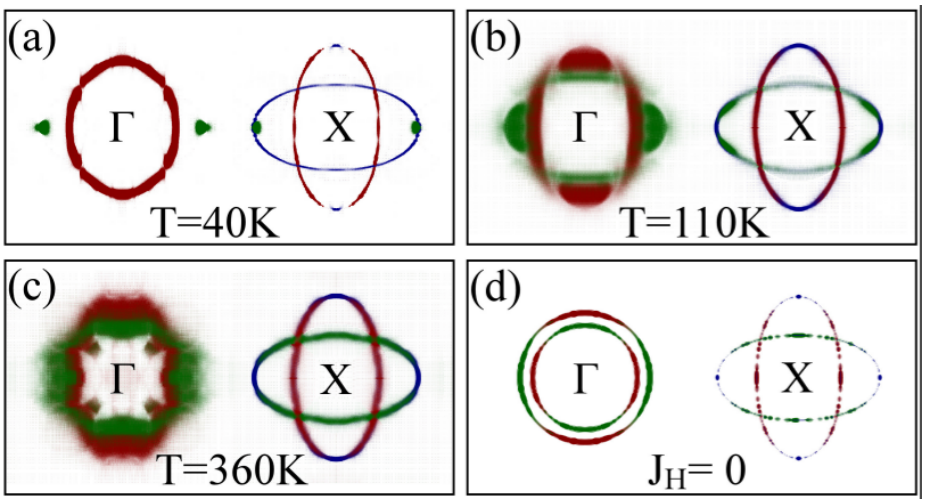

Figure 4.4: (color online) $A(\mathbf{k},\omega)$ at $\omega{=}\mu$ (TBC 8×8 L=512). The model used (see Ref. Daghofer et al. (2010b)) includes the staggered As modulation out of the FeAs layer. Thus, our results are in the *folded* Brillouin zone convention, and for this reason two electron pockets (as opposed to just one) are centered at X in the panels above. The pocket elongated vertically at X would corresponds to a pocket at Y in the unfolded convention if the As modulation is considered via a quasicrystal momentum Daghofer et al. (2010b). (a-c) are for J_{H}=0.1 eV. Red, green, and blue are for the xz, yz, and xy orbitals, respectively. (a) $T{=}40K$, below T_{N}. The $(\pi,0)$ magnetic order induces yz-orbital electron satellite pockets. (b) $T{=}110K{\sim}T_{\mathrm{N}}$. In this regime, the MC configurations display small coexisting patches of $(\pi,0)$ and $(0,\pi)$ order (see text), creating almost symmetric xz and yz features around Γ. (c) Large T=360 K, with no remnants of the $(\pi,0)$ order. The FS becomes a broaden version of the non-interacting FS at J_{H}=0, shown in (d) at T=100 K.

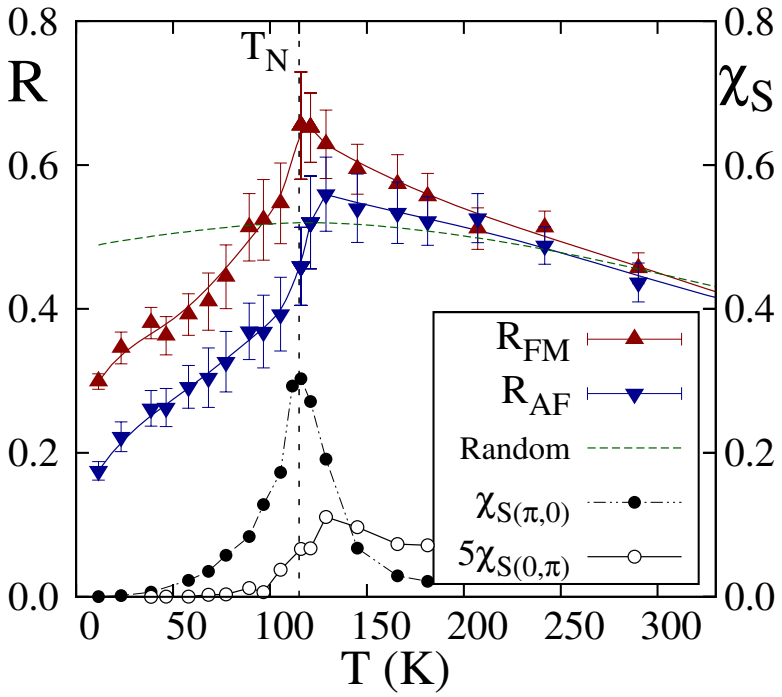

Figure 4.5: (color online) Resistance R of the SF model calculated via MC simulations, at $J_{\rm H}$=0.1 eV and using the L=256 TBC 8×8 cluster. $T_{\rm N}$ is indicated, and the magnetic susceptibilities χ_S are also shown. The FM-AFM directions asymmetry is evident at low T (note that the FM and AFM labels simply refer to the y and x directions, respectively, and not to fully FM or AFM spin configurations). As T increases the symmetry is restored, and the curves display a peak at $T_{\rm N}$. A small symmetry-breaking difference $r_{\rm NN}$=1.14 is used (see text). In green (dashed line) are the results for random spin configurations, showing that their R is smaller than in the MC results near $T_{\rm N}$. The width of the χ peaks extend to $\sim$1.5$T_{\rm N}$, in agreement with neutron scattering for $CaFe_2As_2$ Diallo et al. (2010).

At low-T in the ordered state the expected asymmetry between the $(\pi, 0)$ and $(0, \pi)$ electron pockets is observed (not shown), and more importantly satellite pockets (with electron character) develop close to the Γ hole pockets (Fig. 4.4(a)), as in ARPES experiments Luo et al. (2010); Yi et al. (2009). Thus, the SF model studied here passes the low-T ARPES test. As T increases, at or well above $T_{\rm N}$ (Figs. 4.4(b) and (c)) the xz and yz differences are reduced and rotational invariance is recovered, albeit with a FS broader than in the non-interacting low-T limit (Fig. 4.4(d)).

4.4 R vs. T curves.

Our most important result is the T dependence of R along the two axes, shown in Fig. 4.5. It is visually clear that these results are similar to the transport data of Ref. Chu et al. (2010); I.R. Fisher and Shen (2011), particularly after realizing that lattice effects, that cause the continuous raise of R with T in the experiments, are not incorporated in the SF model. A clear difference exists between the FM and AFM directions at low T, induced by the $(\pi, 0)$ magnetic order that breaks spontaneously rotational invariance. At low T, this difference was understood in the Hubbard-model HF approximation Zhang and Dagotto (2011) based on the reduction of the yz orbital population (Fig. 4.3(d)). This explanation is equally valid in the SF model, and at low T the SF model and the Hubbard model, when treated via the HF approximation, lead to similar physics.

The most interesting result in Fig. 4.5 is the development of a peak at $T_{\rm N}$, and the subsequent slow convergence of R toward similar values along both directions with further increasing T (as already discussed, to model better the effect of uniaxial stress Chu et al. (2010); I.R. Fisher and Shen (2011), a weak symmetry-breaking difference between the NN Heisenberg couplings along x and y was included). To our knowledge, this is the first time that the full R vs. T curve is successfully reproduced via computational studies.

A study as in Fig. 4.5 using a larger cluster, e.g. 16×16, is not practical since the computer time grows like N^4 (N=number of sites), leading to an effort 256 times larger. However, results as in Fig. 4.3(a) indicate that the classical spins configurations generated merely by the spin-spin interaction could be qualitatively similar to those generated by the full SF model, as long as $J_{\rm H}$ does not push the system into a new phase. Thus, the MC evolution could be carried out with $H_{\rm Heis}$ only, while measurements can still be performed using the full diagonalization of $H_{\rm SF}$. Such measurements (very CPU-time consuming) must be sufficiently sparsed in the MC evolution to render the process practical. This procedure was implemented

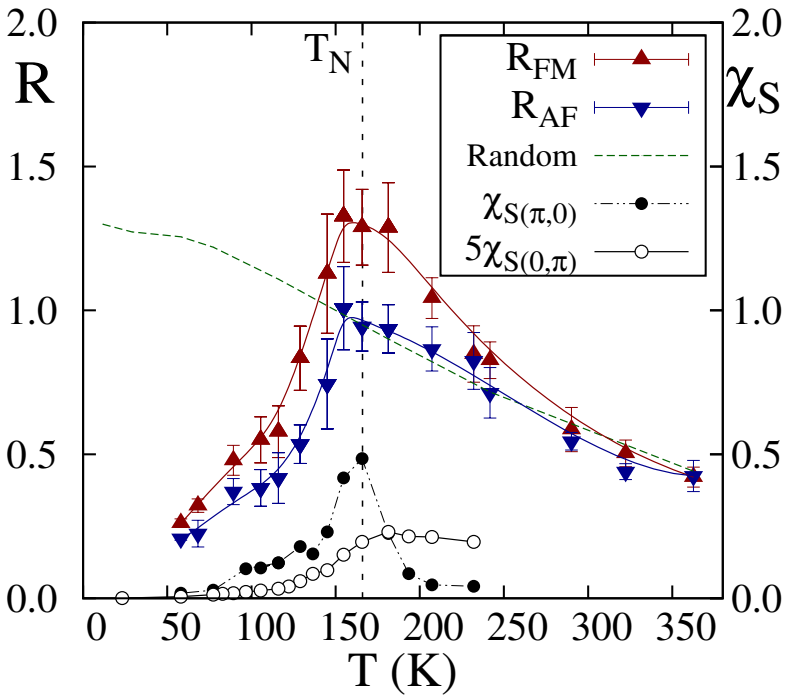

Figure 4.6: (color online) Resistance R calculated using a L=64 TBC 16×16 cluster, with $J_{\rm NN}$=0.032 (0.028) along the x (y) axis. The spin configurations are generated via $H_{\rm Heis}$, while the R measurements use the full $H_{\rm SF}$, at $J_{\rm H}$=0.1 eV. The rest of the notation is as in Fig. 4.5.

on a TBC 16×16 cluster, with L=64. Here, ∼200,000 (∼100,000) MC steps for thermalization (measurements) were employed. The R calculations are very CPU time consuming, thus only ∼20 were performed, but self-averaging effects render the error bars small. The results for R are in Fig. 4.6, and they show a remarkable similarity with Fig. 4.5, and with experiments. Thus, the essence of the R vs. T curves is captured by electrons moving in the spin configurations generated by $H_{\rm Heis}$. Size effects are small in the range analyzed here.

What causes the increase of R upon cooling before $T_{\rm N}$ is reached, displaying insulating characteristics? Since our results are similar to experiments, an analysis of the MC-equilibrated configurations may provide qualitative insight into their origin. In Fig. 4.7(a), a typical MC configuration of classical spins is shown. The colors at the links illustrate the relative orientation of the two spins at the ends. The $(\pi, 0)$ long-range order is lost, but individual spins are not randomly oriented. In fact, the state contains small regions resembling locally either a $(\pi, 0)$ or $(0, \pi)$ order (short-range spin order), and $S(\mathbf{q})$ still displays broad peaks at those two wavevectors. In standard mean-field approximations there are no precursors of the magnetic order above $T_{\rm N}$, but in the SF model there are short-range fluctuations in the same regime.

States with "spin patches" as in Fig. 4.7(a) lead to a concomitant patchy orbital order at the FS shown in Fig. 4.7(b), where the most populated orbital at μ at every site, either xz or yz, are indicated. The orbital orientation suggests that the xz (yz) FS population favors transport along the x (y) axis. The patchy order should have a resistance *larger* than that of a randomly-oriented spin background. This is confirmed by calculating R vs. T in the absence of a guiding Hamiltonian, i.e. by generating random spin configurations. The results are in Figs. 4.5 and 4.6 (green dashes) and their values are indeed *below* those of the peak resistance at $T_{\rm N}$ of the full SF model, i.e. with configurations as in Fig. 4.7. Then, the effect of strain coupled to short-range spin and FS orbital order appears to be the cause of the peak in the R vs. T curves Fernandes et al. (2011). Using a smaller (but nonzero) anisotropy, the R-T curves display a concomitantly smaller anisotropy, but still they have a small peak at

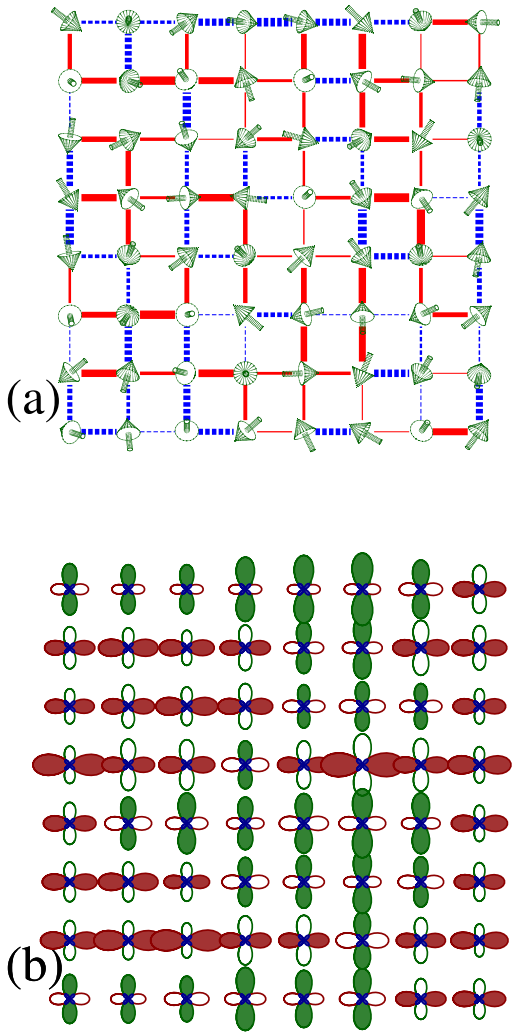

Figure 4.7: (color online) (a) Typical MC-generated classical spin configuration on an 8×8 cluster at T_N∼110 K, J_H=0.1 eV, and J_{NN}=0.016 (0.014) along the x (y) axis. The red (blue) lines denote AFM (FM) NN correlations, of intensity proportional to the width. (b) The dominant orbital at the FS at each site for the configuration used in (a), calculated using $n(\mu)$ as in Fig. 1(d). Red (green) denote the xz (yz) orbital, with a size proportional to the density.

T_N (not shown). Thus, the patchy states may also explain the insulating properties of $Fe_{1.05}Te$ Chen et al. (2009) and (Tl,K)$Fe_{2-x}Se_2$ Fang et al. (2011) above T_N.

4.5 Conclusions.

The Spin-Fermion model for pnictides was here studied with MC techniques. The magnetic and ARPES properties of the undoped compounds are well reproduced. Including a small explicit symmetry breaking to account for strain effects, the resistance R vs. T curves are qualitatively similar to those observed for $BaFe_2As_2$ Chu et al. (2010); I.R. Fisher and Shen (2011), including a peak at T_N that appears caused by short-range spin and FS orbital order. In our calculations, the anisotropy above T_N exists *only* as long as a strain distortion exists, compatible with results for annealed $BaFe_2As_2$ samples Nakajima et al. (2011). This successful application of a SF model paves the way to more demanding efforts involving doped systems where anisotropy effects are stronger than in the undoped limit Chu et al. (2010); I.R. Fisher and Shen (2011).

Chapter 5

Summary

In the begining of the thesis, we discussed the novel phases of multiferroic Manganites. These SOS phases, with their intrinsic 90 degree spin arrangement across the domain walls, create none-zero ferroelectricity through the inverse Dzyaloshinskii-Moriya mechanism. Furthermore, these two-dimensional SOS phases reduce their dimensionality into decoupled one-dimensional stripes. The different stripe arrangements have nearly-degenerate energies.

In the second part of the thesis, simple Monte Carlo calculations were used to analyze the recently unveiled $T-$phase of $BiFeO_3$ and its relatively low Néel temperature due to the weak inter-plane coupling MacDougall et al. (2012).

For iron pnictides, we studied the spin-fermion model, considering a relatively weaker J-Hund interaction than in transition metal oxides. In addition, twisted boundary conditions have been applied to study observables such as the one-particle spectral function $A(k, \omega)$, the resistance measurements, and the fine details of the structure of charge and orbital ordering specifically at the Fermi level. Our results agree with the ARPPES and resistivity anisotropy experiments. The peak at Néel temperature is also reproduced in our calculation which was shown to be caused by short-range orbital spin and charge ordering.

Bibliography

Bibliography

Blomberg, E. C., Kreyssig, A., Tanatar, M. A., Fernandes, R. M., Kim, M. G., Thaler, A., Schmalian, J., Bud'ko, S. L., Canfield, P. C., Goldman, A. I., and Prozorov, R. (2012). Effect of tensile stress on the in-plane resistivity anisotropy in $BaFe_2As_2$. *Phys. Rev. B*, 85:144509. 63, 68

Bondino, F., Magnano, E., Malvestuto, M., Parmigiani, F., McGuire, M. A., Sefat, A. S., Sales, B. C., Jin, R., Mandrus, D., Plummer, E. W., Singh, D. J., and Mannella, N. (2008). Evidence for strong itinerant spin fluctuations in the normal state of $CeFeAsO_{0.89}F_{0.11}$ iron-oxypnictide superconductors. *Phys. Rev. Lett.*, 101:267001. 61

Bramwell, S. T. and Gingras, M. J. P. (2001). Spin ice state in frustrated magnetic pyrochlore materials. *Science*, 294:1495–1501. 11

Buhler, C., Yunoki, S., and Moreo, A. (2000). Magnetic domains and stripes in a spin-fermion model for cuprates. *Phys. Rev. Lett.*, 84:2690–2693. 61

Chen, G. F., Chen, Z. G., Dong, J., Hu, W. Z., Li, G., Zhang, X. D., Zheng, P., Luo, J. L., and Wang, N. L. (2009). Electronic properties of single-crystalline $Fe_{1.05}Te$ and $Fe_{1.03}Se_{0.30}Te_{0.70}$. *Phys. Rev. B*, 79:140509. 75

Chen, K., Ferrenberg, A. M., and Landau, D. P. (1993). Static critical behavior of three-dimensional classical heisenberg models: A high-resolution monte carlo study. *Phys. Rev. B*, 48:3249–3256. 38

Cheong, S.-W. and Mostovoy, M. (2007). Multiferroics: a magnetic twist for ferroelectricity. *Nature Mater.*, 6:13–20. ix, x, 5, 6, 9

Chu, J.-H., Analytis, J. G., Greve, K. D., McMahon, P. L., Islam, Z., Yamamoto, Y., and Fisher, I. R. (2010). In-plane resistivity anisotropy in an underdoped iron pnictide superconductor. *Science*, 329(5993):824. 62, 68, 71, 75

Chuang, T., Allan, M., Lee, J., Xie, Y., Ni, N., Bud'ko, S. L., Boebinger, G. S., Canfield, P. C., and Davis, J. (2010). Nematic electronic structure in the "parent" state of the iron-based superconductor $Ca(Fe_{1-x}Co_x)_2As_2$. *Science*, 327(5962):181. 60

Daghofer, M., Luo, Q.-L., Yu, R., Yao, D. X., Moreo, A., and Dagotto, E. R. (2010a). Orbital-weight redistribution triggered by spin order in the pnictides. *Phys. Rev. B*, 81(18):180514(R). 66, 68

Daghofer, M., Nicholson, A., Moreo, A., and Dagotto, E. R. (2010b). *Phys. Rev. B*, 81(1):014511. viii, xix, xx, 63, 64, 65, 69

Dagotto, E. (2002). *Nanoscale Phase Separation and Colossal Magnetoresistance*. Berlin: Springer. 11, 12

Dagotto, E. (2005). Complexity in strongly correlated electronic systems. *Science*, 309:257–262. 9

Dagotto, E., Hotta, T., and Moreo, A. (2001). Colossal magnetoresistant materials: The key role of phase separation. *Physics Reports*, 344(13):1 – 153. 1, 11, 12, 62, 65, 66

de la Cruz, C., Huang, Q., Lynn, J. W., Li, J., II, W. R., Zarestky, J. L., Mook, H. A., Chen, G. F., Luo, J. L., Wang, N. L., and Dai, P. (2008). Magnetic order close to superconductivity in the iron-based layered $LaO_{1-x}F_xFeAs$ systems. *Nature*, 453:899–902. 60, 68

Deisenhofer, J., Eremin, M. V., Zakharov, D. V., Ivanshin, V. A., Eremina, R. M., Krug von Nidda, H.-A., Mukhin, A. A., Balbashov, A. M., and Loidl, A. (2002). Crystal field, Dzyaloshinsky-Moriya interaction, and orbital order in $La_{0.95}Sr_{0.05}MnO_3$ probed by ESR. *Phys. Rev. B*, 65:104440. 8

Dhital, C., Yamani, Z., Tian, W., Zeretsky, J., Sefat, A. S., Wang, Z., Birgeneau, R. J., and Wilson, S. D. (2012). Effect of uniaxial strain on the structural and magnetic phase transitions in $BaFe_2As_2$. *Phys. Rev. Lett.*, 108:087001. 63, 68

Diallo, S. O., Pratt, D. K., Fernandes, R. M., Tian, W., Zarestky, J. L., Lumsden, M., Perring, T. G., Broholm, C. L., Ni, N., Bud'ko, S. L., Canfield, P. C., Li, H.-F., Vaknin, D., Kreyssig, A., Goldman, A. I., and McQueeney, R. J. (2010). Paramagnetic spin correlations in $CaFe_2As_2$ single crystals. *Phys. Rev. B*, 81:214407. xxi, 70

Dong, S., Yu, R., Liu, J.-M., and Dagotto, E. (2009). Striped multiferroic phase in double-exchange model for quarter-doped manganites. *Phys. Rev. Lett.*, 103:107204. 10, 14, 19, 20, 22, 25

Dong, S., Yu, R., Yunoki, S., Alvarez, G., Liu, J.-M., and Dagotto, E. (2008a). Magnetism, conductivity, and orbital order in $(LaMnO_3)_{2n}/(SrMnO_3)_n$ superlattices. *Phys. Rev. B*, 78:201102(R). 7

Dong, S., Yu, R., Yunoki, S., Liu, J.-M., and Dagotto, E. (2008b). Origin of multiferroic spiral spin order in the $RMnO_3$ perovskites. *Phys. Rev. B*, 78:155121. x, 7, 16

Fang, M.-H., Wang, H.-D., Dong, C.-H., Li, Z.-J., Feng, C.-M., Chen, J., and Yuan, H. Q. (2011). Fe-based superconductivity with Tc=31 K bordering an antiferromagnetic insulator in (Tl,K) Fe_xSe_2. *EPL*, 94:27009. 75

Fernandes, R. M., Abrahams, E., and Schmalian, J. (2011). Anisotropic in-plane resistivity in the nematic phase of the iron pnictides. *Phys. Rev. Lett.*, 107:217002. 73

Fiebig, M. (2005). Revival of the magnetoelectric effect. *Journal of Physics D: Applied Physics*, 38:R123–R152. 9

Giovannetti, G., Kumar, S., van den Brink, J., and Picozzi, S. (2009). Magnetically induced electronic ferroelectricity in half-doped manganites. *Phys. Rev. Lett.*, 103:037601. xiii, 11, 27

Goto, T., Kimura, T., Lawes, G., Ramirez, A. P., and Tokura, Y. (2004). Ferroelectricity and giant magnetocapacitance in perovskite rare-earth manganites. *Phys. Rev. Lett.*, 92:257201. x, 4, 7

Gretarsson, H., Lupascu, A., Kim, J., Casa, D., Gog, T., Wu, W., Julian, S. R., Xu, Z. J., Wen, J. S., Gu, G. D., Yuan, R. H., Chen, Z. G., Wang, N.-L., Khim, S., Kim, K. H., Ishikado, M., Jarrige, I., Shamoto, S., Chu, J.-H., Fisher, I. R., and Kim, Y.-J. (2011). Revealing the dual nature of magnetism in iron pnictides and iron chalcogenides using x-ray emission spectroscopy. *Phys. Rev. B*, 84:100509. 61

Harrison, W. A. (1989). *Electronic Structure and the Properties of Solids*. New York: Dover. 44, 68

Holm, C. and Janke, W. (1993). Critical exponents of the classical three-dimensional heisenberg model: A single-cluster monte carlo study. *Phys. Rev. B*, 48:936–950. 38

Hotta, T. (2006). Orbital ordering phenomena in d- and f-electron systems. *Rep. Prog. Phys.*, 69:2061–2155. 20

Hotta, T., Moraghebi, M., Feiguin, A., Moreo, A., Yunoki, S., and Dagotto, E. (2003). Unveiling new magnetic phases of undoped and doped manganites. *Phys. Rev. Lett.*, 90:247203. 20

I.R. Fisher, L. D. and Shen, Z. (2011). In-plane electronic anisotropy of underdoped '122' fe-arsenide superconductors revealed by measurements of detwinned single crystals. *Rep. Prog. Phys.*, 74:124506. 62, 63, 68, 71, 75

Ishiwata, S., Kaneko, Y., Tokunaga, Y., Taguchi, Y., Arima, T., and Tokura, Y. (2010). Perovskite manganites hosting versatile multiferroic phases with symmetric and antisymmetric exchange strictions. *Phys. Rev. B*, 81:100411(R). 10

Johnston, D. (2010). *Advances in Physics*, 59(6):803–1061. 60, 63

Kaplan, T. A. and Mahanti, S. D. (1997). On the relation of the double-exchange model to low-temperature magnetic properties of doped manganites. *J. Phys.: Condens. Matter*, 9:L291–L297. x, 16

Katsura, H., Nagaosa, N., and Balatsky, A. V. (2005). Spin current and magnetoelectric effect in noncollinear magnets. *Phys. Rev. Lett.*, 95:057205. 10, 14

Khomskii, D. (2009). Classifying multiferroics: Mechanisms and effects. *Physics*, 2:20. 9

Kimura, T. (2007). Spiral magnets as magnetoelectrics. *Annu. Rev. Mater. Res.*, 37:387–413. 10

Kimura, T., Sekio, Y., Nakamura, H., Siegrist, T., and Ramirez, A. P. (2008). Cupric oxide as an induced-multiferroic with high-T_C. *Nature Mater.*, 7:291–294. 10

Kitagawa, Y., Hiraoka, Y., Honda, T., Ishikura, T., Nakamura, H., and Kimura, T. (2010). Low-field magnetoelectric effect at room temperature. *Nature Mater.*, 9:797–802. 10

Krüger, F., Kumar, S., Zaanen, J., and van den Brink, J. (2009). Spin-orbital frustrations and anomalous metallic state in iron-pnictide superconductors. *Phys. Rev. B*, 79(5):054504. 61, 63

Liang, S., Alvarez, G., Şen, C., Moreo, A., and Dagotto, E. (2011). Transport anisotropy of the pnictides studied via Monte Carlo simulations of a Spin-Fermion model. *ArXiv e-prints*. 60

Liang, S., Daghofer, M., Dong, S., Şen, C., and Dagotto, E. (2011). Emergent dimensional reduction of the spin sector in a model for narrow-band manganites. *Phys. Rev. B*, 84:024408. 11

Luo, Q., Martins, G., Yao, D.-X., Daghofer, M., Yu, R., Moreo, A., and Dagotto, E. (2010). Neutron and ARPES constraints on the couplings of the multiorbital Hubbard model for the iron pnictides. *Phys. Rev. B*, 82:104508. 61, 68, 70

MacDougall, G. J., Christen, H. M., Siemons, W., Biegalski, M. D., Zarestky, J. L., Liang, S., Dagotto, E., and Nagler, S. E. (2012). Antiferromagnetic transitions in tetragonal-like $BiFeO_3$. *Phys. Rev. B*, 85:100406. 34, 38, 44, 48, 76

Malashevich, A. and Vanderbilt, D. (2008). First-principles study of improper ferroelectricity in $TbMnO_3$. *Phys. Rev. Lett.*, 101:037210. 10

Mermin, N. D. and Wagner, H. (1966). Absence of ferromagnetism or antiferromagnetism in one- or two-dimensional isotropic heisenberg models. *Phys. Rev. Lett.*, 17:1307–1307. 38

Moraghebi, M., Buhler, C., Yunoki, S., and Moreo, A. (2001). Fermi surface and spectral functions of a hole-doped spin-fermion model for cuprates. *Phys. Rev. B*, 63:214513. 61

Moraghebi, M., Yunoki, S., and Moreo, A. (2002a). Optical conductivity and resistivity of a hole-doped spin-fermion model for cuprates. *Phys. Rev. B*, 66:214522. 61

Moraghebi, M., Yunoki, S., and Moreo, A. (2002b). Robust D -wave pairing correlations in a hole-doped spin-fermion model. *Phys. Rev. Lett.*, 88:187001. 62

Nakajima, M., Liang, T., Ishida, S., Tomioka, Y., Kihou, K., Lee, C., Iyo, A., Eisaki, H., Kakeshita, T., Ito, T., and Uchida, S. (2011). Unprecedented anisotropic metallic state in undoped iron arsenide $BaFe_2As_2$ revealed by optical spectroscopy. *Proceedings of the National Academy of Sciences*, 108:12238. 75

Picozzi, S., Yamauchi, K., Sanyal, B., Sergienko, I. A., and Dagotto, E. (2007). Electric polarization reversal and memory in a multiferroic material induced by magnetic fields. *Phys. Rev. Lett.*, 99:227201. 10, 14

Pratt, D. K., Kim, M. G., Kreyssig, A., Lee, Y. B., Tucker, G. S., Thaler, A., Tian, W., Zarestky, J. L., Bud'ko, S. L., Canfield, P. C., Harmon, B. N., Goldman, A. I., and McQueeney, R. J. (2011). Incommensurate spin-density wave order in electron-doped $BaFe_2As_2$ superconductors. *Phys. Rev. Lett.*, 106:257001. 60

Qazilbash, M., Hamlin, J., Baumbach, R., Zhang, L., Singh, D., Maple, M., and Basov, D. (2009). Electronic correlations in the iron pnictides. *Nature*, 5:647 – 650. 61

Riera, J., Hallberg, K., and Dagotto, E. (1997). Phase diagram of electronic models for transition metal oxides in one dimension. *Phys. Rev. Lett.*, 79:713–716. x, 16

Salafranca, J., Alvarez, G., and Dagotto, E. (2009). Electron-lattice coupling and partial nesting as the origin of Fermi-Arcs in manganites. *Phys. Rev. B*, 80:155133. 13, 66

Schiffer, P., Ramirez, A. P., Bao, W., and Cheong, S.-W. (1995). Low temperature magnetoresistance and the magnetic phase diagram of $La_{1-x}Ca_x$ MnO_3. *Phys. Rev. Lett.*, 75:3336–3339. ix, 1, 2

Sergienko, I. A., Şen, C., and Dagotto, E. (2006). Ferroelectricity in the magnetic E-phase of orthorhombic perovskites. *Phys. Rev. Lett.*, 97:227204. 10, 14

Sergienko, I. A. and Dagotto, E. (2006). Role of the Dzyaloshinskii-Moriya interaction in multiferroic perovskites. *Phys. Rev. B*, 73:094434. 4, 10, 14

Shimojima, T., Ishizaka, K., Ishida, Y., Katayama, N., Ohgushi, K., Kiss, T., Okawa, M., Togashi, T., Wang, X. Y., Chen, C. T., Watanabe, S., Kadota, R., Oguchi, T., Chainani, A., and Shin, S. (2010). Orbital-dependent modifications of electronic structure across the magnetostructural transition in BaFe2As2. *Phys. Rev. Lett.*, 104(5):057002. 60

Vergés, J. A. (1999). Computational implementation of the kubo formula for the static conductance: Application to two-dimensional quantum dots. *Comput. Phys. Commun.*, 118:71. 68

Wang, K. F., Liu, J.-M., and Ren, Z. F. (2009). Multiferroicity: the coupling between magnetic and polarization orders. *Advances in Physics*, 58:321–448. 10

Wollan, E. O. and Koehler, W. C. (1955). Neutron diffraction study of the magnetic properties of the series of perovskite-type compounds $La_{1-x}Ca_xMnO_3$. *Physical Review*, 100:545–563. 25

Xiang, H. J., Wei, S.-H., Whangbo, M.-H., and Silva, J. L. F. D. (2008). Spin-orbit coupling and ion displacements in multiferroic $TbMnO_3$. *Phys. Rev. Lett.*, 101:037209. 10

Yasuda, C., Todo, S., Hukushima, K., Alet, F., Keller, M., Troyer, M., and Takayama, H. (2005). Néel temperature of quasi-low-dimensional heisenberg antiferromagnets. *Phys. Rev. Lett.*, 94:217201. viii, 40, 42

Yi, M., Lu, D. H., Analytis, J. G., Chu, J.-H., Mo, S.-K., He, R.-H., Hashimoto, M., Moore, R. G., Mazin, I. I., Singh, D. J., Hussain, Z., Fisher, I. R., and Shen, Z.-X. (2009). Unconventional electronic reconstruction in undoped (Ba,Sr)Fe_2As_2 across the spin density wave transition. *Phys. Rev. B*, 80:174510. 70

Yin, W.-G., Lee, C.-C., and Ku, W. (2010). Unified picture for magnetic correlations in iron-based superconductors. *Phys. Rev. Lett.*, 105:107004. 61, 63

Yu, R., Trinh, K. T., Moreo, A., Daghofer, M., Riera, J. A., Haas, S., and Dagotto, E. R. (2009a). *Phys. Rev. B*, 79(10):104510. 61

Yu, R., Yunoki, S., Dong, S., and Dagotto, E. (2009b). Electronic and magnetic properties of $R\mathrm{MnO}_3/a\mathrm{MnO}_3$ heterostructures. *Phys. Rev. B*, 80:125115. 13

Z. P. Yin, K. H. and Kotliar, G. (2011). Kinetic frustration and the nature of the magnetic and paramagnetic states in iron pnictides and iron chalcogenides. *Nature Materials*, 10:932–935. 61

Zang, J., Roder, H., Bishop, A. R., and Trugman, S. A. (1997). Magnetic properties of the double-exchange model. *J. Phys.: Condens. Matter*, 9:L157–L163. x, 16

Zhang, X. and Dagotto, E. (2011). Anisotropy of the optical conductivity of a pnictide superconductor from the undoped three-orbital Hubbard model. *Phys. Rev. B*, 84:132505. 63, 71

Appendix

Appendix A

Multi d-orbitals for Manganites and Iron pnictides

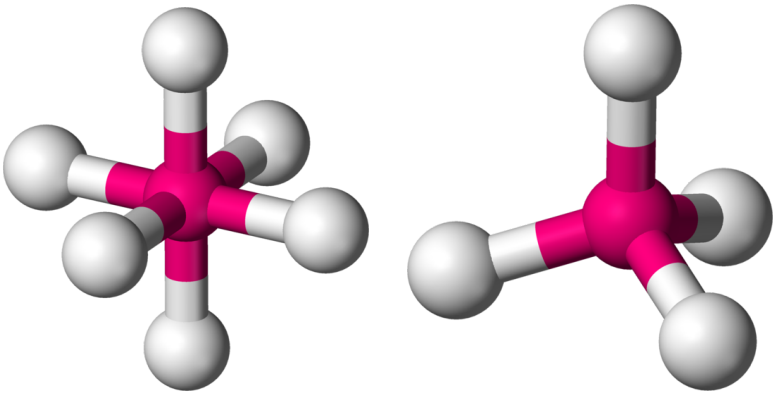

(a) Octahedral geometry **(b)** Tetrahedral geometry

Figure A.1: The d electron degeneracy is broken under a crystal field. (a) Octahedral structure with one Mn in the center and eight Oxygen atoms along the x, y and z axis. (b) Tetrahedral structure with one Fe atom in the center and four Arsenic atoms around it. These figures are reproduced from wikipedia.

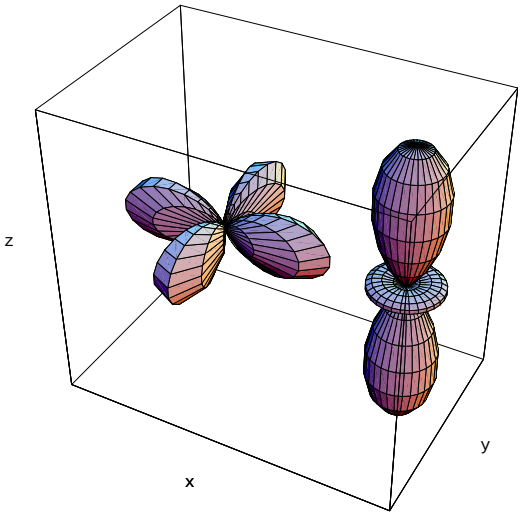

Figure A.2: e_g d orbitals: $x^2 - y^2$, $3r^2 - z^2$. This figure is courtesy of Alexander Pruell.

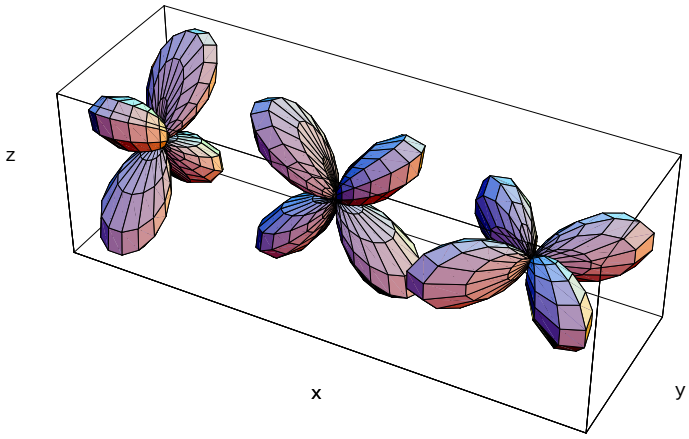

Figure A.3: t_{2g} d orbitals: yz, xz and xy. This figure is courtesy of Alexander Pruell.

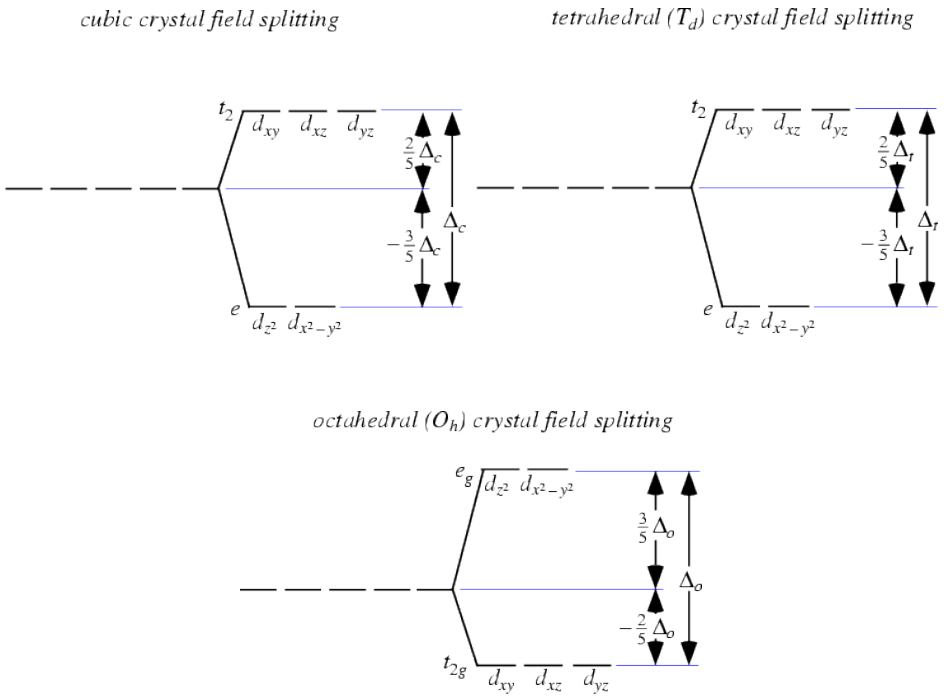

Figure A.4: The energy levels of the e_g and t_{2g} d electrons vary under different types of crystal fields. These figures are reproduced from http://scienceworld.wolfram.com.

Vita

Shuhua Liang was born on August 8, 1983. After he earned his Bachelor degree on theoretical physics from the University of Science and Technology of China at Hefei, he entered the Department of Physics of University of Tennessee at Knoxville as a graduate teaching assistant. In 2007, he joined the condensed matter theory group as a research assistant with Dr. Elbio Dagotto as his advisor. His main research area includes the multiferroic properties of manganites and the transport and magnetic properties of iron pnictides. In 2012 Shuhua will join the University of Tennessee as a post doctoral researcher with Dr. Elbio Dagotto.